Cooling of a tube by a two-phase flow under microgravity conditions

Tomás Pereira Nave Henriques da Silva

Thesis to obtain the Master of Science Degree in

Aerospace Engineering

Supervisors: Prof. Catherine Colin
Prof. António Luís Nobre Moreira

Examination Committee

Chairperson: Prof. Paulo Oliveira
Supervisor: Prof. António Luís Nobre Moreira
Member of the Committee: Prof. Ana Sofia Henriques Moita

November 2021

Dedicated to my grandparents.

Acknowledgments

Firstly, I would like to thank my internship tutor, Prof. Catherine Colin, for giving me the opportunity to do an internship in a subject that reunites what I like most, space and fluid mechanics. Moreover, I am very grateful for all the time, patience and support, guiding me throughout the internship without ever imposing anything. I can only hope to have more bosses with a similar mindset in my future career.

Secondly, I would like to thank Prof. António Moreira for having accepted to be my thesis' tutor from the part of Técnico Lisboa.

Finally, I would like to thank my family. My parents for always giving me the liberty to do my own choices, for trusting that I know what I am doing, and for all the love and support that they give me. My brother for being an unconventional role model, showing me that is possible to go through very hard times in life, get those behind our back and become successful. My grandmother for all the love and our weekly talks where I learn about life. My other grandparents that unfortunately are not here anymore, but whose principles guide me through life and make me a better person.

Resumo

Esta tese apresenta o estudo da modelisação de escoamentos difásicos durante o arrefecimento rápido de motores de foguetão criogénicos em microgravidade. É apresentada uma revisão bibliográfica completa de todas as experiências feitas nesta área até à data, que permite perceber a escassez de dados e de modelos que expliquem correctamente os fenómenos físicos que acontecem. Assim sendo, este trabalho apresenta resultados experimentais obtidos a partir do arrefecimento de um tubo de aço inoxidável usando HFE7100 como líquido refrigerante. É estudado o impacto do nível de gravidade, do débito de massa e do sub-arrefecimento do líquido no regime de ebulição em filme, na temperatura de Leidenfrost, no fluxo de calor crítico e no regime de ebulição nucleada. É ainda proposta uma correlação para o regime de ebulição em filme, validada usando os dados de experiências com HFE7100 e também com azoto líquido, aplicável tanto em gravidade normal como em microgravidade.

Keywords: arrefecimento rápido, ebulição em filme, temperatura de Leidenfrost, velocidade de re-humedecimento, fluxo de calor crítico, regime de ebulição nucleada, microgravidade

Abstract

This master's thesis presents a study of the modelling of liquid-vapour flows during the chill down of rocket engines by cryogenic fluid in microgravity. A thorough literature review on reduced gravity quenching experiments is presented, showing the scarcity of experimental data and accurate models. Experimental results obtained with the quenching of a stainless steel tube by HFE7100 are presented. The impact of gravity level and flow mass flux and subcooling on film boiling, rewetting temperature, critical heat flux and nucleate boiling is investigated. A correlation for the film boiling regime is presented, validated for HFE7100 and LN2, for terrestrial and microgravity conditions.

Keywords: quenching, film boiling, rewetting temperature, rewetting velocity, critical heat flux, nucleate boiling, microgravity

Contents

List of Tables

List of Figures

Nomenclature

Symbols

$\Delta h_{l,v}$	Latent heat of vaporisation.
$\dot{m}$	Mass flow rate
A	Surface of the test section.
Bi	Biot number.
Cp	Specific heat at constant pressure.
D	Internal diameter of the test tube.
e	Thickness of the tube’s wall.
Fr	Froude number.
G	Mass flux.
g	Gravity acceleration.
Ja	Jakob number.
L	Length of the test section.
M	Molecular weight
p	Pressure
Pe	Peclet number.
Pr	Prandtl number.
q	Heat flux.
Re	Reynolds number.
T	Temperature.
t	Time.
u	Average velocity.

We	Weber number.
x	Vapour quality.

Greek symbols

α	Void fraction.
δ	Thickness of the vapour film.
λ	Thermal conductivity coefficient.
μ	Dynamic viscosity.
ν	Cinematic viscosity.
ρ	Density.
σ	Surface tension.

Subscripts

c	Critical
chf	Critical heat flux.
exp	Experimental.
fb	Film boiling.
fc	Forced convection.
l	Liquid phase.
nb	Nucleate boiling.
r	Rewetting.
sat	Saturation.
v	Vapour phase.
w	Wall.

Chapter 1

Introduction

1.1 Motivation

Since the 1960s, cryogenic engines have been used for their high efficiency. This type of engines has been used in Ariane launchers for decades, especially in the upper stages, which means that they are responsible for correctly inserting the payload in orbit.

In particular, Ariane 5 ES (Evolution Storable) is equipped with an upgraded storable propellant stage, allowing re-ignition and long coast phases [1]. Moreover, the upper stage of the upcoming Ariane 6 is powered by the re-ignitable Vinci engine [2]. Furthermore, during the re-ignition phases of the cryogenic engines, it is necessary to chilldown the supply pipes and the turbopumps beforehand. To do so, the cryogenic propellants are injected into the tubes which are at a temperature close to 300K. Since the cryogenic liquids used as fuels in space applications must be free of vapour, being able to predict when a certain tube subjected to a particular set of flow conditions has been sufficiently cooled down, so that the propellant can flow through it without phase-changing, is a critical safety concern.

From a mission point of view, it is important to have an accurate estimation of the time that this chilldown process takes, along with the mass of propellant necessary. Since the liquid used to cool down the tubes is not re-used for combustion purposes, an accurate model of the chilldown process allows to reduce the quantity of propellant wasted.

Moreover, in the future of space activity it will be important to have the capability of refuelling spacecraft in-orbit. This idea has already been studied and some well-thought projects exist in paper, such as the OTV Network System [3]. However, for this to be possible, a good knowledge and understanding of the two-phase flow characteristics of cryogenic fluids is paramount, seeing that the transfer lines between storage tanks would also need to be cooled down.

In both cases, one fundamental aspect that makes the modelling of the chilldown process more complex is the fact that it happens in weightless conditions. In fact, there is very little data in literature regarding two-phase flow heat transfer in microgravity, which is why the work developed presented in this thesis is useful.

1.2 Topic Overview

The research about flow heat transfer under microgravity conditions started in the 1960's due to the rapid growth of the space industry and the need to understand how fluids behave in low gravity. Initially, the research was mainly focused in the pool boiling mechanisms, but since then a considerable amount of research has also been conducted on flow patterns and flow maps for adiabatic two-phase flow, that made possible the refinement of the boiling models. However, low gravity flow boiling, unlike pool boiling and adiabatic two-phase flow, has not received much attention in the past mainly due to the fact that it is, by far, the more complex of the three phenomena. In addition, thorough understanding of pool boiling is a necessary initial step in analysing flow boiling since it constitutes a fundamental element of the latter.

There are four platforms where microgravity experiments can be performed. The terrestrial-based options include sounding rockets, parabolic flights and drop towers. Then, there is also the possibility of performing the experiments in International Space Station (ISS).

First, drop towers are the least expensive option, are easy to use and offer the best microgravity levels among the three terrestrial-based options. Moreover, they can be operated on a daily basis and allow the experiment hardware to be changed at short notice and the experiment set-up to be adjusted or improved between drops [4]. However, its use is not suitable for all kinds of experiments since it only offers a few seconds of microgravity per trial (10 seconds maximum), which may not be enough to complete an experiment. On the other hand, parabolic flights are also relatively easy to use and have the advantage of offering longer microgravity periods (around 20 seconds) and allowing the intervention of researchers during the experience. Nevertheless, the cost is higher and the flights need to be booked a few months in advance.

In order to increase the microgravity period to a few minutes, sounding rockets can be used to perform the experiment. Despite this great advantage, the cost is even higher than for parabolic flights and it takes a few years to design and implement the experiment on the rocket. Moreover, once its launched, the researchers have little possibility to intervene. Finally, long weightlessness periods can be obtained by performing the experiments in the ISS. Not only the microgravity level is very low, but the astronauts can intervene in the experiments if necessary. Nevertheless, sending an experiment to the ISS is a very expensive and complex process, which may take years between the experiment design and its implementation. During the experiment, the data are downloaded by telemetry but the payload does not always return to Earth. All in all, the longer the microgravity period, the higher the cost and time required to perform the experiment.

Considering the small number of experiments ever performed to gather data about the flow boiling heat transfer during the chilldown process under microgravity conditions, it is possible to name and briefly describe each of them, in order to assess the results obtained and later compare to the results from this thesis.

To the best of my knowledge, the first experiment ever on this topic was conducted by Antar et. al [5] in 1990 using parabolic flights. Two experimental apparatuses were employed, one for studying subcooled liquid boiling and the other for examining saturated liquid boiling. For the saturated experiments, liquid nitrogen was used while Freon 113 was used for the subcooled experiments. The boiling phenomenon was investigated in both cases using flow visualisation techniques and by recording wall temperatures. It was found that the dispersed flow region, which is in between the fully vapour and the annular flow regions, appear to be influenced the greatest by the gravity field. In microgravity, the liquid droplets are very large and their shapes are nonuniform, varying from spherical to long meandering threads. On the other hand, in normal gravity the droplets are spherical in shape and small, flowing along the wall of the tube. It was concluded that this variation in the dispersed flow region may lead to diminishing heat flux in low gravity environment between the wall of the tube and the fluid.

Later in 1991, a master thesis on this topic was published by Sathasivam [6]. This experiment analysed the flow boiling in microgravity of saturated liquid nitrogen, and provided qualitative data thanks to the record of the flow boiling patter on film. Once again, the microgravity environment was simulated via parabolic flights.

In 1993, a PhD thesis published by Misawa [7] analysed flow boiling of saturated and subcooled Freon 113 under microgravity conditions, using both a drop tower and parabolic flights. Quantitative measurements were taken, and it was shown that the reduced gravity environment affected the subcooled two-phase heat transfer by increasing the void fraction and the stagnation of coalesced bubbles. Overall, it was concluded that the heat transfer coefficient was reduced under microgravity conditions.

In 1995, Adham-Khodaparast et al. [8] reported a series of experiments on flow quenching of a hot flat surface by Freon 113 using parabolic flights. During film boiling, heat transfer from the hot surface to the flowing liquid was found to be reduced under microgravity compared to normal gravity conditions due to the thickening of the vapour layer. In addition, the wall superheat and the surface heat flux at the onset of rewetting and the maximum heat flux during quenching of the hot surface were found to increase with the inlet liquid subcooling, mass flux and gravity level. Finally, it was concluded that the effect of microgravity was more important for low flow rates and decreased at high flow rates.

In the same year, Westbye et al. [9] also used Freon 113 to study the quenching of an initially hot, thin-walled stainless tube by injection of a subcooled liquid under microgravity conditions. The data collected were also compared with quenching tests performed under normal gravity conditions. It was found that the rewetting temperatures were around 20ºC lower and that the film boiling heat transfer coefficients decreased between 50 to 80 percent when compared to the results from the normal gravity experiments. This meant that the time to complete the tube quenching process was greatly extended in microgravity. It was also reported a slight increase in the rewetting velocity (the propagation velocity of the quench front) in microgravity. Furthermore, the boiling curves showed that both the nucleate and the transition boiling curves were shifted to lower wall superheats due to the lower rewetting temperature. Apart from that difference, the heat flux profiles of those boiling regimes were similar to the ones from the 1g results, indicating that these regimes are little affected by the reduction in gravity intensity.

In 1998, Xu [10] conducted experiments by injecting liquid R-113 and PF5060 into an initially dry, heated channel, which was 40 mm wide, 5 mm high and 200 mm long, on the ground and in reduced gravity conditions. It was reported that the boiling curves shifted to higher wall superheats with increasing liquid subcooling and gravity level. The boiling curves for R-113 were obtained in a higher wall superheat range compared to those for PF5060, because of higher rewetting temperature for R-113 than that for PF5060. In addition, the quench velocity and the rewetting temperature decreased for R-113 but only showed very slight decrease for PF5060 in reduced gravity. It was concluded that the quench velocity and rewetting temperature for R-113 were higher than those for PF5060 mainly due to a higher latent heat, higher surface tension and a smaller vapour density for R-113. Furthermore, the maximum heat flux increased with increasing flow rate, but decreased with reduction in inlet liquid subcooling and gravity level except for R-113 at high flow rates.

In 2007, Kawanami et al. [11] published their study on the heat transfer during tube quenching under microgravity conditions, using liquid nitrogen as the working fluid. The experiments were conducted at the Japan Microgravity Center (JAMIC) in the world's largest drop shaft at the time, capable of producing a weightless environment with a duration of about 10 seconds. Not only the tube was transparent to allow the visualisation of the fluid behaviour, but simultaneous measurements of the thermal characteristics and quench front velocity were also successfully carried out. Unlike previous experiments, it was reported an increase in the heat transfer coefficient in microgravity. On the other hand, it was reported a quench front velocity increase. This increase in heat transfer coefficient and quench front velocity is as high as 20 percent, and its magnitude decreases with increasing mass flow. It was concluded from these results that the increase in the heat transfer under microgravity conditions is a consequence of the increase in the quench front velocity.

One year later, Yuan et al. [12] published the results of their research aimed at the fundamental understanding of the cryogenic chilldown phenomena inside a pipe in terrestrial gravity and microgravity. The test section used was a Pyrex glass tube and the microgravity environment was simulated by using a 1.7-second drop tower. Flow patterns and wall temperature history during the chilldown were obtained for a range of different flow rates. Moreover, the wall temperature histories were measured at three downstream locations. It was found that the terrestrial chilldown process is divided into three stages based on the temperature of the tube wall. These stages are film boiling, nucleate boiling and single-phase convection, which carries a close similarity to the pool boiling mechanisms. It is reported that, in general, the cooling rate of the tube wall is proportional to the mass flow rate of the quenching flow. In microgravity, there is no stratified flow and the heat transfer from the wall is significantly reduced due to the fact that the absence of buoyancy force in a microgravity environment results in a flow with liquid filaments in the central core and with a low thermal conductivity vapour layer near the wall. Thus, it is concluded that the flow is axisymmetric and that the chilldown process is longer in microgravity.

In 2009, Celata et al. [13] studied the rewetting phenomenon by carrying out quenching tests at normal gravity and in parabolic flights with a vertical test section with liquid flowing upwards, using a test tube made of Pyrex with a diameter of 6.0 mm and using FC-72 as the working fluid. Measurements included wall temperature along the flow channel, inlet and outlet temperature, pressure and mass flow-rate. It was reported a significant decrease of the quenching velocity at reduced gravity, presenting values in the range of 5–7 mm/s, much lower than the values obtained at terrestrial gravity under the same conditions. It is also reported that the rewetting temperature is not affected by the gravity level and that it shows a slight reduction for the higher mass flow rate test cases. Finally, considering the fact that the tests were performed at a constant inlet liquid subcooling (25 °C), it is stated that the mass flow rate has a significant influence on the structure and on the behaviour of the liquid core during the inverted annular flow regime. In fact, for low mass flow rates, the liquid core is found to be irregular and continuously formed and disrupted during the cooling process, while for higher mass flow rates the liquid core is more stable and regular.

In 2016, Darr et al. [14] studied the effect of reduced gravity on cryogenic nitrogen boiling and pipe chilldown. To do so, heat transfer data were obtained from flowing LN2 through a stainless steel tube, both under normal gravity and microgravity conditions using parabolic flights to simulate the reduced gravity. It was reported that film boiling heat transfer was lessened by up to 25% in reduced gravity, resulting in longer time and more liquid to quench the pipe to liquid temperatures. Furthermore, the heat transfer was enhanced by increasing the flow rate, and the differences between reduced and terrestrial gravity diminished at high flow rates.

In 2019, Kinefuchi et al. [15] conducted an experiment under low gravity during the ballistic phase of an S-310-43 sounding rocket. In order to understand the physics of cryogenic chilldown in rocket engine turbopumps with low flow rate and low gravity, the test sections simulated the bearing room of a liquid oxygen turbopump, each of which has a complex flowpath including slits and a dead end. The working fluid was LN2 and the experiment was performed using two mass flow rates, 1.0 and 0.5 g/s. Then, the flight experiment data were compared to the ground data, revealing that the slits played an important role in the chilldown process and that the test sections were chilled down faster under low gravity. It was reported that the slits of the test sections formed liquid jets, and their behaviours were different from those in the ground experiment. Under microgravity conditions, the jets easily reached the dead end of the test sections and cooled down the whole walls due to the increase in inertia and wettability. Contrary to what was found in the precedent studies, heat transfer deterioration due to the bubble stagnation, bubble coalescence, or thick vapour film on the walls was never observed. In the ground experiment, the jets from the slits spread into droplets, which hardly arrived at the dead end. It is concluded that the dead end, which needs to be chilled down in the actual turbopump, it is easier to cool down in microgravity than in normal gravity conditions.

1.3 Objectives and Deliverables

The objective of the internship was to carry out a thorough research of recent studies on the transient boiling regimes observed during chilldown, especially under microgravity conditions. In particular, special focus was given to the theoretical modelling of the film boiling regime, since it is the regime that impacts the most the duration of the chilling process. Hence, a theoretical model coupled with the heat transfers in the tube wall was developed and validated using the data obtained in the scope of the PhD thesis of Brian Verthier [16], who designed and built at IMFT an experiment to study the chilldown process under microgravity conditions using a refrigerant fluid. Furthermore, an analysis was conducted in parallel to discuss the extrapolation of the proposed model to cryogenic fluids, using data found in the literature review.

1.4 Thesis Outline

The outline of the master's thesis is as follows: first a brief introduction on the importance of an accurate modelling of the chilldown process is made, followed by a presentation of all the studies done so far on the topic of chilldown under microgravity conditions. The main conclusions of those studies are presented in order to compare them with our own conclusions later. Next, the background section introduces the fundamental physics of the boiling curve, and offers an overview of the existing models and correlations for each boiling regime. Then, the experimental apparatus built during Verthier's PhD and its main components are described. The data processing required to obtain useful data from the experiment's sensors is also detailed. Afterwards, the results obtained are presented. Firstly, a parametric presentation of the results is made, followed by the results in modelling accurately the boiling curve. Finally, the conclusions of the work are presented along with some ideas for future work to be done in this area of research.

Chapter 2

Background

2.1 Theoretical Overview

2.1.1 Boiling Curve

Figure 2.1 illustrates the typical boiling curve for saturated water, initially plotted by Nukiyama [17], showing the heat flux as a function of the wall superheat, which is the difference in temperature between wall and fluid. This curve can be traversed from left to right (heating) or vice-versa (quenching), depending on the relative temperature difference between fluid and wall and the imposed method of wall heat flux. Moreover, it is possible to observe three different boiling regimes, namely: film boiling (FB), transition boiling (TB), and nucleate boiling (NB). These regimes are separated by three critical points, the Leidenfrost Point, LFP (point C), the Critical Heat Flux, CHF (point B), and the onset of nucleate boiling, ONB (point A).

In the quenching or chilldown configuration, the curve is traversed from right to left. Chilldown begins in the vapour film boiling regime due to the rapid evaporation of the liquid in the immediate vicinity of the wall at high temperature. Depending on the local conditions (inlet pressure, quality, mass flux, and degree of subcooling), the flow will proceed into dispersed flow film boiling (higher quality, low subcooling, and low mass flux) or inverted annular film boiling (IAFB) (low quality, high subcooling, and high mass flux). The latter is the one observed in our case. Film boiling is the least efficient regime regarding the transfer of energy from the wall, for the fact that a film of vapour fully covers its surface, forming an insulating layer due to the low thermal conductivity of vapour, therefore decreasing the heat transfer coefficient.

As the transfer line cools down, the system approaches the LFP, or rewetting temperature, where the heat flux reaches its minimum due to the existence of the insulating vapour layer combined with low wall superheat. The flow then proceeds and passes quickly through TB, characterised by intermittent contact between the liquid and the wall. This regime ends when the liquid is in full contact with the wall, at the point of CHF, where the heat transfer coefficient reaches its maximum value due to the highly efficient cooling process of boiling liquid through use of sensible and latent energy, and since the insulating vapour layer is not present anymore.

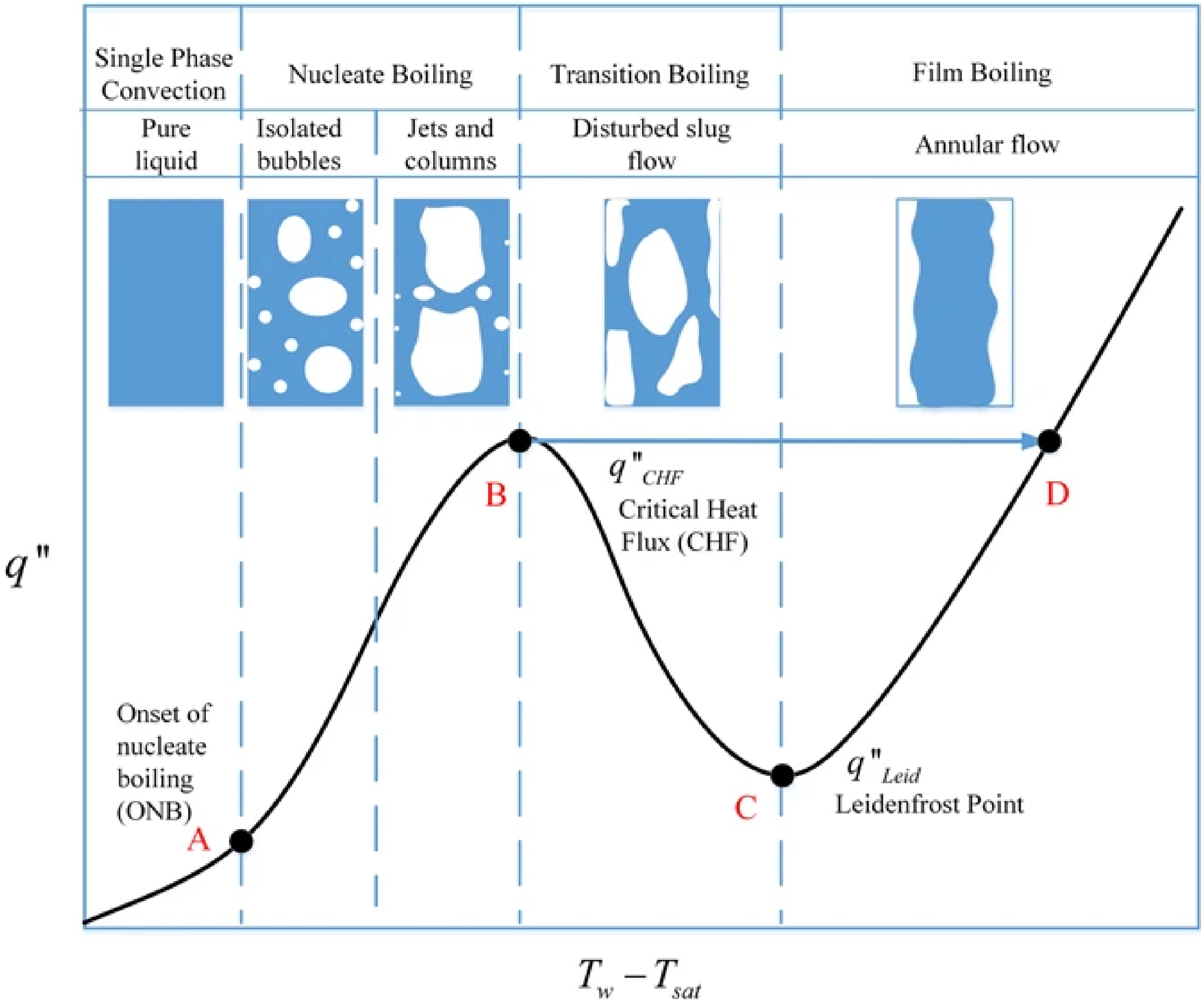

Figure 2.1: Boiling curve for saturated water.

Following is nucleate boiling regime, where heat is generated by vapour bubbles formed in surface cavities that are swept away from the wall surface. As the wall cools further, the system approaches the ONB, defined as the point at which the system progresses from nucleate two-phase cooling to single-phase liquid convection. Vapour-free liquid marks the end of the chilldown test.

This boiling curve is similar for the heating and quenching configurations. However, the value of the CHF can largely differ and a strong hysteresis may be observed in the nucleate boiling regime.

2.2 Models & correlations from the literature

2.2.1 Film boiling

Nusselt's model

One of the more classic approaches to describe the heat transfer in film boiling is an adaptation of the Nusselt model [18]. This model was built to predict wall heat transfer during the condensation of a liquid film falling along a vertical wall, but it has been transposed to the film boiling case by inverting the properties of liquid and vapour, as it can be seen in the work of Carey [19].

The model considers the development of a vapour film along an infinite vertical wall without the presence of flow other than the rise of the vapour by the hydrostatic pressure gradient generated by gravity. It is assumed that the heat exchange takes place only by conduction through the thin vapour film which allows to define the purely conductive exchange coefficient $h(z) = \lambda_v/\delta(z)$. The aim of this model is therefore to estimate the thickness $\delta(z)$ of the vapour film in order to obtain this exchange coefficient.

The starting point is to consider the balance of momentum in the vapour phase whose physical properties are considered constant (Equation 2.1). The pressure gradient $\frac{\partial p}{\partial z}$ is hydrostatic in the liquid phase, and the model assumes the pressure to be equal in both phases. In the case of a vertical test section and an ascending flow $g = 9.81m/s^2$.

$$\rho_v \left(\frac{\partial u_v}{\partial t} + u_v \nabla u_v \right) = -\frac{\partial p}{\partial z} + \mu_v \nabla^2 u_v - \rho_v g \tag{2.1}$$

Neglecting the inertia terms, represented by the left side of equation 2.1 and assuming zero shear at the interface, the velocity profile is parabolic. Hence, we obtain equation 2.2 where z is the distance from the start of film boiling.

$$u_v(z) = \frac{\rho_l - \rho_v)g}{\mu_v} \left(z\delta - \frac{z^2}{2} \right) \tag{2.2}$$

By integrating this profile over the thickness of the film, we can obtain the mass flow rate of vapour, m_v. Through an energy balance, it is possible to relate the variation of the mass flow rate to the heat flux through the wall, q_w. If we assume that the flow is purely conductive through the thickness δ, the variation in vapour mass flow as a function of the thickness of the film can be obtained according to the equation 2.3.

$$q_w = \frac{\lambda_v (T_w - T_{sat})}{\delta} = \Delta h'_{l,v} \frac{\partial \dot{m}}{\partial z} \tag{2.3}$$

Since the mass flow rate is related to the speed profile and therefore to the thickness of the film, the exchange coefficient can be expressed analytically at a distance z from the rewetting point according to the equation 2.4.

$$h(z) = \left[\frac{\lambda_v^3 \rho_v (\rho_l - \rho_v) g \Delta h'_{l,v}}{z \mu_v (T_w - T_{sat})} \right] \tag{2.4}$$

This model also allows for the consideration of the vapour superheating, by averaging the temperature of the vapour layer between the wall the saturated interface between the liquid and vapour phases. Thus, the effective latent heat $h'_{l,v}$ is a modified form taking this energy into account. In the same way we can take into account a subcooling of the liquid by adding the energy necessary to heat the vaporised liquid to saturation.

$$\Delta h'_{l,v} = \Delta h_{l,v} + 0.4 Cp_v (T_w - T_{sat}) + Cp_l (T_{sat} - T_l) \tag{2.5}$$

To this local conductive exchange coefficient, it would be advisable to add the energy emitted to the fluid by the wall through radiation. However, in the present study the superheats are relatively low, making this impact negligible.

Integral forms of the Nusselt's model

In order to be able to predict the film boiling averaged over a surface, many studies have been based on the model presented above, by integrating it on the geometry considered.

One of the first studies was made by Bromley [20], who integrated this local form for the case of horizontal cylinders in a fluid at rest. The integration around the cylinder involved its diameter D, as well as a constant of 0.62. He validated the expression obtained on experiments carried out with water, benzene, pentane, liquid nitrogen, and ethylene.

$$h = 0.62 \left[\frac{\lambda_v^3 \rho_v (\rho_l - \rho_v) g \Delta h'_{l,v}}{D \mu_v (T_w - T_{sat})} \right]^{1/4} \tag{2.6}$$

Klimenko [21] proposed another modification of equation 2.6 to take into account the Rayleigh-Taylor instability. He establishes several forms of the same law by adjusting the powers and empirical constants involved in the law according to the laminar or turbulent nature of the flow and overheating of the wall. In our case, i.e. for a turbulent vapour film and relatively low wall superheating, the correlation can be written:

$$h = 0.71 C \frac{\lambda_v}{D} \left[\frac{L_c^3 \rho_v^2 g}{\mu_v^2} \frac{\rho_l - \rho_v}{\rho_v} \right]^{1/2} \left[\frac{\mu_v C p_v}{\lambda_v} \right]^{1/3} \left[\frac{C p_v (T_w - T_{sat})}{\Delta h_{l,v}} \right]^{-1/3} \tag{2.7}$$

where $L_c = 2\pi \sqrt{\frac{\sigma}{g(\rho_l - \rho_v)}}$, and C is a constant which varies according to the fluid used in the experiment. Klimenko [21] suggested a value of 0.0086 for water, and Ramilison and Lienhard [22] proposed values of 0.0057 for R-113, 0.0066 for acetone and 0.0154 for benzene. Considering that the correct value for HFE7100 is unknown, the value for R-113 is used because among the various liquids, it is thought to be the one with more similarities with our working fluid.

Bromley's model

The models presented above were built for non-convective cases. This is taken into account from the start in Nusselt's model, assuming zero shear at the interface ($\tau_i = 0$).

Bromley et al. [23] proposed a modification for cylinders quenched at a velocity V_l normal to the axis in order to take this convection into account. He resumed the approach taken by Nusselt by adding an interfacial shear due to the convection of the liquid. The law obtained then combines the impact of the density difference on the hydrostatic pressure gradient and forced convection as can be seen in equation 2.8.

$$h = 0.88 \left(\frac{\lambda_v^3 \rho_v (\rho_l - \rho_v) g \Delta h'_{l,v}}{4 D \mu_v (T_w - T_{sat})} + \frac{3 h^2 V_l \lambda_v \rho_v \delta h'_{l,v}}{D (T_w - T_{sat})} \frac{\pi^2}{\theta^2} \right) \tag{2.8}$$

In his model, Bromley postulated that the heat transfer between the wall and the flow happened primarily by conduction through the vapour film. He considered that the transfers were made only on the upstream part of the cylinder, before the separation of the vapour layer, which is located at an angle θ.

Considering that the experiment being studied in this work is more similar to a flow tangent to a plane plate than a flow normal to a cylinder, Brian Verthier [16] proposed a modified version of the equation 2.8 by adjusting the constant translating the forced convection:

$$h = 0.88 \left(\frac{\lambda_v^3 \rho_v (\rho_l - \rho_v) g \Delta h'_{l,v}}{4D\mu_v (T_w - T_{sat})} + \frac{5h^2 V_l \lambda_v \rho_v \delta h'_{l,v}}{3D(T_w - T_{sat})} \right) \tag{2.9}$$

This correction was validated with the experimental data that is being used in this work, and it correlates well with the data. In spite of being a correction for the case of a flow tangent to a plane plate, the diameter of the cylinder stills play a role in the formula.

To solve this incoherence, it was decided that the best solution was to apply the Bromley's model to our specific case instead of changing the constant in the previously existing correlations. After searching in the literature for the application of the Bromley's model to a plane plate and not finding it, the demonstration can be found in Appendix A. The formula found was the following:

$$h = \left(\frac{4}{3}\right)^{3/4} \left(\frac{1}{2}\right)^{1/4} \left[\frac{\lambda_v^3 \rho_v (\rho_l - \rho_v) g h_{lv}^*}{6 L_{ref} \Delta T \mu_v} + \frac{h^2 u_L \lambda_v \rho_v h_{lv}^*}{L_{ref} \Delta T} \right]^{1/4} \tag{2.10}$$

Using the quadratic formula, the equation can be developed further so that the heat transfer coefficient can be found explicitly:

$$h_{co} = \frac{4}{3\sqrt{3}} \sqrt{\frac{u_L \lambda_v \rho_v h_{lv}^*}{L_{ref} \Delta T}} \cdot \left[1 + \sqrt{1 + \frac{9}{16} \frac{\lambda_v (\rho_l - \rho_v) g L_{ref} \Delta T}{u_L^2 \rho_v \mu_v h_{lv}^*}} \right]^{1/2} \tag{2.11}$$

The best value for L_{ref} was found to be around 0.012 m for experiments in microgravity conditions and 0.036 m for terrestrial conditions, based on the experimental results from our experiment. It was also validated for the results of the experiment using liquid nitrogen under microgravity conditions conducted by Darr et al. [24]. Considering that this is not a local method, i.e., the heat flux obtained is an average of the heat flux along the distance L_{ref}, in physical terms this length is thought to be the distance between the rewetting point and another point in the wall that can be used to obtain a representative value of heat flux along the wall.

Correlation for cryogenic fluids by Darr et al. [25]

Following their recent experiments in normal gravity and microgravity conditions using liquid nitrogen, Darr et al. [25] presented the following correlation for the film boiling regime, which is composed of three factors: buoyancy effects at low flow, forced convection at medium to high flows, and droplet heat transfer at high flows:

$$h = c_1 \left[\frac{\rho_v(\rho_l - \rho_v) g h_{l,v} \lambda_v^3}{4L\mu_v(T_w - T_{sat})} \right] + c_2 \left[1 + \left(\frac{D}{L + 0.1D} \right)^{0.7} \right] \left(\frac{\lambda_v}{D} \right) (1 - x_e)^{c_3} Re_g^{c_4} Pr_g^{0.4} + c_5 \left(\frac{\lambda_l}{D} \right) \exp\left[- \left(\frac{L}{D} \right)^{c_6} \right] We_l^{c_7} Ja_l^{-1} \tag{2.12}$$

where the coefficient c1 in the first term accounts for different flow directions; the second term was constructed from the Dittus–Boelter equation, multiplied by the two-phase multiplier that accounts for the speed of the vapour layer; and the third term correlates with data at high flow rates by using Weber (We) and Jakob (Ja) numbers. The values of the coefficients for the different scenarios, i.e., upwards flow, horizontal flow, downwards flow and microgravity can be found in the article cited.

2.2.2 Rewetting temperature

This section summarises the most commonly used models and correlations to calculate the rewetting temperature, i.e, the minimum film boiling temperature or Leidenfrost temperature. The existing models can be divided into several groups according to the mechanisms that trigger the rewetting process, as it was done by Bernardin and Mudawar [26] and Carey [19].

In classical thermodynamics, phase transitions for simple compressible substances are treated as quasi-equilibrium events at conditions corresponding to the saturation state. Between the saturated liquid and saturated vapour states exists a two-phase region where liquid and vapour coexist. Within this region, the temperature and pressure of the two phases must be constant, and the Gibbs function, chemical potential, and fugacity of each phase must be equal. In real-phase transformations, deviations from classical thermodynamics occur under non-equilibrium conditions, such as the superheating of a liquid above its boiling point. These non-equilibrium or metastable states are of practical interest and are important in determining limits or boundaries of real systems.

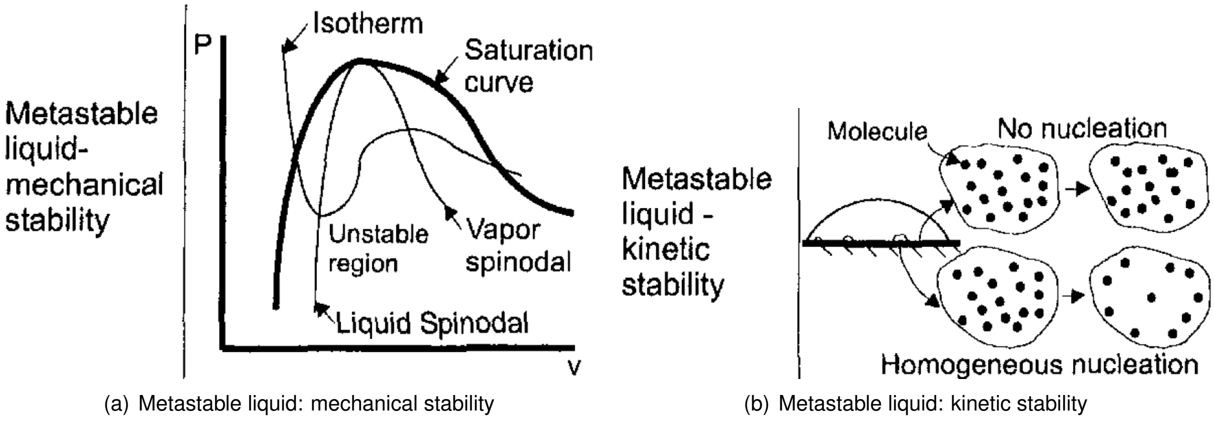

(a) Metastable liquid: mechanical stability

(b) Metastable liquid: kinetic stability

Figure 2.2: Metastability models. (source: Bernardin and Mudawar [26])

On the pressure-volume diagram in 2.2, it is possible to observe the superheated liquid and supercooled vapour regions separated by an unstable region. The lines separating these regions are referred to as the liquid and vapour spinodals, which represent the maximum superheating and supercooling limits. Two different approaches have been used in the literature to predict the superheat limit.

Hydrodynamic instability of the liquid-vapour interface

The first mechanism is based on the hypothesis that Taylor wave motion ease the release of vapour bubbles from the vapour film near the wall, and that the Leidenfrost temperature corresponds to the point with lowest heat flux that can maintain the vapour release mechanism without the formation of waves that can lead to the contact between the liquid and the wall.

In 1950, Taylor [27] used the assumptions of potential flow and sinusoidal disturbance between two fluids of different densities where the denser one is on top, along with a first-order perturbation analysis to demonstrate that gravity induced interfacial disturbances with wavelengths given by 2.13 are most likely to be amplified and, consequently, disrupt the smooth horizontal interface.

$$\lambda_d = 2\pi \left[\frac{3\sigma_f}{g(\rho_f - \rho_g)} \right]^{1/2} \tag{2.13}$$

Several authors have used Taylor's hydrodynamic stability theory to describe the rewetting temperature for pool boiling. In particular, Berenson [28] showed that the bubble spacing in film boiling was hydrodynamically controlled by a Rayleigh-Taylor instability and that the presence of the corresponding vapour layer and bubble departure supported film boiling by keeping the liquid from contacting the heated surface. Berenson's analytical expression, 2.14, to predict the minimum film pool boiling temperature, T_{wet}, coincides with the point at which vapour is not generated rapidly enough to sustain the Taylor waves at the liquid-vapour interface.

$$T_{wet,B} - T_{sat} = +0.127 \frac{\rho_v h_{fg}}{\lambda_v} \left[\frac{g(\rho_l - \rho_v)}{\rho_l + \rho_v} \right]^{2/3} \cdot \left[\frac{\sigma}{g(\rho_l - \rho_v)} \right]^{1/2} \cdot \left[\frac{\mu_v}{g(\rho_l - \rho_v)} \right]^{1/3} \tag{2.14}$$

However, as the heat flux decreases in the film boiling regime, some partial contact between the liquid and the wall may initially result in a slight departure from the film boiling conditions. This means that the initial collapse of the Taylor wave action might not correspond exactly to the point where the heat flux is minimal. To address this issue, Henry [29] developed a correction for Berenson's model that takes into account the effects of transient rewetting and subsequent liquid microlayer evaporation on the Leidenfrost temperature, presented in 2.15.

$$\frac{T_{wet,H} - T_{wet,B}}{T_{wet,B} - T_l} = 0.42 \left[\sqrt{\frac{k\rho c_p|_l}{k\rho c_p|_w}} \left(\frac{h_{lv}}{c_{p,w}(T_{wet,B} - T_{sat})} \right) \right]^{0.6} \tag{2.15}$$

This correlation was found to provide good agreement with available experimental data over a wide range of conditions. Having said, it failed to predict accurately the rewetting temperatures of the experiments in microgravity presented in this work. In order to improve the results, Brian Verthier [16] proposed a correction to Henry's formula to better fit the data for cases where the Reynolds number is inferior to 37000:

$$\frac{T_{w,Verthier} - T_{sat}}{T_{w,H} - T_{sat}} = 2.34 Re_l^{-0.068} \tag{2.16}$$

Metastable Liquid — Homogeneous and Heterogeneous Nucleation

On the other hand, Yao and Henry [30] and Sakurai et al. [31] reasoned that the minimum wall superheat in the film boiling regime is not necessarily governed by the need to sustain the Taylor wave action, and proposed that spontaneous bubble nucleation at the liquid-solid interface is the mechanism for the minimum pool film boiling point. Bubble nucleation can be either heterogeneous, in which the vapour bubbles are produced within cavities at a solid-liquid interface as a result of the imperfect wetting of the liquid, or homogeneous, where the bubble nuclei are formed completely within the liquid due to density fluctuations over a duration of 10^{-9} to 10^{-8} seconds.

This mechanism is based on a mechanical stability condition described by Eberhart and Schnyders [32] and Carey [33] for a closed system containing a pure substance which is not in thermodynamic equilibrium, is given as:

$$\left(\frac{\partial P}{\partial v}\right)_T < 0 \tag{2.17}$$

Using the Van der Walls equation of state, the condition of mechanical stability given by 2.17, and the fact that $P_r = P/P_c < 1$ for most fluids at atmospheric conditions, Spiegler et al. [34] derived the thermodynamic homogeneous nucleation temperature limit, T_{thn}, that corresponds to the rewetting temperature:

$$T_{wet,Spielberg} = \frac{27}{32} T_c \tag{2.18}$$

Using equation 2.18 as a starting point, Semeria [35] and Baumeister and Simon [36] implemented some modifications to take into account the subcooling of the liquid and the wall's properties, which play a role during the intermittent contact during the rewetting process.

$$T_{wet,Semeria} \leq \frac{27}{32} T_c + \sqrt{\frac{\lambda \rho C_p|_l}{\lambda \rho C_p|_w}} \left(\frac{27}{32} T_c - T_l\right) \tag{2.19}$$

$$T_{wet,Baumeister} = T_l + 0.29 \left(\frac{27}{32} T_c - T_l\right) \left[e^{\frac{3.06\times10^6}{\lambda \rho C_p|_w}} erfc\left(\frac{1751.5}{\sqrt{\lambda \rho Cp|_w}}\right)\right]^{-1} \tag{2.20}$$

Afterwards, DeSalve and Panella [37] added a term to equation 2.20 to take into account the variation in the rewetting temperature with the flow mass flux. However, this was established for mass fluxes $G < 135.6 kg/m^2 s$, and in our case the mass flux is much higher, which makes this correlation not suitable for our study.

$$T_{wet,DeSalve} = T_l + 0.29 \left(\frac{27}{32} T_c - T_l\right) \left(1 + 0.279 G^{0.49}\right) \left[e^{\frac{3.06\times10^6}{\lambda \rho C_p|_w}} erfc\left(\frac{1751.5}{\sqrt{\lambda \rho Cp|_w}}\right)\right]^{-1} \tag{2.21}$$

More recently, Darr et al. [25] presented a correlation especially for cryogenic fluids that is also a variation of the initial Spielberg's equation:

$$T_{wet,Darr} = \frac{27}{32} T_{cr} \left(1 + c_1 We^{c_2} Re^{c_3 Ja^{c_4}}\right) \tag{2.22}$$

where $Ja = \frac{c_{p,l}(T_{cr} - T_{sat})}{h_{fg}}$, $We = \frac{G^2 D}{\rho_l \sigma}$, c_1 = 0.08, c_2 = 0.01, c_3 = 0.007 and c_4 = 3.

Between these two mechanisms, hydrodynamic instability and homogeneous nucleation, the one that requires the lowest wall temperature to establish a stable film boiling regime is the one that dictates the rewetting temperature. For instance, cryogenic fluids normally require a relatively small level of superheat above the normal boiling point to initiate homogeneous nucleation, therefore its Leidenfrost temperature is dictated by the homogeneous nucleation condition, while for other fluids such as water, hydrocarbons and liquid metals, the stability of the Taylor wave action is probably the limiting mechanism, according to the previously quoted authors.

2.2.3 Critical heat flux

As explained in Konishi and Mudawar [38] and Bruder et al. [39], the majority of the theoretical models to predict the CHF have been developed specifically for vertical upflow in terrestrial conditions, which is the configuration most commonly adopted because it provides stable two-phase flow. Figure 4.20 illustrates the four main mechanisms that have been proposed to trigger flow boiling CHF: Boundary Layer Separation, Bubble Crowding, Sublayer Dryout, and Interfacial Lift-Off.

The Boundary Layer Separation Model uses an analogy between wall gas injection into a single-phase liquid boundary layer and vapour effusion at a heated wall in flow boiling. In the case of single-phase flow, wall injection decreases the liquid velocity gradient near the wall. Ultimately, the gradient becomes increasingly small once the injection velocity reaches a threshold value, causing the boundary layer to separate from the wall. By analogy, the Boundary Layer Separation Model is based on the premise that CHF occurs when the rate of vapour effusion normal to the heated wall reaches a threshold value that causes a significant reduction in the bulk liquid velocity gradient, leading to the separation of the liquid from the wall.

The Bubble Crowding Model is based on the premise that CHF occurs when accumulation of oblong bubbles along the heated wall becomes too dense to permit turbulent fluctuations in the core liquid to provide adequate liquid supply to the wall.

The Sublayer Dryout Model is based on the premise that as CHF is approached, oblong bubbles propagating along the heated wall trap thin liquid sub-layers. CHF is postulated to occur when heat supplied at the wall exceeds the enthalpy of bulk liquid replenishment of the sub-layer.

The Interfacial Lift-off Model is based on the observation that, prior to CHF, vapour patches generated along the heated wall coalesce into a fairly continuous wavy vapour layer. The wavy interface is able to maintain contact with the wall in 'wetting fronts' corresponding to the wave troughs. CHF is postulated to occur when intense evaporation of liquid in the wetting fronts causes the wavy interface to be lifted off the wall, extinguishing any further liquid replenishment.

Incidentally, all these models were thought to explain the critical heat flux phenomenon in a heating process, not quenching.

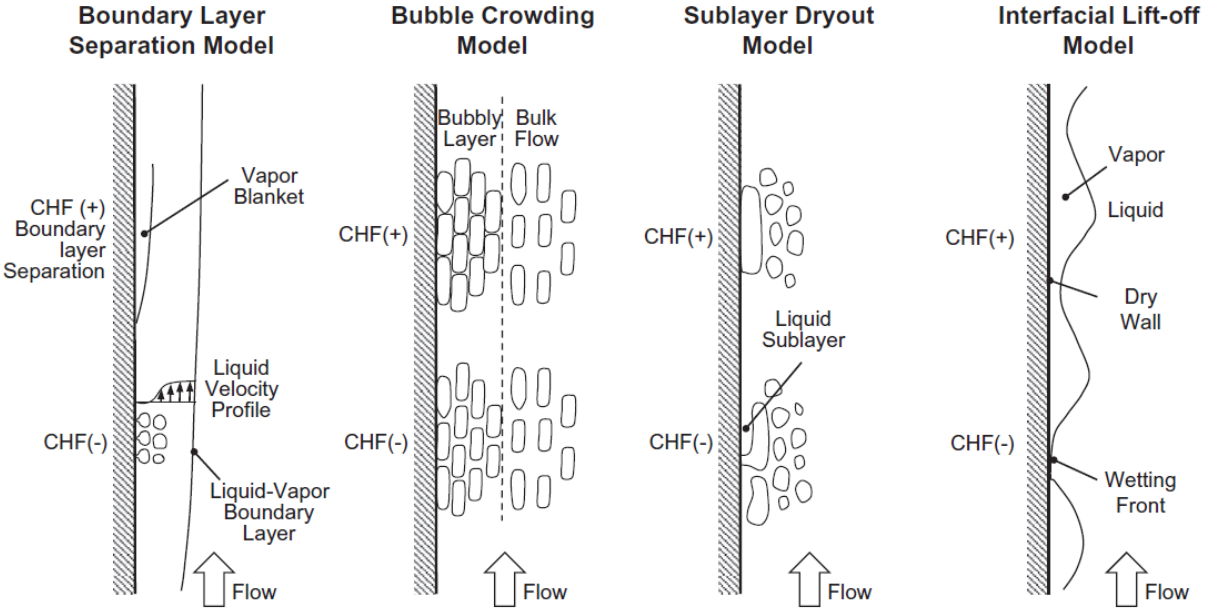

Figure 2.3: Trigger mechanisms for flow boiling CHF according to different models. (source: [38])

In terms of correlations to calculate the critical heat flux, one of the first was proposed by Kutateladze [40] in the context of pool boiling of saturated liquid. This correlation was established by assuming that the vapour generated during boiling is exhausted in the form of columns spaced at a distance equal to a critical half length of the Rayleigh - Taylor instability. The critical flux is then assumed to occur when the interface is deformed by Kelvin - Helmholtz instability.

$$q_{CHF,Kutateladze} = 0.131 \Delta h_{l,v} \rho_v^{1/2} \left(g\sigma(\rho_l - \rho_v)\right)^{1/4} \tag{2.23}$$

Kutateladze [41] later modified this law to take into account the subcooling of the liquid. It was based on the fact that the flow serves both to vaporise the liquid and to heat it up to saturation temperature.

$$q_{CHF,Kutateladze2} = 0.131 \Delta h_{l,v} \rho_v^{1/2} \left(g\sigma(\rho_l - \rho_v)\right)^{1/4} \left(1 + 0.0065 \left(\frac{\rho_l}{\rho_v}\right)^{0.8} \frac{Cp_l(T_{sat} - T_l)}{\Delta h_{l,v}}\right) \tag{2.24}$$

Haramura and Katto [42] proposed a correlation in convective flows around cylinders, adopting the same model of critical flux occurring at interface destabilisation by Kelvin-Helmholtz type instability. They therefore modified equation 2.23 to take mass flow into account. They also involved a length L representing the length of the element considered. Indeed, they observed that the critical heat flux in stationary flow depended on the diameter of the cylinder, with higher values of heat flux for smaller diameters.

$$q_{CHF,Haramura\&Katto} = 0.175 G \Delta h_{l,v} \left(\frac{\rho_v}{\rho_l}\right)^{0.467} \left(\frac{\sigma \rho_l}{G^2 L}\right)^{1/3} \tag{2.25}$$

The most classically used correlations are probably those obtained by Katto and Ohno [43] and by Shah [44]. These two correlations are quite complex, because they take into account transitions for different values of the flow parameters. They were both obtained for stationary flows in uniformly heated vertical tubes, and were established by correlating different characteristic dimensionless numbers, namely the boiling number, the subcooling Jakob number, the ratio of the length of the heated tube to its diameter L/D, as well as the ratios of certain physical properties of liquid and vapour.

The correlation from Shah [44] takes into account some additional physical properties, such as phase viscosity, and also depends on the L/D ratio. However, the surface tension is not taken into account. The author compared this law with that of Katto and Ohno [43] and found a better agreement for data from the literature obtained with water, refrigerants and cryogenic fluids.

One decade later, Hall and Mudawar [45] also proposed a correlation based on the dominant non-dimensional numbers (equation 2.26), with the difference that the length of the heated tube is not involved while the Weber number is.

$$q_{CHF,Hall\&Mudawar} = 0.0722 G \Delta h_{l,v} We_l^{-0.312} \left(\frac{\rho_l}{\rho_v}\right)^{-0.644} \left(1 - 0.9 \frac{Cp_l (T_{sat} - T_l)}{\Delta h_{l,v}} \left(\frac{\rho_l}{\rho_v}\right)^{0.724}\right) \tag{2.26}$$

More recently, Darr et al. [24] presented a new CHF correlation for cryogenic fluids, which is a modified form of the correlation proposed in Katto and Kurata [46] and takes the following form:

$$q_{CHF,Darr} = c_1 G \Delta h_{l,v} We_l^{-0.5} \left(\frac{\rho_l}{\rho_v}\right)^{-0.91} \left(\frac{L}{D}\right)^{0.48} \left(1 + 0.07 We_l^{0.35} \frac{\Delta h_{sub}}{\Delta h_{l,v}}\right) \tag{2.27}$$

where $\Delta h_{sub} = h(T_{sat}) - h(T_l)$, $We_l = \frac{G^2 L}{\rho_l \sigma}$ and c_1 is a constant equal to 1.0 for vertical upwards flows and equal to 0.741 for flows under microgravity conditions.

Two years ago Huang and Kharangate [47] presented a new mechanistic model for predicting the CHF in flow boiling. This is the most complex model and also the most difficult to implement, since it is based on three sub-models which together are used to determine the trigger mechanism that leads to the critical heat flux. First, a separated flow model is used to determine the variations of average velocities and thicknesses of the liquid and vapour layers along the channel. Second, the results from the separated flow model are used to predict the critical wavelength for the transition to the stability of the vapour layer in the wetting front. Third, a CHF trigger mechanism is determined by calculating a heat flux required to simultaneously trigger the critical wavelength of the vapour wave and the Helmholtz wavelength in the wetting front.

Finally, it is important to mention the effect of instationarity in the CHF. Having as reference the value of CHF in a quasi steady-state configuration where the wall temperature is imposed constant, it was reported by Auracher and Marquardt [48] a significant increase in the CHF for the case where the wall temperature is increasing. Similarly, when the wall temperature is being cooled, the CHF also decreases. The results from Auracher and Marquardt [48] are presented in figure 2.4 and shows the important role played by instationarity in the CHF.

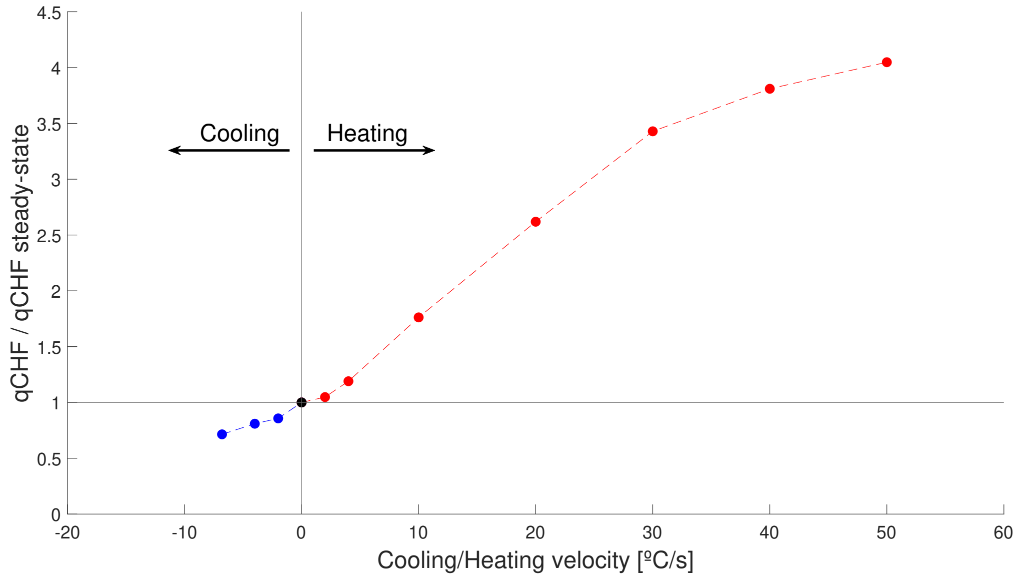

Figure 2.4: CHF results from [48].

2.2.4 Nucleate boiling

There has been a significant amount of work for nucleate boiling correlations development. Since this regime is characterised by a direct contact between the wall and the liquid, simultaneously with the creation of vapour bubbles at nucleation sites, the most widely accepted correlations are generally a superposition of boiling due to nucleation and forced convection. This approach, first suggest by Chen [49], is to consider the heat transfer coefficient as the sum of a microscopic contribution (nucleation) and a macroscopic contribution (forced convection).

The term accounting for the forced convection is usually predicted by the correlation of Dittus and Boelter [50] described in equations 2.28 and 2.29 for the heating and cooling configurations, respectively.

$$Nu = \frac{h_{fc}D}{\lambda_l} = 0.0243Re^{0.8}Pr^{0.4} \tag{2.28}$$

$$Nu = \frac{h_{fc}D}{\lambda_l} = 0.0265Re^{0.8}Pr^{0.3} \tag{2.29}$$

The most popular model for the prediction of the flux contribution from nucleation is that of Rohsenow (1952) described in equation 2.30.

$$q_{nb,Rohsenow} = \mu_l \Delta h_{l,v} \left[\frac{g(\rho_l - \rho_v)}{\sigma}\right]^{1/2} Pr^{-s/r} \left[\frac{Cp_l[T_w - T_{sat}(p_l)]}{C_{sf}\Delta h_{l,v}}\right]^{1/r} \tag{2.30}$$

where r = 0.33, s = 1.0 for water and 1.7 for other fluids, and the constant C_{sf} may vary from one fluid-surface combination to another. The known values of C_{sf} for the studied fluid-surface combinations are presented in Carey [19] and vary between 0.0022 and 0.02. Regarding the use of this correlation in microgravity, Dhir [51] suggested the use of $g = 9.81 m/s^2$ even under microgravity conditions.

In the original formulation by Chen [49], the microscopic and macroscopic contributions are given by expressions the 2.31 and 2.32, respectively. The first one corresponds to the Forster-Zuber [52] correlation, created to calculate the heat transfer coefficient for nucleate pool boiling, but it is multiplied by a suppression factor, S, that accounts for the fact that as the macroscopic convective effect increases in strength, the nucleation is more strongly suppressed. The second one corresponds to a modification of the Dittus-Boelter equation.

$$h_{mic} = 0.00122 \left[\frac{k_l^{0.79} Cp_l^{0.45} \rho_l^{0.49}}{\sigma^{0.5} \mu_l^{0.29} \Delta h_{l,v} \rho_v^{0.24}} \right] \left[T_w - T_{sat}(p_l) \right]^{0.24} \left[p_{sat}(T_w) - p_l \right]^{0.75} S \tag{2.31}$$

$$h_{mac} = 0.023 \left(\frac{k_{tp}}{D} \right) Re_{tp}^{0.8} Pr_{tp}^{0.4} \tag{2.32}$$

where $k_{tp} = k_l$, $Pr_{tp} = Pr_l$ and Re_{tp} is given by the expression 2.33, which depends on the function of the Martinelli factor, whose formula depend on the value of the Martinelli factor itself and are presented in equations 2.35 and 2.36. To decide which expression one should use, the Martinelli factor can be calculated using equation 2.34.

$$Re_{tp} = Re_l \left[F(X_{tt}) \right]^{1.25} \tag{2.33}$$

$$X_{tt} = \left(\frac{1-x}{x} \right)^{0.9} \left(\frac{\rho_v}{\rho_l} \right)^{0.5} \left(\frac{\mu_l}{\mu_v} \right)^{0.1} \tag{2.34}$$

From a regression analysis of the available data at the time, Chen obtained $F(X_{tt})$ and $S(Re_{tp})$ curves that provided a best-fit for his correlation. Originally, the curves were only presented in graphical form, but later Collier [53] proposed the following empirical expressions to fit the Chen's original graphical curves:

$$F(X_{tt}) = 1 \quad \text{for } X_{tt}^{-1} \leq 0.1 \tag{2.35}$$

$$F(X_{tt}) = 2.35 \left(0.213 + \frac{1}{X_{tt}} \right)^{0.736} \quad \text{for } X_{tt}^{-1} > 0.1 \tag{2.36}$$

$$S(Re_{tp}) = \left(1 + 2.56 \times 10^{-6} Re_{tp}^{1.17} \right)^{-1} \tag{2.37}$$

Solving equation 2.34 for the value of quality that results in a X_{tt} higher than 10, it can be found that the value of $F(X_{tt})$ is given by expression 2.35 as long as $x < 8.25 \times 10^{-3}$. Regarding our experiments, Brian Verthier [16] estimated the quality both in normal gravity and microgravity conditions, in the whole range of mass flux, and concluded that $x < 3 \times 10^{-3}$ for all cases. Therefore, $F(X_{tt}) = 1$.

One fundamental difference between the nucleate boiling correlation from Rohsenow and the one from Chen is the fact that the first was created for subcooled nucleate boiling, which is our case, while the second applies to saturated nucleate boiling. Recently, Scheiff et al. [54] conducted experiments with

HFE7000 and studied the subcooled nucleate boiling regime. To take into account the liquid subcooling, equation 2.31 is multiplied by a factor S_{sub} given by:

$$S_{sub} = 1 + 3.27 \times 10^{-4} \cdot Ja_{sub}^2 \tag{2.38}$$

Furthermore, the authors proposed a modification in Chen's expression for the forced convection, presented in equation 2.39, that consisted in changing the exponent of the Prandtl number in order to fit better the experiments with refrigerant liquids.

$$h_{mac} = 0.023 \left(\frac{k_l}{D}\right) Re_{tp}^{0.8} Pr_{tp}^{0.696} \tag{2.39}$$

Klimenko also investigated two-phase forced flows [55] [56], and in 1990 [57] presented the final form of his correlations for nucleate boiling heat transfer (equation 2.40) and for the forced convection vaporisation heat transfer (equation 2.41). These correlations do not take into consideration the fluid subcooling.

$$Nu_{nb,Klimenko} = C Pe_*^{0.6} K_p^{0.54} Pr_l^{-1/3} K_i^{0.12} \tag{2.40}$$

$$Nu_{fc,Klimenko} = 0.087 Re_m^{0.6} Pr_l^{1/6} \left(\frac{\rho_v}{\rho_l}\right)^{0.2} K_i^{0.09} \tag{2.41}$$

where $Pe_* = \frac{qLb}{\Delta h_{lv} \rho_v \alpha_l}$, $Lb = \sqrt{\frac{\sigma}{g(\rho_l - \rho_v)}}$, $K_p = \frac{pLb}{\sigma}$, $K_i = \frac{\lambda_w}{\lambda_l}$, $Re_m = \left(\frac{G}{\rho_l}\right) \cdot \left[1 + x\left(\frac{\rho_l}{\rho_v} - 1\right)\right] \cdot \frac{Lb}{\nu_l}$, and the value of C depends on the type of fluids. For freons and cryogenic fluids, $C = 7.6 \times 10^{-3}$ and $C = 6.1 \times 10^{-3}$, respectively.

In 1991, Liu and Winterton [58] presented a set of equations that can be used to calculate both saturated and subcooled flow boiling, based on the modified form of the Dittus-Boelter (equation 2.43) for the forced convection and on the correlation for pool boiling when the surface finish is unknown from Cooper [59] (equation 2.44). The equations for the subcooled flow boiling are the following:

$$q = \sqrt{(h_L \Delta T_b)^2 + (S h_{pool} \Delta T_s)^2} \tag{2.42}$$

$$where: h_L = 0.023 Re_L^{0.8} Pr_l^{0.4} \tag{2.43}$$

$$h_{pool} = 55 \left(\frac{p}{p_c}\right)^{0.12} \cdot [h_{pool}(T_w - T_{sat})]^{2/3} \left[-\log_{10}\left(\frac{p}{p_c}\right)\right]^{-0.55} \cdot M^{-0.5} \tag{2.44}$$

$$S = (1 + 0.055 Re_L^{0.16})^{-1} \tag{2.45}$$

$$\Delta T_b = T_w - T_l \tag{2.46}$$

$$\Delta T_s = T_w - T_{sat} \tag{2.47}$$

Regarding correlations created specifically for cryogenic fluids, two expressions were recently presented, one by Darr et al. [24] and the other by Kuang et al. [60]. Both of them apply for saturated nucleate flow boiling, not taking into account subcooling. The first (equation 2.48) was based in LN2 and LH2 data and it is a modification of Chen's expression for the forced convection. The Jakob number was included to account for the relative importance of latent to sensible energy during this phase of chilldown, the Weber number to take into consideration the surface tension of LN_2 or LH_2, and the Archimedes number to include the effects of the bubbles' dynamics.

$$h_{nb,Darr} = c_1 Pr_l^{c2} Ja_l^{c3} We_l^{c4} Ar^{c5} \cdot \left(0.023\frac{\lambda_l}{D}Re^{0.8}Pr^{0.4})\right) \tag{2.48}$$

where $We_l = \frac{G^2 D}{\rho_l \sigma}$, $Ar = \frac{\rho_l g(\rho_l - \rho_v)D^3}{\mu_l^2}$, and where $c_1 = 2.14 \times 10^{-7}$, $c_2 = 4.895$, $c_3 = 0.393$, $c_4 = -0.284$ and $c_5 = 0.749$ for vertical upwards flows in normal gravity, and $c_1 = 0.14 \times 10^{-7}$, $c_2 = 5.900$, $c_3 = 1.200$, $c_4 = -0.220$ and $c_5 = 0.880$ for microgravity conditions.

The second equation (2.49) also consists in a modification of Chen's expression for the forced convection, this time corrected by the Boiling number, Bo. The reported application scope are flows with a $Bo \in [8.37 \times 10^{-5}; 2.33 \times 10^{-3}]$. However, in the case of chilldown, since the wall heat flux is not constant with time, Bo number-based correlations might not be very suitable.

$$Nu_{nb,Kuang} = 406.3Bo^{0.6162} \cdot 0.023Re^{0.8}Pr^{0.4} \tag{2.49}$$

$$\text{where } Bo = \frac{q}{G\Delta h_{l,v}} \tag{2.50}$$

Interestingly, both correlations use the variation of Dittus-Boelter expression for the forced convection with the value of 0.4 as the exponent of the Prandtl number, which was supposedly for the heating and not quenching case.

Chapter 3

Experimental Apparatus and Procedure

This chapter will present the experimental set-up designed, built and tested in the scope of a PhD thesis [16] by Mr. Brian Verthier and Prof. Dr. Catherine Colin, his supervisor. All the experimental data used in the present work comes from this experiment that took place in 2009, therefore it is interesting to understand its fundamentals.

3.1 How parabolic flights work

As it can be seen observed from figure 3.1, one complete parabola has four main phases and lasts around 1 minute in total. From a stabilised level-flight at 6000 metres, the aircraft gains attitude. During this phase, called parabola pull-up, passengers experience a pull of 1.8 times that of gravity on Earth. This is called hypergravity. The flying crew then performs a manoeuvre called “injection”: as the aircraft travels upwards, the pilots reduce engine speed and the aircraft follows a ballistic trajectory. After a transition period of around 5 seconds during which the vertical load factor goes from 1.8g to null, the microgravity conditions last for about 22 seconds during which the aircraft seems to be in ”free fall”. In reality, the pilot adjusts the control stick tilt to maintain the vertical load factor at zero, while the lateral acceleration is controlled by an automatic piloting, and a mechanician adjusts the thrust of the engines to cancel the longitudinal load factor. Together, all three pilots maintain a near-zero acceleration level in the three axes to guarantee zero-gravity precision ± 0.02 g. An exit phase at 1.8 g, symmetrical with the entry phase, is then performed on the descending part of the parabola within about 20 seconds to return the aircraft to a stabilised altitude level.

Despite the short duration of the microgravity phase during each parabola, it is possible to accumulate up to 10 minutes of recorded data per flight since the aircraft makes 30 parabolas. These are separated into 6 groups of 5, and a two-minute gap is left between two successive parabolas to allow scientists and pilots to prepare for the next parabola. Between each group of parabolas, there is a five-minute pause. [61], [62]

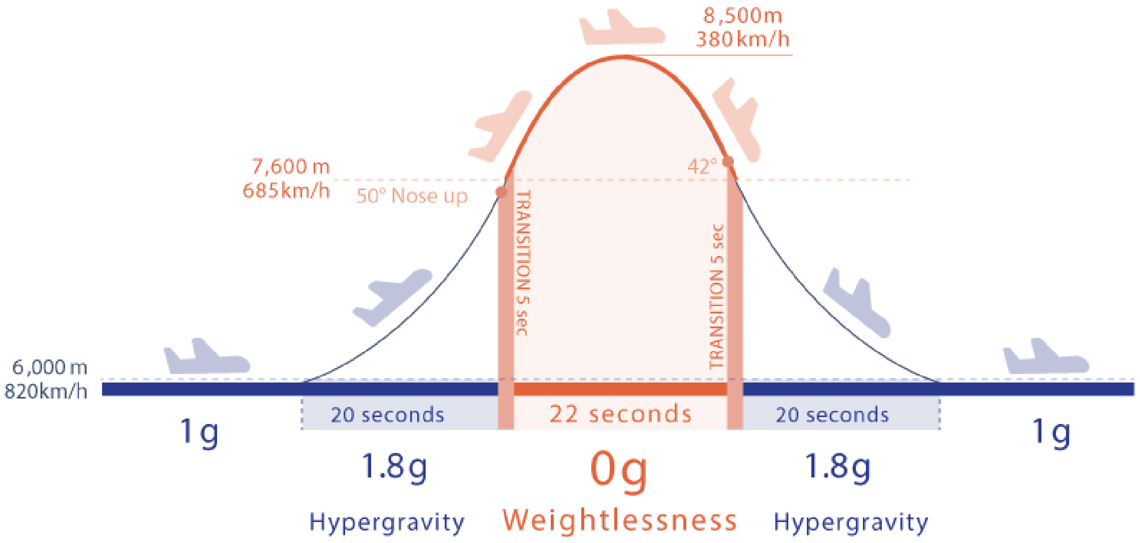

Figure 3.1: Phases of a parabolic flight. (source: Novespace's website [62])

3.2 Working fluid

The fluid used was the 3M™ Novec™ 7100 Engineered Fluid [63] (HFE7100), which is part of a new generation of refrigerant fluids from the hydrofluoroethers family that are suitable to use in place of older refrigerant fluids such as R113 and R123. The main advantage of this new generation of fluids is the fact they are less harmful for the environment.

This fluid was chosen for its very low surface tension and viscosity, that make it one of the non cryogenic fluids whose physical properties are closest to the ones from liquid oxygen and liquid hydrogen. Furthermore, its low boiling point at 61 °C makes it suitable for boiling experiences. Finally, the other reason for which this fluid was selected was the fact that, for safety reasons during the parabolic flight, it was necessary to use a fluid whose behaviour at high temperatures was known. Incidentally, Tuma and Tousignant [64] had already shown in a previous study that the continuous exposition to high temperatures did not generate a dangerous quantity of toxic decomposition products.

3.3 Experimental set-up

As described in [65], the experimental apparatus is a classical two-phase flow loop that can be divided in two main loops:

- The hydraulic one is a closed loop in which the fluid circulates at a given mass flow rate, temperature and pressure.
- The air loop is used to impose the fluid loop pressure. This pressurisation is made by means of a bellows (component Ta1 in the figure 3.2), which is in contact with air on one side, and with HFE7100 on the other.

The main components of the hydraulic section are shown in figure 3.2. In the circuit, the refrigerant pressure varies from 0.8 to 2 bar and the liquid subcooling from 5 to 15℃.

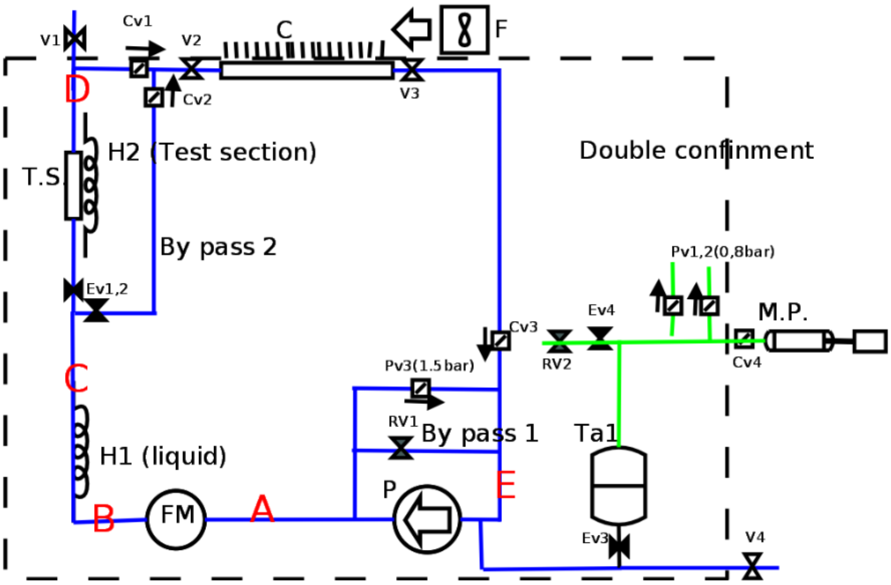

Figure 3.2: Scheme of the two-phase flow loop used in the experiment.

The hydraulic circuit consists of a main loop, containing the test section (T.S), a condenser (C) to condense the vapour generated during the quenching, a preheater (H1), a pump (P), and two bypass valves (1 & 2). The bypass 1 is used to set up the mass flow rate. The bypass 2 is used to choose if the fluid passes through the test section or not. The branch choice is made by two normally closed electro-valves (Ev 1,2).

The test section is a stainless steel tube, with a 10mm inner diameter, a 1mm thickness and a 10cm length, heated by three resistive heating tapes (figure 4). 15 k-type thermocouples are attached to the test section outer surface. A k-type thermocouple in inside the test section to measure the liquid temperature. The test section is located between two thermoplastic insulating bridles. In each bridle, two O-ring electrodes are flush-mounted to measure the void fraction from a capacitance method. A k-type thermocouple passes through each bridle to measure inlet and outlet liquid temperatures.

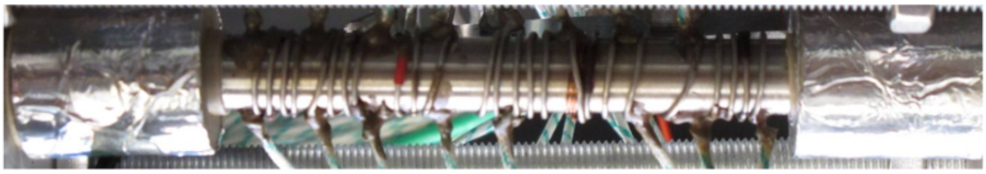

Figure 3.3: Test section.

During each parabola, the quenching trial of the test section is divided into 3 phases:

1. Regulation phase: This phase takes place during the five-minute pauses between groups of

parabolas, and it is used to modify the global temperature of the circuit. This operation is long and costly in terms of energy consumption, since not only it is necessary to change the temperature of the working fluid, but also the temperature from another components such as the circuit's lines or the pump. During this phase, all the HFE7100 is in the liquid state and circulates via the bypass.

2. Adjustment phase of the test parameters: Two minutes before each quenching trial, the mass flux and the pressure are modified to the desirable values. Simultaneously, the test section is heated and the liquid inside it is vaporised. The vapour generated by the heating of the test section is evacuated using the one-way valve located after the pyrex tube, and then it is condensed by the condenser.

3. Quenching phase: At the beginning of the microgravity period, the test section is full of vapour and heated to a temperature of 180℃. At the same time, the heating is switched off and the working fluid is deviated from the by-pass and starts passing through the branch line containing the test section. This marks the beginning of the quenching. The vapour generated during the trial is evacuated and re-condensed. At the end of this phase, the liquid is deviated to the bypass and the second phase starts all over again.

3.4 Description of the metrology used

The measures required to analyse the quenching process, calculate the heat flux and the rewetting temperature are listed below. In addition, the measurements of quantities more relevant to this work will be explained more in detail. A general scheme of the metrology used is presented in figure 3.4.

- The in-flight acceleration felt by the experimental apparatus.
- The mass flux.
- The pressure at the inlet of the test section.
- The pressure difference between the inlet and the outlet of the test section.
- The temperature of the working fluid, both at the inlet and outlet of the test section.
- The wall temperature along the test section.
- The void fraction.

3.4.1 Thermal measurements

The temperature of the liquid phase of the fluid is measured at the inlet and outlet of the test section by two k-type sheathed thermocouples (TI1 and TI2). A third thermocouple TI3 allows to measure the temperature of the thermoplastic's wall.

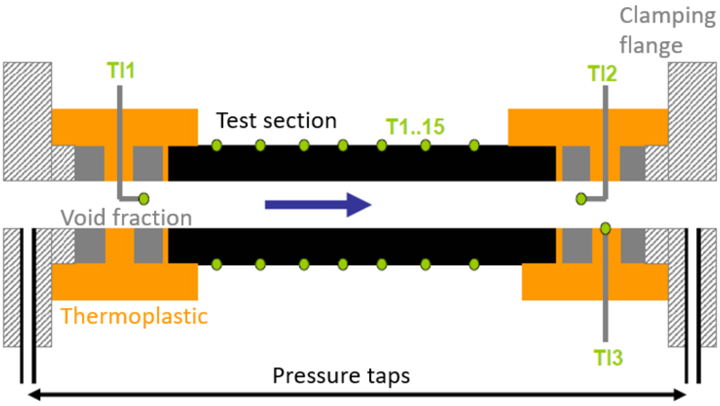

Figure 3.4: Sensors in the test section.

Originally, the maximum error of the thermocouples used was 1 °C. However, since the temperature gradients between the inlet and outlet of the test section were small, of the order of a few degrees, a recalibration of the liquid temperature sensors was done by Brian Verthier. For this, the temperature signal measured from a thermostatic bath was corrected by the measurement made at the thermocouple tip by a PT100 platinum probe. This allowed to reduce the maximum error to 0.1 °C.

Moreover, the temperature of the test section is measured in 15 positions by unsheathed K-type thermocouples. These were fixed to the wall by a thermosetting resin with a high thermal conductivity, ensuring good mechanical strength and correct thermal contact. These thermocouples have a maximum error of 1 ° C, and 3 of them are used to regulate the heating of the section, while the other 12 are used to collect data.

3.4.2 Measurement of the acceleration and mass flow rate

The gravity intensity is measured by a 3-axis accelerometer that can measure a relative acceleration of 2g with an accuracy of 0.3%. This sensor is located approximately 20cm from the test section, and it is attached to the frame of the apparatus.

The flow rate is measured by a Coriolis effect flowmeter capable of measuring a maximum flow rate of 208 m^3/h with an accuracy of 0.75% . This technology was chosen because the fluid being dielectric, the use of an electromagnetic flowmeter was impossible. Likewise, the measure had to not be impacted by the level of gravity.

3.4.3 Pressure measurements

The absolute pressure is measured upstream of the test section and upstream of the pump, the point where the pressure is imposed, by sensors with a range from 0 to 5 bar and a precision of 0.25 mbar. The pressure gradient between the inlet and the outlet of the section is measured between two taps made in the clamps of the latter, using a pressure differential sensor with an accuracy of 0.5%.

3.5 Data processing

3.5.1 Calculation of the wall's internal temperature and heat flux

In order to obtain the temperature of the wall's inner surface, it is necessary to apply an inverse method. In other words, we measured the temperature of the wall on its external surface, while the cooling takes place on its inner surface. A classical resolution cannot then be applied because the boundary conditions on the inner surface are not known.

Numerous analytical solutions are developed in the work of Maillet et al. [66] and have been applied, for example, in the case of the quenching of a plate by an impact jet (Gradeck et al. [67]). This type of method requires the solution of the heat equation in Laplace space and therefore the use of numerical inversion tools that are complicated to set up and often a source of errors.

We are therefore interested in solving the heat equation using a shooting method. The simplified case of the 1D cylindrical unsteady heat equation (3.1) was used, where r is the radial direction, varying between D/2 and D/2+e, and φ is the local flux density in W/m^2. It was also assumed that the temperature is invariant with the angle, which is a reasonable assumption given that the test section is vertical.

$$\frac{1}{r}\lambda_w\frac{\partial r\varphi}{\partial r} = \rho_w Cp_w\frac{\partial T}{\partial t} \tag{3.1}$$

By adopting the discretisation shown in figure 3.5, the surface flux can be expressed as a function of the temperature of each mesh.

$$\varphi_n = \frac{\lambda_w}{dr}\left[T_{n+1} - T_n\right] \tag{3.2}$$

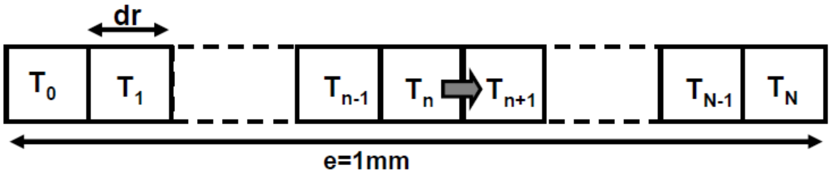

Figure 3.5: Discretization of the wall in 1D Cartesian for inverse problem solving.

By noting Tin the temperature of the mesh n at time i and choosing time and space steps dt and dr, the heat equation can be discretised according to equation 3.3 and written in matrix form according to equation 3.4 with $C = (\lambda_w dt)/(\rho_C p_w dr)$.

$$\begin{aligned}
&\frac{\rho_p Cp_p}{\lambda_p}\frac{\partial T}{\partial t} = \left[\frac{\partial^2 T}{\partial r^2} + \frac{1}{r}\frac{\partial T}{\partial r}\right] \iff \\
\iff &\frac{\rho_p Cp_p}{\lambda_p}\frac{T_n^{i+1} - T_{n-1}^{i}}{dt} = \frac{1}{2r}\left[\frac{T_{n+1}^{i} - T_n^{i}}{dr}\right] + \frac{1}{dr^2}\left[\frac{T_{n+1}^{i} - 2T_n^{i} + T_{n-1}^{i}}{dr}\right] \iff \\
\iff &T_n^{i+1} = T_n^{i} + \frac{\lambda_w dt}{\rho_w Cp_w 2r dr}\left[T_{n+1}^{i} - T_{n-1}^{i}\right] + \frac{\lambda_w dt}{\rho_w Cp_w dr^2}\left[T_{n+1}^{i} - 2T_n^{i} + T_{n-1}^{i}\right]
\end{aligned} \tag{3.3}$$

$$\begin{pmatrix} T_1^{i+1} \\ T_2^{i+1} \\ \vdots \\ T_{N-1}^{i+1} \\ T_N^{i+1} \end{pmatrix} = \begin{pmatrix} \frac{C}{2r}+\frac{C}{dr} & 1-2\frac{C}{dr} & \frac{C}{2r}+\frac{C}{dr} & 0 & \cdots & 0 \\ 0 & \frac{C}{2r}+\frac{C}{dr} & 1-2\frac{C}{dr} & \frac{C}{2r}+\frac{C}{dr} & \ddots & \vdots \\ 0 & \ddots & \ddots & \ddots & \ddots & 0 \\ \vdots & \ddots & 0 & \frac{C}{2r}+\frac{C}{dr} & 1-2\frac{C}{dr} & \frac{C}{2r}+\frac{C}{dr} \\ \vdots & \cdots & 0 & \frac{C}{2r}+\frac{C}{dr} & 1-2\frac{C}{dr} & \frac{C}{2r}+\frac{C}{dr} \end{pmatrix} \times \begin{pmatrix} T_1^{i} \\ T_2^{i} \\ \vdots \\ T_{N-1}^{i} \\ T_N^{i} \end{pmatrix} \tag{3.4}$$

In order to apply an inverse resolution to this system, we will assume known a function $F(t)$ giving the temperature at the internal surface of the wall at time $t = i+1$ as a function of time $t = i$ according to $T_1^{i+1} = F(i) \times T_1^i$. Taking into account this boundary condition, the matrix system is modified according to equation 3.5. Thus, for a given function $F(t)$ we can, according to the established matrix system, calculate the evolution of the temperature $T_N(t)$, outside the wall, by applying the matrix equation to each time step .

$$\begin{pmatrix} T_1^{i+1} \\ T_2^{i+1} \\ \vdots \\ T_{N-1}^{i+1} \\ T_N^{i+1} \end{pmatrix} = \begin{pmatrix} F(i) & 0 & \cdots & \cdots & \cdots & 0 \\ 0 & \frac{C}{2r}+\frac{C}{dr} & 1-2\frac{C}{dr} & \frac{C}{2r}+\frac{C}{dr} & \ddots & \vdots \\ 0 & \ddots & \ddots & \ddots & \ddots & 0 \\ \vdots & \ddots & 0 & \frac{C}{2r}+\frac{C}{dr} & 1-2\frac{C}{dr} & \frac{C}{2r}+\frac{C}{dr} \\ \vdots & \cdots & 0 & \frac{C}{2r}+\frac{C}{dr} & 1-2\frac{C}{dr} & \frac{C}{2r}+\frac{C}{dr} \end{pmatrix} \times \begin{pmatrix} T_1^{i} \\ T_2^{i} \\ \vdots \\ T_{N-1}^{i} \\ T_N^{i} \end{pmatrix} \tag{3.5}$$

Therefore, the method consists of calculating the corresponding external temperature from an internal temperature profile $F(t)$. The error between the calculated and measured profiles is then subtracted from the internal profile (figure 3.6), before iterating the calculation. The initial temperature profile chosen corresponds to a stationary 1D profile $T_1 = T_N - e/\lambda_w Q(z,t)$, where the heat flux $Q(z,t)$ is obtained by assuming a uniform wall temperature (equation 3.6).

$$Q(z,t) \approx \frac{\rho_w A_w C p_w}{P_w} \frac{\partial T_w(z,t)}{\partial t} \tag{3.6}$$

In terms of the precision, this method of calculating the heat flux is not entirely correct because it does not take into account the heat losses that exist. These can be classified into three types: heat losses due to the natural convection with the ambient air, heat losses by radiation, and heat losses caused by the axial conduction along the section test.

The losses by natural convection can be estimated from the Mc-Adams equation 3.7. During the tests in weightlessness, the phenomenon of natural convection disappears and the losses by natural convection are then zero.

$$\begin{aligned} Nu &= 0.547 Ra^{0.25} \\ Ra &= \frac{g\beta D^3 \Delta T}{\nu\alpha} \end{aligned} \tag{3.7}$$

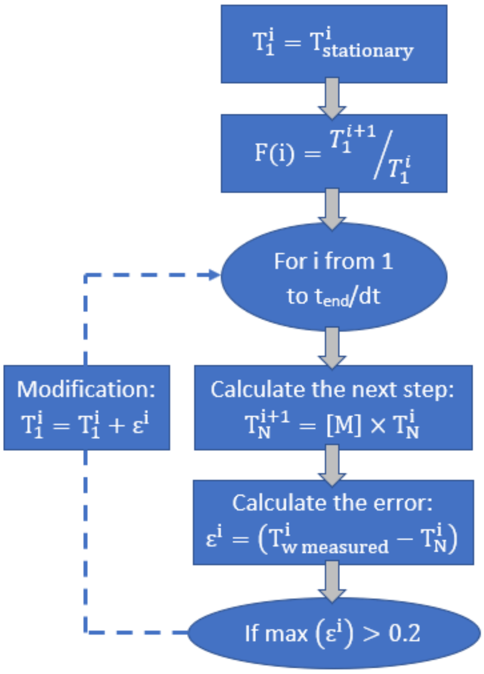

Figure 3.6: Schematic representation of the algorithm to calculate the wall internal temperature.

In terrestrial gravity, these losses are of the order of $2kW/m^2$ for a wall temperature of 200 C. Since the heat flux at film boiling and at CHF are of the order of $15kW/m^2$ and $60kW/m^2$, we can conclude that the losses by natural convection can be neglected during most part of the boiling curve.

The radiation losses can be estimated by Stefan - Boltzmann's law (equation 3.8) where ϵ is the emissivity of the body between 0 and 1, S the radiating surface, σ_{SB} the Stefan - Boltzmann constant equal to $5.67038 \times 10^{-8} W/m^2K^4$, T_p and T_{amb} the temperature of the radiating body and the ambient temperature in Kelvin. Considering that the temperature of the test section is relatively low, these losses can also be neglected.

$$Q_{rad} = \epsilon S \sigma_{SB}(T_w^4 - T_{amb}^4) \tag{3.8}$$

Finally, the losses due to the axial conduction can be estimated by considering the heat fluxes from the neighbouring thermocouples (equation 3.9).

$$Q_{axial}(z) = \frac{\lambda_w S}{\Delta z}\left[T_w(z + \Delta z) + T_w(z - \Delta z) - 2T_w(z)\right] \tag{3.9}$$

Figure 3.7 compares the heat flux calculated through the method previously presented and the heat flux losses caused by axial conduction along the test section. As it is possible to see, the losses are more significant for higher superheats, but they are 10^4 smaller than the calculated heat flux. Hence, they can be neglected.

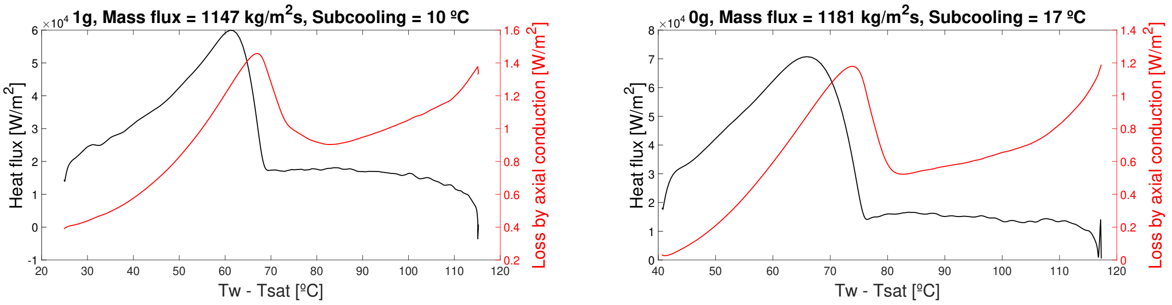

(a) Normal gravity

(b) Microgravity

Figure 3.7: Heat flux losses due to the axial conduction along the test section.

3.5.2 Rewetting temperature

The calculation of the rewetting temperature from the experimental data obtained is not straightforward. In fact, the rewetting process is not instantaneous, which means that there is not a well-defined temperature value above which the wall is dry and below which the wall is wet. What happens is that there is a range of temperatures in which there is an intermittent contact between the liquid and the wall, as it was observed by Ilyas et al. [68] using water and by Yuan et al. [69] using liquid nitrogen. This intermittent process is part of the transition regime between the film boiling and the nucleate boiling.

In the plot of the wall temperature as a function of time (figure 3.8), one can observe that the rewetting phenomenon results in a change of the curve's slope. However, since that change is not instantaneous, the question of where should one consider the rewetting point is raised.

In the literature, different approaches can be found. The first definition by Chen et al. [70] says that the rewetting temperature can be found by the intersection of the curves with the slopes of the film boiling and nucleate boiling regimes. Later, Xu [10] used another definition saying that the rewetting temperature is the one for which the heat flux starts to increase rapidly, corresponding to the beginning of the intermittent contact between the liquid and the wall. Another method used is to consider the temperature at which the maximum temperature variation occurs, which can be easily obtained by taking a second derivative criterion of the maximum temperature.

Implementing the method by Chen [70] in our case can be somewhat difficult, due to the fact that the wall temperature does not have a perfectly linear behaviour with time in film and nucleate boiling regimes. As a consequence, depending on whether one considers an averaged slope over the entire regimes, or just a few seconds near the rewetting point, the rewetting temperature value may vary. In our case, to compute the rewetting temperature using this method, the slope of the film boiling is calculated using the 3 seconds preceding the estimated rewetting point and the slope of the ensemble nucleate/transition boiling regimes is calculated using the 0.5 seconds preceding the critical heat flux, and 2,5 seconds after this point. A shortcoming of this definition is that the rewetting temperature obtained does not correspond to a physically measured temperature. A modification could therefore be made to take into account the physical temperature corresponding to the moment when the slopes intersect.

Concerning the method that uses the second time-derivative of the temperature to calculate the rewetting temperature, it was found by observing 3.8.c) that it had a slight offset with the actual rewetting temperature value. Interestingly, using the minimum value of the third time-derivative it is possible to obtain the rewetting temperature with great precision. Physically, the minimum of third time-derivative represents the point where the ”acceleration” of the temperature reaches a maximum absolute value. In other words, it is the point where the ”acceleration” to decrease the temperature is maximal. This makes sense because the flow is shifting from the film boiling regime, where the heat transfer is low, to the transition/nucleate boiling regime where the heat transfer is much higher, causing a big variation of the temperature’s variation velocity.

To conclude, it appears that the time-derivative based definition is the most robust and the most objective, since it does not involve an arbitrary criterion on the smoothing interval. It can be obtained simply by considering the third time-derivative of the temperature and it is then subject to fewer calculation errors. Therefore, this is the definition of rewetting temperature that will be used in upcoming sections of this work.

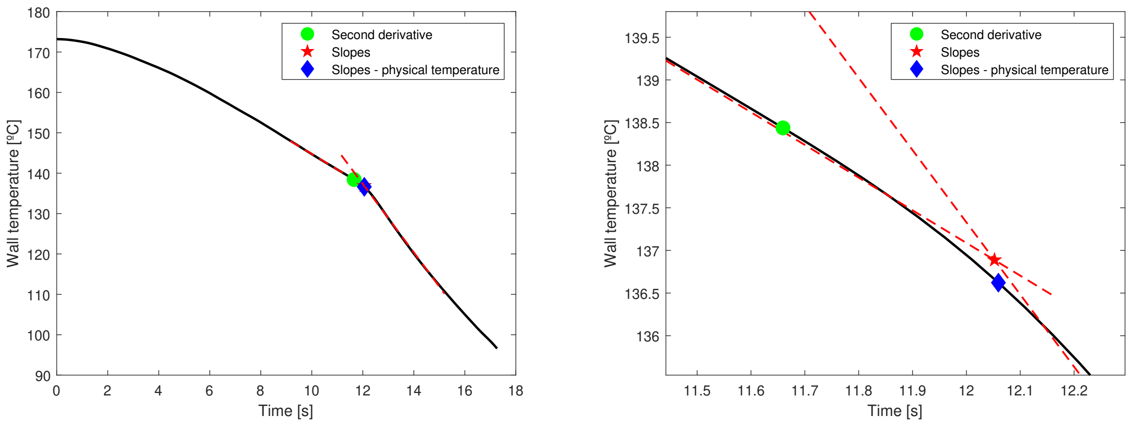

(a) Rewetting temperature from the different methods

(b) Zoom of figure a)

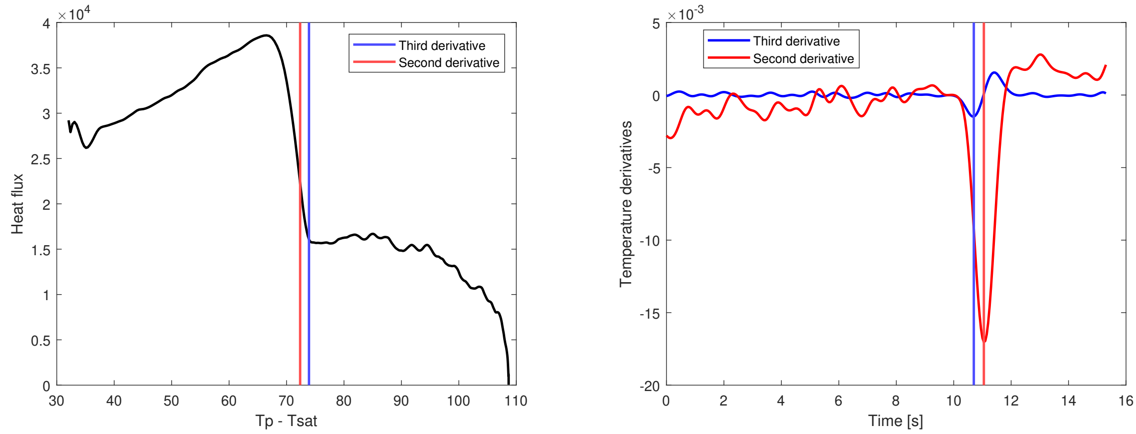

(c) Rewetting temperatures obtained from the second and third time-derivatives in the boiling curve

(d) Second and third time-derivatives of the temperature

Figure 3.8: Comparison of the rewetting temperature calculation methods.

3.5.3 Rewetting velocity

In order to calculate the rewetting velocity, the time difference between the rewetting point of two thermocouples was used. Ideally, this could be done using all 12 thermocouples available in order to access the evolution of the rewetting velocity along the wall. However, as it can be observed in figure 3.9 this is not possible due to the fact that the temperature of the wall is not uniform along the tube. If we consider that, for the same operating conditions, two points have an equal rewetting temperature, it would not be correct to compare points with a different initial temperature because the point with the higher temperature would take longer to reach the rewetting temperature and that time difference would induce an error in the rewetting velocity measurement. Hence, the only solution was to find thermocouples with a close initial temperature and that had a well-defined film boiling regime.

The pair of thermocouples that better check this requirements is formed by thermocouples 7 and 9 (T7 and T9). These are 1cm apart and have an initial temperature between the 170 and 180 ºC in all the experiment trials. The rewetting velocity is then calculated by dividing the distance between T7 and T9 by the time difference between the rewetting instant in those two thermocouples. Furthermore, a selection of the trials was made in order to obtain results as close to reality as possible. This selection was based in two criteria: initial temperature difference between T7 and T9; and rewetting temperature difference between T7 and T9. For both parameters, the maximum difference allowed was 3ºC. As a result, the selection is comprised of 20 trials in microgravity and 34 trials in normal gravity. The results obtained are presented in 4.2.5.

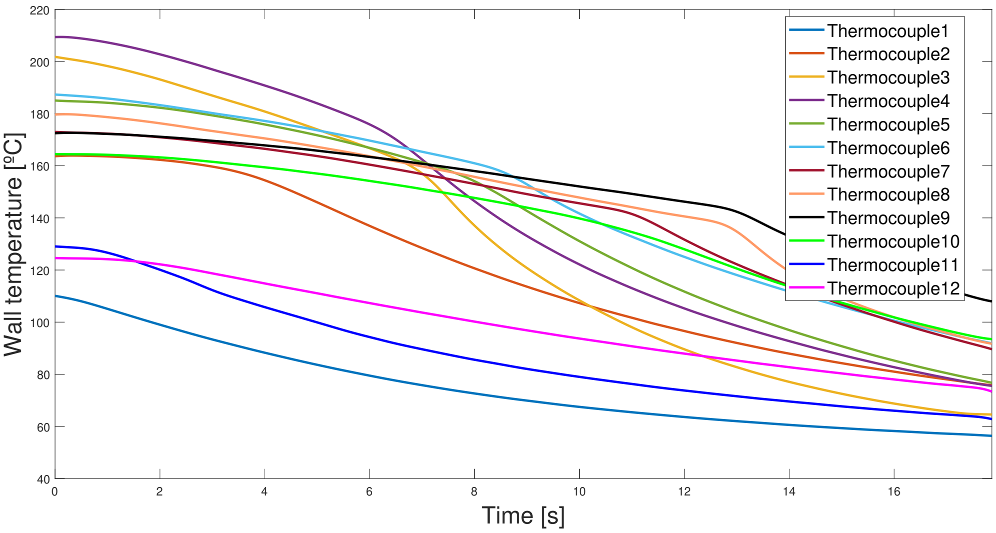

Figure 3.9: Variation of the wall temperature with time for the various thermocouples.

Table 3.1: Position of the thermocouples.

Thermocouple	T1	T2	T3	T4	T5	T6	T7	T8	T9	T10	T11	T12
Position	1 cm	2 cm	3 cm	3 cm	4 cm	5 cm	6 cm	7 cm	7 cm	8 cm	8 cm	9 cm

Chapter 4

Results

4.1 Introduction

Before presenting the results obtained in this study, it is necessary to introduce the boiling curves obtained, which are different from the theoretical boiling curve for saturated water presented in the chapter 2.1.1. Looking at figure 4.1 it is immediate that, unlike what happens in the theoretical curve, in the experimental curves the heat flux does not decrease in the film boiling regime when the difference between the wall and the saturation temperature decreases. In fact, the heat flux is approximately constant, except for the beginning of the curve (when $T - T_{sat}$ is higher) where the heat flux increases abruptly because that is when the flow is injected in the tube and that causes a brief transitory regime.

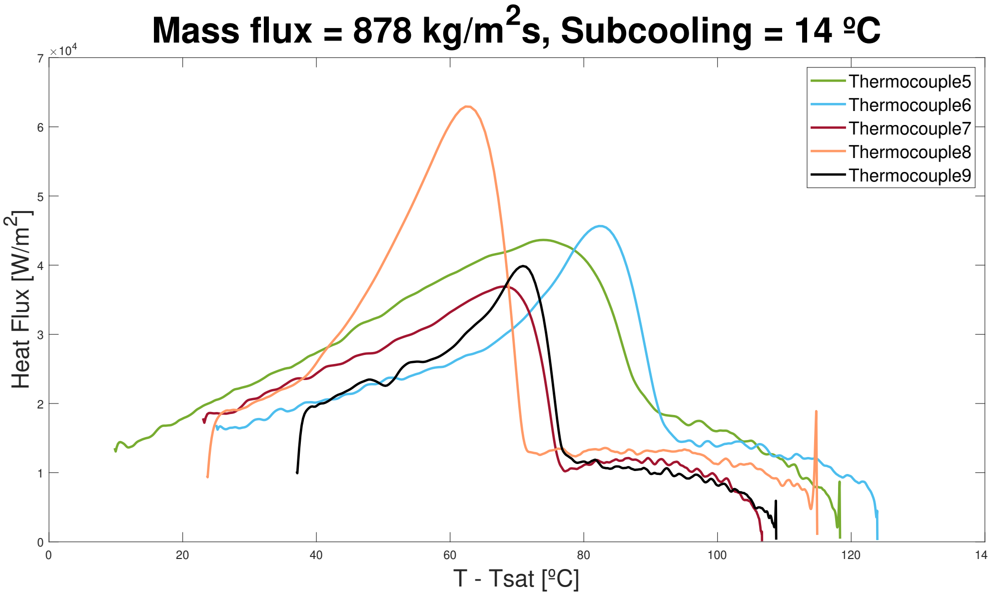

Figure 4.1: Comparison of the boiling curves obtained for different thermocouples.

Moreover, it is clear that the boiling curve can be very different depending on the thermocouple from which the data is obtained. It is very difficult to have perfect experiment conditions and the thermocouples have different initial temperatures like we have already seen in figure 3.9. This factor combined with the different positions of thermocouples along the tube result in the different boiling curves. Having said that, to perform our analysis it was necessary to decide which thermocouple we would use. Looking at figures 4.1 and 3.9, it was decided the thermocouple 8 (T8) was the best since its boiling curve is very well-defined in all the trials (well-marked film boiling with constant heat flux, clear rewetting point, transition boiling and nucleate boiling regimes in accordance to the theoretical model and a distinct peak corresponding to the critical heat flux) and it has an approximately constant initial temperature as well. Therefore, all the results presented from now on were obtained with data from T8, except for the rewetting velocity which was calculated with T7 and T9, as explained in the previous chapter.

In order to characterise the heat exchange coefficients in the different boiling regimes, certain characteristic points of the boiling curve were chosen. These points are used to analyse the relative influence of each parameter on the different boiling regimes as well as for the comparison of measurements with models and correlations in the literature.

Figure 4.3 shows the selected points. Going through the boiling curve from the right to the left, i.e., from the highest superheats to the lowest, one can observe the film boiling point at a superheat of 90ºC, followed by the rewetting point and the critical heat flux point. Finally, there is the nucleate boiling point at a superheat of 55ºC.

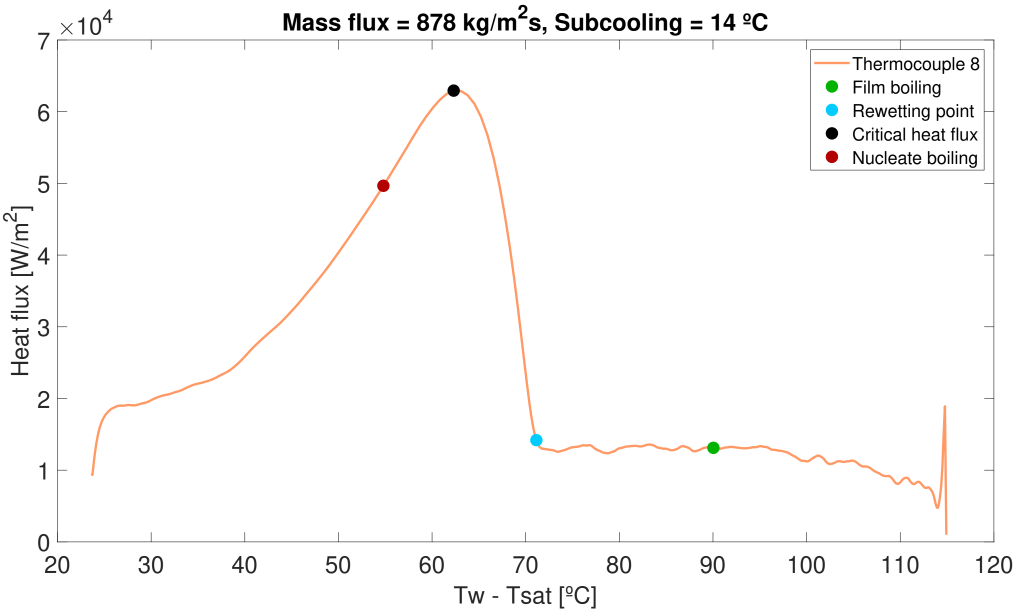

Figure 4.2: Reference points in the boiling curve.

4.2 Parametric Study

Before comparing the experimental data with the results obtained from the various physical models and correlations for each regime of the boiling curve, the experimental data is qualitatively analysed in order to facilitate the understanding of the physical phenomenon. The variables whose impact will be

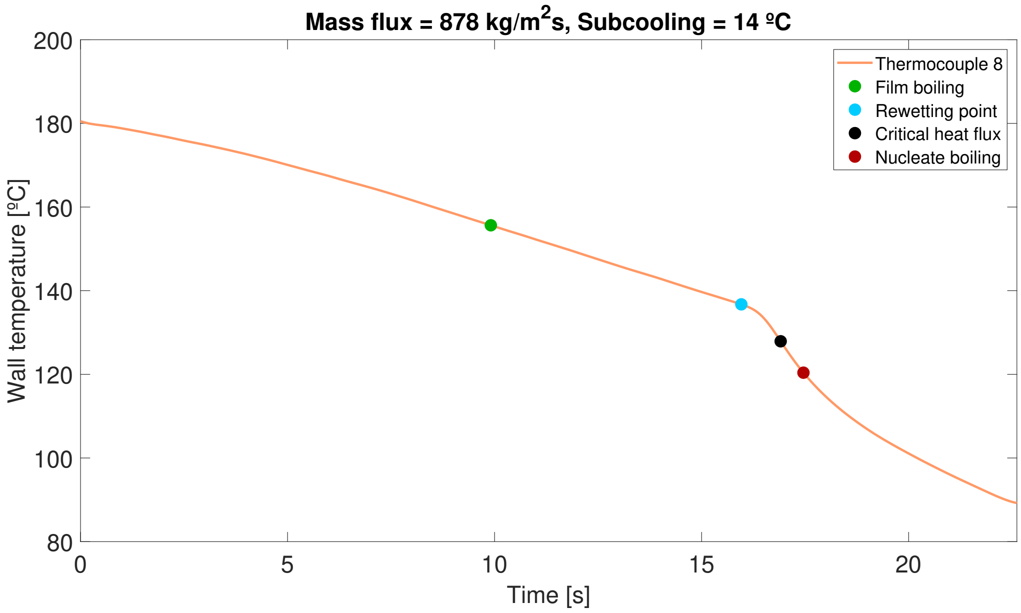

Figure 4.3: Reference points in the temperature vs time curve.

analysed are the following: gravity intensity, mass flux and subcooling.

4.2.1 Film boiling

Looking at figure 4.4 it is possible to understand the impact that these three variables have on the film boiling regime in both gravity intensity levels. Firstly, the heat flux increases for a higher mass flux. However, this augmentation is much more notorious in microgravity conditions, leading to an increase of more than 100% of the heat flux, for the same level of subcooling. On the contrary, an higher level of subcooling seems to have a stronger impact on terrestrial conditions, although it leads to an increase in the heat flux in both conditions. Finally, the impact of the gravity level seems to fade for higher mass fluxes. In fact, for low mass fluxes the heat transfer is between 2 and 3 times greater in normal gravity that in microgravity. This could be explained by the absence of a hydrostatic pressure gradient allowing a better evacuation of the liquid that also results in the narrowing of the liquid core. As a consequence, the thickness of the surrounding vapour film increases, degrading the heat transfer between the wall and the liquid. As previously said, this reduction can be very significant for flows with a very low mass flux, while for flows with higher values of mass flux the heat transfer in terrestrial and reduced gravity are of the same order. This seems logical because the impact of gravity is related to the flow by the Froude number, $Fr = \frac{u_l^2}{\sqrt{gD}}$. For high flow rates, this number is large regardless of gravity intensity, reflecting the dominance of the inertial effects.

4.2.2 Rewetting temperature

Figure 4.5 presents the rewetting temperatures of our trials in both gravity levels. It is possible to see that there is a range of 20ºC, between 130ºC and 150ºC, where the rewetting temperatures are located.

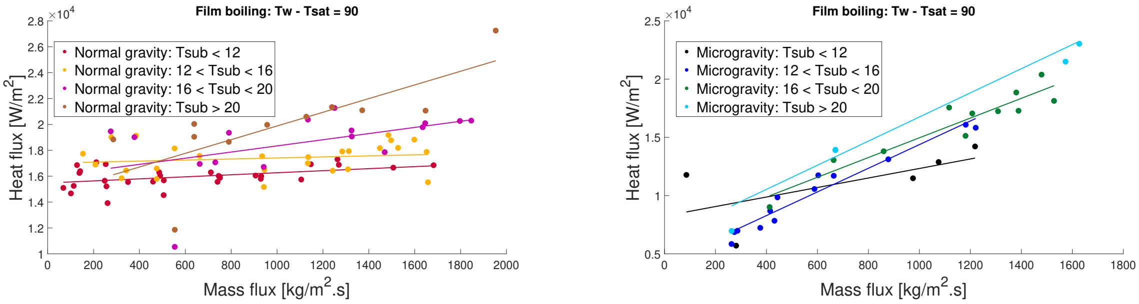

(a) Normal gravity (b) Microgravity

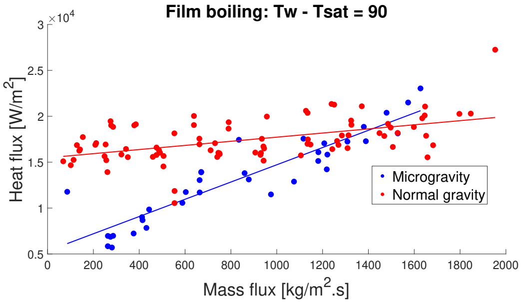

(c) Comparison between gravity levels

Figure 4.4: Experimental results obtained in the film boiling regime.

This variation is quite large and is caused mainly by the variation of flow mass flux and flow subcooling. Of these two parameters, the one that has most impact is the flow subcooling, as it is very clear that the graphs are stratified from the lowest subcooling to the highest subcooling. The mass flow rate effect seems to be similar to all levels of subcooling, resulting in an increase of rewetting temperature in around 5ºC. Regarding the gravity level, it is not easy to draw a clear conclusion because the data points are very dispersed. Nevertheless, the best-fit lines indicate that the rewetting temperature is around 2% lower in microgravity for flows with a very low mass flux. However, this small difference fades for increasingly higher values of mass flux.

4.2.3 Critical heat flux

The experimental data obtained concerning the critical heat flux is shown in figure 4.6. Foremost, the dependency of the CHF on the flow subcooling is clear, since the best-fit lines are stratified according to the subcooling levels. This dependency is observed in both gravity levels, but its magnitude seems greater in normal gravity conditions. Moreover, an increase in the mass flow rate results in a greater CHF.

Finally, the influence of the gravity level is not very well understood. Using the thermocouple T8 (figure 4.6 (c)), the best-fit lines show that the heat transfer is slightly greater in microgravity for the entire range of mass flux, which is in disagreement with some observations from the literature. However, looking at the measurements of thermocouple T4 (figure 4.6 (d)), which has a CHF of the same order of T8 as it can be observed in figure 4.1, the data shows that the CHF is higher in terrestrial conditions for low mass rates. For higher flow velocities the CHF is similar for both gravity levels. From these data,

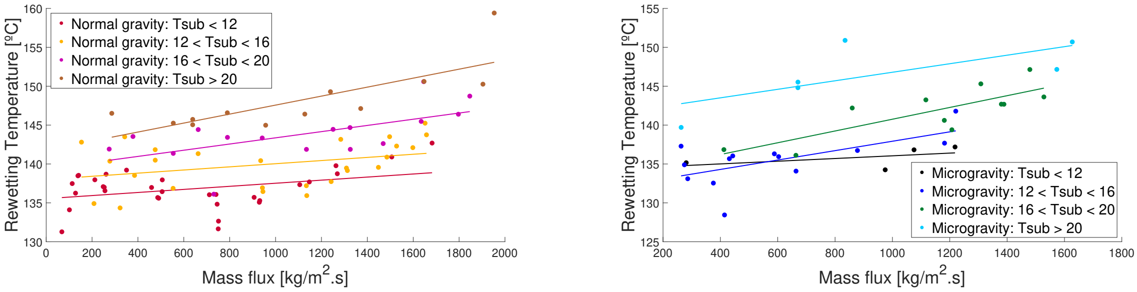

(a) Normal gravity (b) Microgravity

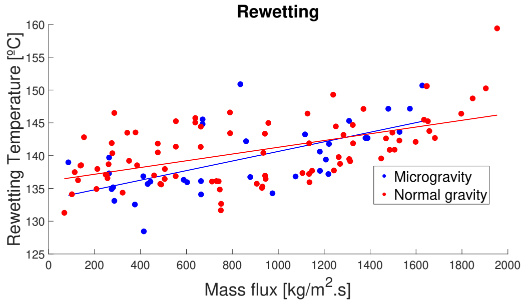

(c) Comparison between gravity levels

Figure 4.5: Experimental results obtained in the rewetting point.

it is difficult to give a clear conclusion on the effect of gravity on the CHF, specially because the CHF models presented in chapter 2.2.3 were developed for boiling curves traversed in the heating sense, not in quenching as it is our case.

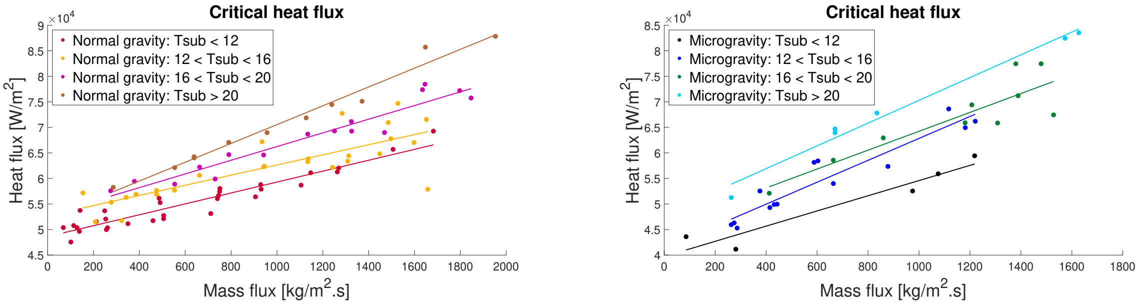

(a) Normal gravity (b) Microgravity

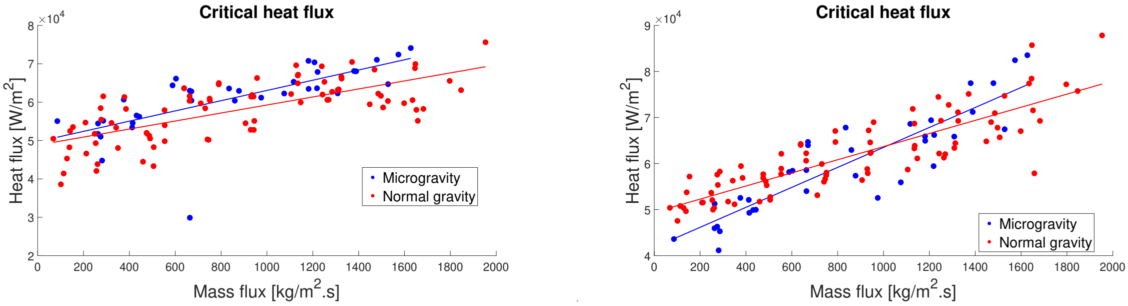

(c) Comparison between gravity levels - T8 (d) Comparison between gravity levels - T4

Figure 4.6: Experimental results obtained in the critical heat flux point.

4.2.4 Nucleate boiling

Finally, the experimental results obtained in the nucleate boiling regime are presented in figure 4.7. Contrary to what has been observed in the previous regimes, the fluid subcooling does not have a strong influence on the heat flux, in both gravity levels. Moreover, it can be observed that in normal gravity an increase in the mass flux translates in an increase in the heat flux. However, that behaviour does not seem to happen in microgravity. The impact of the gravity levels themselves is not clear, as the order of magnitude that does not seem to change regardless of the gravity level.

These different behaviours depending on the gravity conditions might be explained by a competition between the forced convection and nucleate boiling mechanisms. In normal gravity, it seems that the forced convection dominates over the nucleate boiling, leading to an increase in the heat flux with the mass flux. On the other hand, the nucleate boiling mechanism seems to be more important in microgravity, which results in a heat flux that is more independent of the mass flux and subcooling. This is accordance with the results in microgravity.

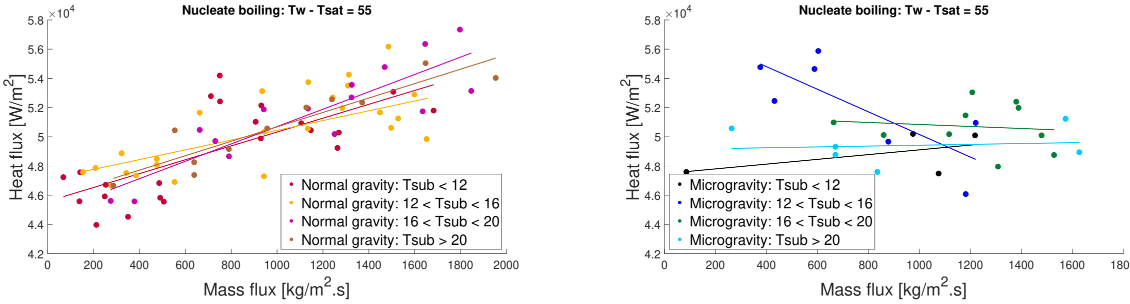

(a) Normal gravity (b) Microgravity

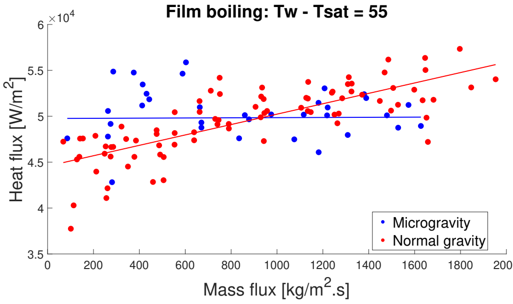

(c) Comparison between gravity levels

Figure 4.7: Experimental results obtained in the nucleate boiling regime.

4.2.5 Rewetting velocity

As it can be seen in figure 4.8, the rewetting velocity seems to decrease in microgravity conditions. This is in accordance to what was observed by Celata et al. [13], where the rewetting velocity was reported to be in the range of 5 to 7 mm/s under microgravity and in the range of 5 to 18 mm/s, for flows with a mass flux between 100-400 kg/m^2s. In our case, the range is from 4 to 8 mm/s for microgravity, and from 6 to 12 mm/s for normal gravity conditions. Despite the fact that the results have a considerable error margin, the rewetting velocity have the same order of magnitude. Interestingly, Westbye et al. [9]

reported a slight increase in the rewetting velocity under microgravity conditions.

It is believed that the decrease in the rewetting velocity is a consequence of the decrease in the heat transfer under microgravity conditions that the experimental data obtained shows. In fact, it makes sense that, for a lower heat transfer, the rewetting velocity is also lower, because the rewetting process takes a longer time to complete. Moreover, it is difficult to draw a conclusion regarding the impact of the mass flux in the rewetting velocity. In both gravity levels the rewetting velocity seems to vary between the same interval of values for the entire range of mass flux.

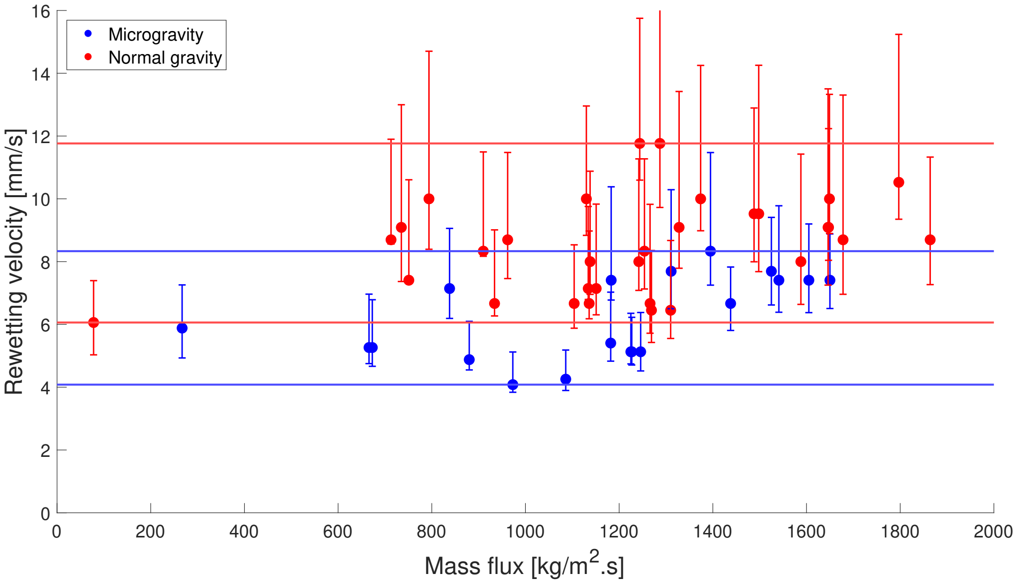

Figure 4.8: Rewetting velocity as a function of the mass flux for different gravity levels.

Furthermore, the impact of the liquid subcooling on the rewetting velocity is shown in figure 4.9. In addition to the plotting of the points according to 4 ranges of liquid subcooling, the line of best fit calculated using the least square method is also presented for each group of data. There seems to be an increase in the rewetting velocity for a greater liquid subcooling. This trend is clearer in microgravity, since the trend lines in normal gravity intercept each other, possibly due to the two extreme points with a higher rewetting velocity. One reason that makes it difficult to draw a conclusion on the impact of liquid subcooling is the fact that some of the groups of data only have two points, which may not be sufficient to have an accurate view of the results.

Finally, to compare the rewetting velocity of refrigerant fluids against cryogenic fluids, the published data from Darr et al. [24] related to the trials in microgravity using liquid nitrogen as a working fluid was used. From the 10 trials available, 3 of them reached the rewetting point before the end of the microgravity period. For those 3 trials, the velocities obtained were the following: 94.5, 90.0 and 65.17 mm/s for values of mass flux equal to 304.38, 375.26 and 503.06 kg/m^2s. In this experiment the liquid was not subcooled. These results show that the rewetting velocity is around 10 times higher for liquid nitrogen than for the refrigerants HFE7100 and FC-72, emphasising the difference between these two types of fluids.

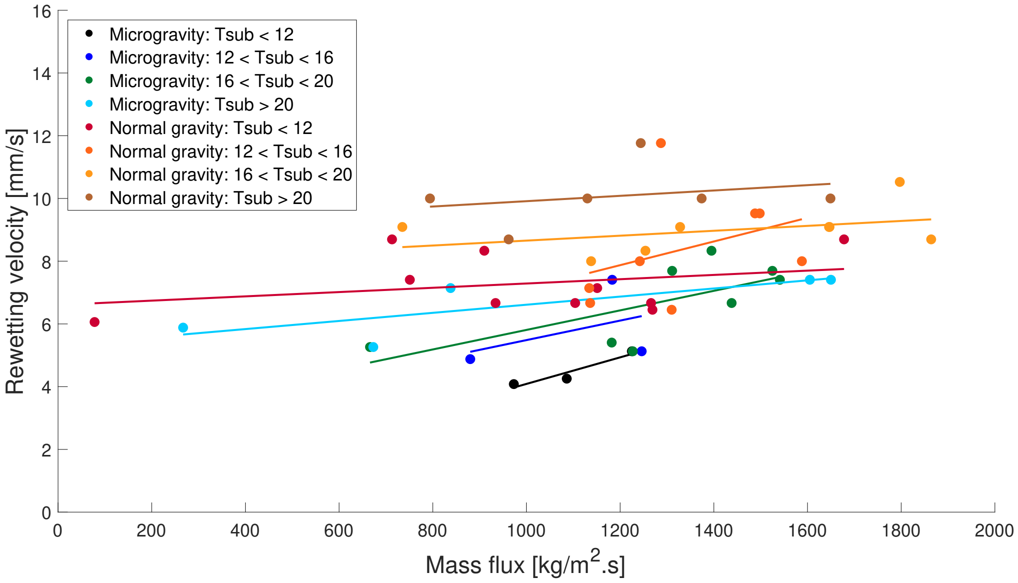

Figure 4.9: Rewetting velocity as a function of the mass flux for different subcooling ranges.

4.3 Modelling of the boiling curve

4.3.1 Film boiling

Since film boiling is the regime that takes more time to complete, it is the one that influences the most the total time of the quenching process. Therefore, an accurate prediction of this regime would come a long way in the correct modelling of the boiling curve. Figure 4.10 shows the results obtained with several correlations, for both terrestrial and microgravity conditions. All the correlations used depend on the gravity level, which is essential in our study.

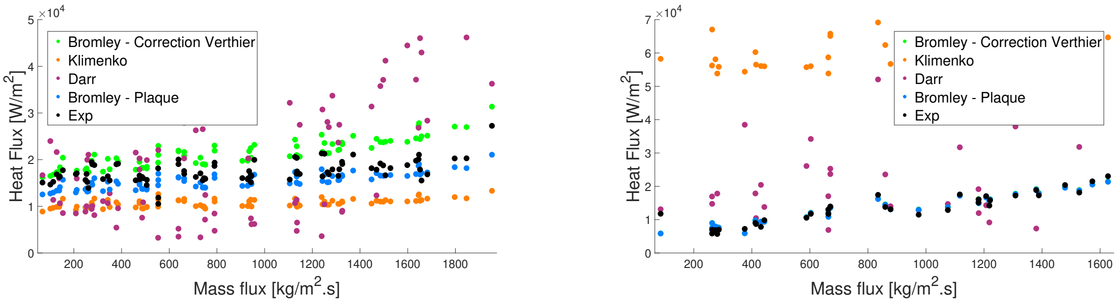

(a) Normal gravity

(b) Microgravity

Figure 4.10: Comparison of the different correlations for the film boiling regime.

In normal gravity, it is possible to observe that the Bromley - Plaque presents the results closer to the experimental data. In general, the Bromley correlation with the correction made by Brian Verthier [16] overestimates the heat flux. Although it is very close to the experimental data for trials with low mass fluxes, the error increases for the higher values of mass flux. On the contrary, the Klimenko correlation tends to underestimate the heat flux. Finally, the Darr's correlation presents very dispersed results and the reason for that is thought to be the use of the equilibrium quality value to calculate the heat flux. In fact, Brian Verthier has calculated the values of the equilibrium quality in its work but they have a significant incertitude (around 35%), which is a problem because the second term of the Darr's correlation, where the equilibrium quality intervenes, is also by far the term that contributes the most for the total heat transfer coefficient.

For microgravity conditions, the correlation from Klimenko is the one that presents a bigger deviation for the experimental data, overestimating the heat flux by around 200%. Furthermore, the Darr's correlation continues to present dispersed values around the experimental data for the reasons previously explained. Finally, both correlations based in the Bromley's model present results very close to the experimental ones. So close that the green dots from the Bromley - Verthier correlation cannot be seen due to being superposed by the experimental and Bromley - Plate results.

In the figure 4.11 below, it is possible to see the comparison of the experimental results and the ones predicted both by Bromley's law for the flow around the cylinders with the correction by Brian Verthier (Bromley-Verthier), and by the ones predicted using the formula of Bromley's model for a plane plate (Bromley-plaque) using Lref = 0.036 m.

For terrestrial conditions, Bromley-Verthier tends to underestimate the heat flux for low mass fluxes and to overestimate the heat flux for higher mass fluxes. Nevertheless, in most cases this correlation allows to obtain results with a deviation of less than 30% from the experimental results, except for the range of very low mass fluxes where the error increases. On the contrary, Bromley-plaque underestimates the heat flux for whole range of mass flux, with an almost constant deviation of around 10%. Since the deviation is practically constant, it is possible to conclude that this formula predicts with accuracy the evolution of the heat flux as a function of the mass flux.

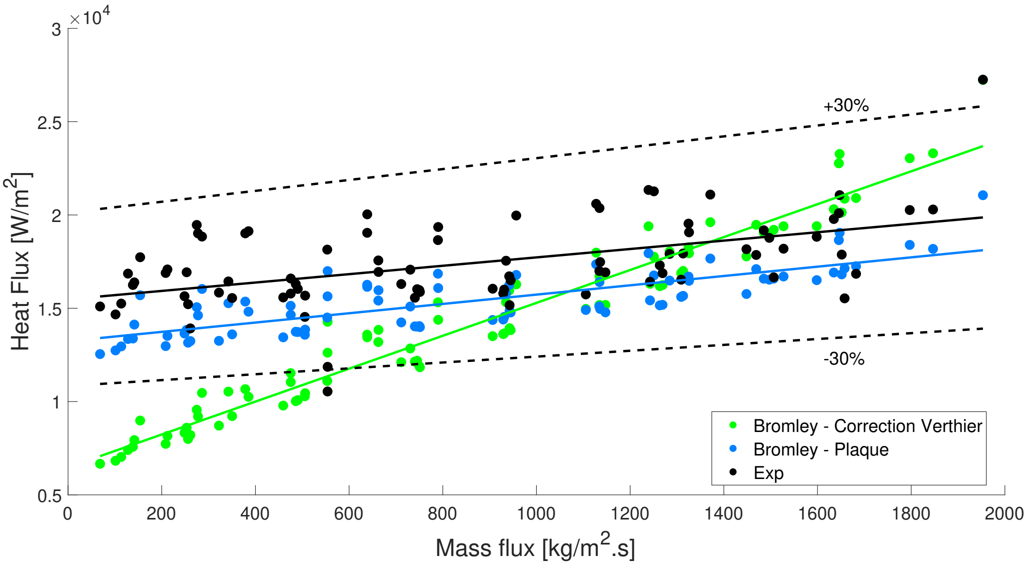

Figure 4.11: Heat flux as a function of mass flux for a superheat = 90ºC, in normal gravity conditions.

In weightlessness conditions both formulas improve their accuracy, as it can be seen in figure 4.12. While Bromley-Verthier overestimates the heat flux for low mass fluxes, it predicts with significant precision the heat flux for higher mass fluxes. Bromley-plaque also presents a great accuracy. In fact, the best-fit line obtained via the least-squares method of the results predicted by this formula and the best-fine line of the experimental results are virtually indistinguishable. In this case, the using Lref value used was 0.012 m.

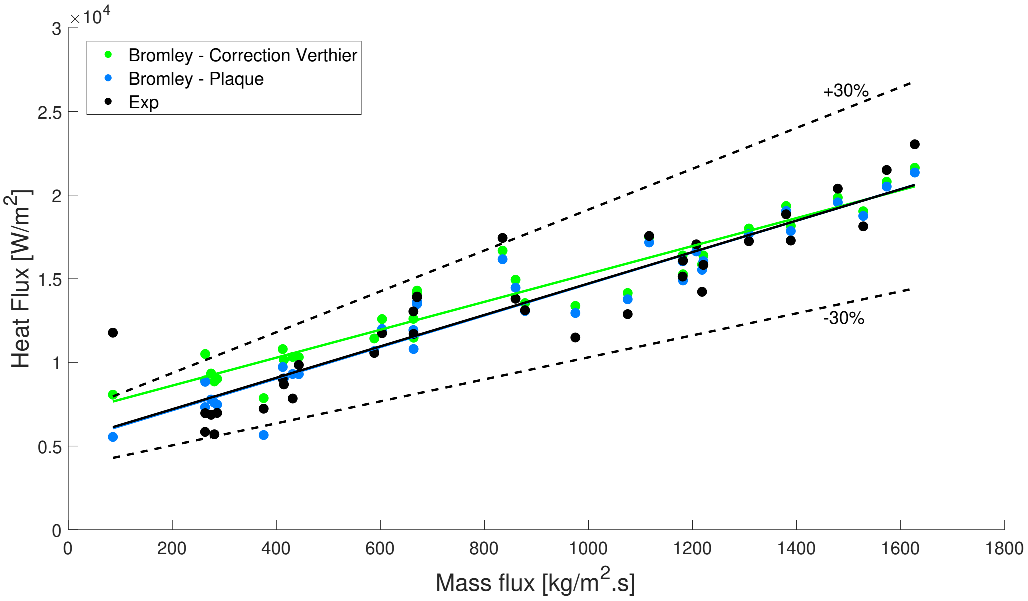

Figure 4.12: Heat flux as a function of mass flux for a superheat = 90ºC, in microgravity conditions.

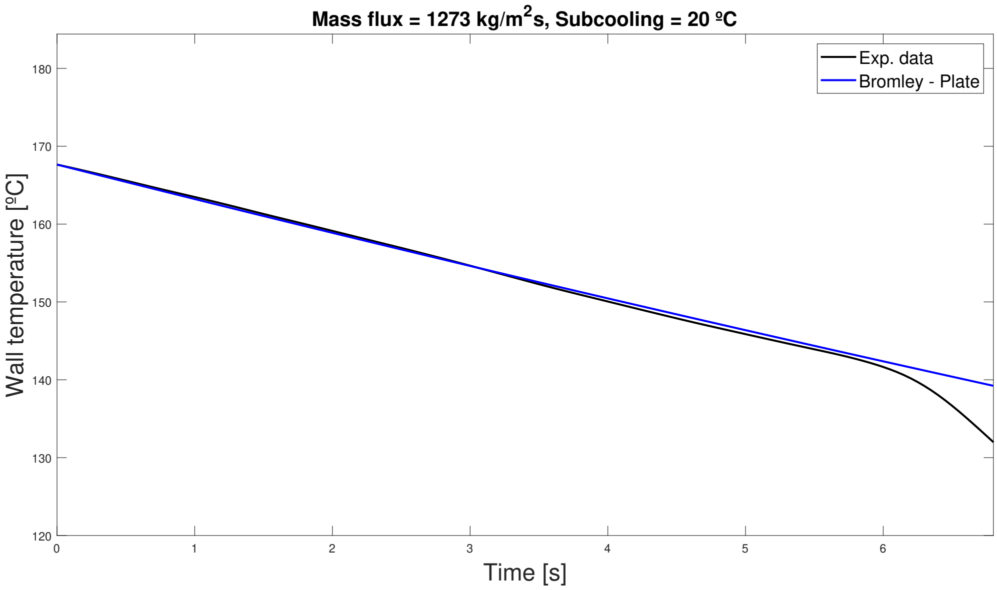

Figure 4.13: Comparison of the predicted evolution of temperature as a function of time with the experimental result, for the HFE7100 case in microgravity conditions.

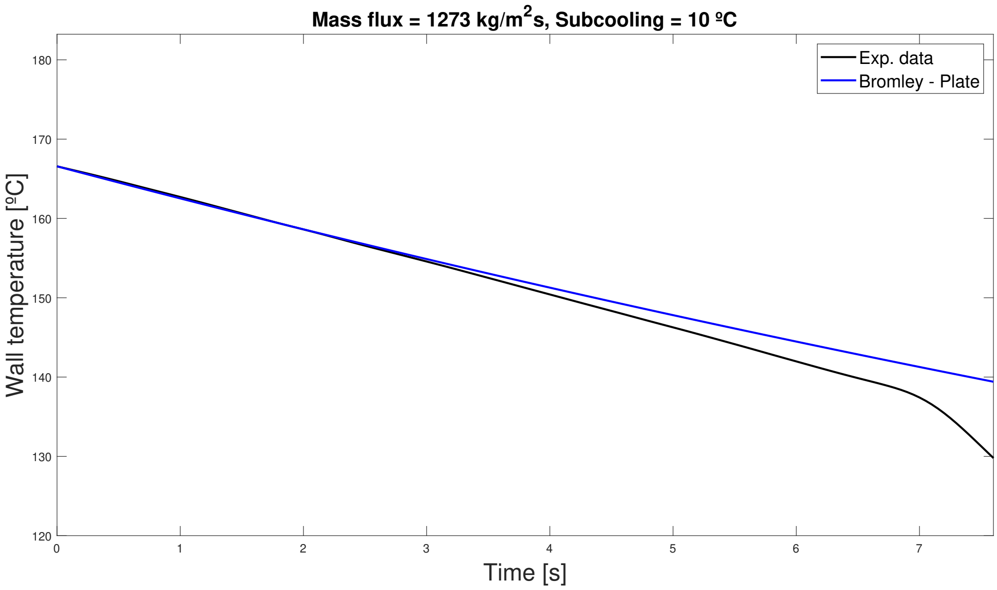

Figure 4.14: Comparison of the predicted evolution of temperature as a function of time with the experimental result, for the HFE7100 case in normal gravity conditions.

Validation of the reference length

In order to assess if the values of L_{ref} were in agreement with the physical explanation given in 2.2.1, the rewetting velocity was multiplied by the time difference (Δt) between a superheat of 90ºC or 80ºC and the rewetting point. This was done both in normal gravity and microgravity conditions, and the results are presented in figure 4.16. Firstly, it is possible to observe that the order of magnitude of L_{ref} is correct. Secondly, the data for a superheat of 90 ºC is close to the value of L_{ref} in normal gravity, but in microgravity the value of L_{ref} is between the data for a superheat of 90 ºC and 80 ºC.

By looking at figure 4.15, one can understand that the point of L_{ref} is not always located in the same place in the boiling curve. Sometimes, it is exactly located between the points corresponding to superheats of 90 ºC (red line) and 80 ºC (green line), such as in figure 4.15 (b) and (d). However, for normal gravity conditions it is more common to find L_{ref} located very near the red line, while for microgravity it is closer to the green line. Either way, the values for L_{ref} are coherent with the physical explanation suggested.

Application to cryogenic fluids

Considering the accuracy obtained with the Bromley-plaque formula in predicting the heat flux for our experiments, it was decided to test it against the results of the cryogenic experiment made by Darr et al. [24]. Before presenting the results obtained, a few introductory notes are necessary.

First of all, the data from the experiments in terrestrial conditions was not made available by Darr et al. [24], therefore the Bromley-plaque model was only validated for the microgravity conditions. Secondly, the properties of saturated nitrogen, either in gaseous or liquid state, were obtained in the website [71]. It was not possible to find the source of the information nor its level of accuracy, hence it can be a

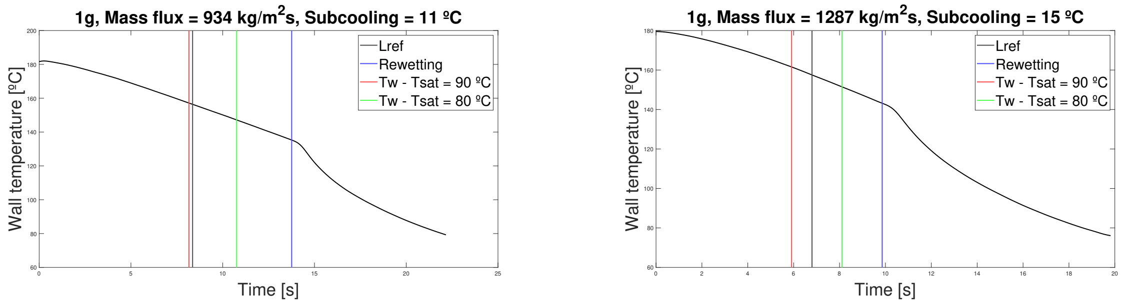

(a) Normal gravity (b) Normal gravity

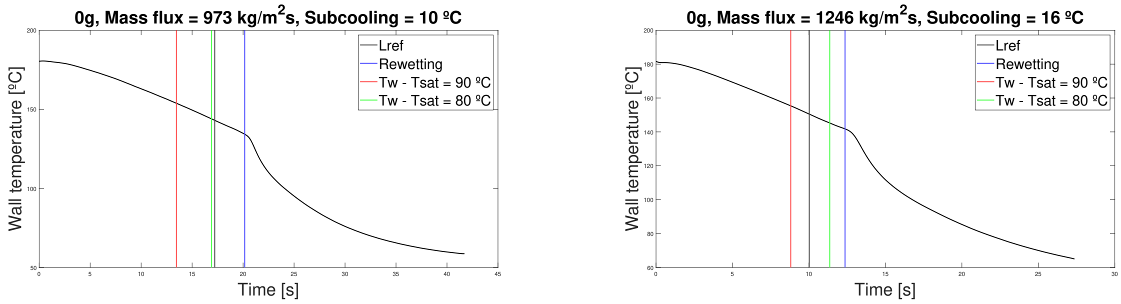

(c) Microgravity (d) Microgravity

Figure 4.15: Comparison of the position of the points with a superheat of 90 and 80 ºC with the position of Lref in the Tw vs time curve.

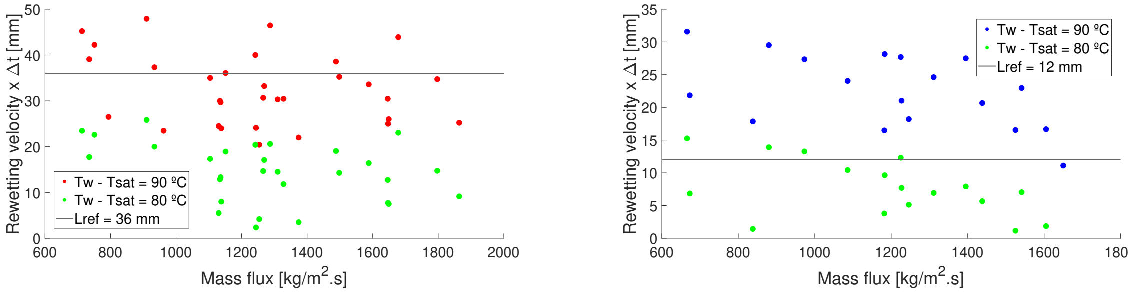

(a) Normal gravity (b) Microgravity

Figure 4.16: Validation of L_{ref} by comparing its value with the rewetting velocity multiplied by the time difference between the rewetting and a characteristic point in the plot of wall temperature with time.

source of error in the heat flux calculation. Furthermore, it was not possible to find the properties of the material of the tube, 304 stainless steel. Therefore the properties used are the ones for the range of 0 to 100ºC, and were obtained in the website [72]. The quantitative impact that this approximation has on the obtained results is unknown. Moreover, only four out of the ten trials available were used because the other six had lower mass fluxes and as result did not arrive near the rewetting point before the end of the microgravity period. Hence, either the validation was made for superheats above 100 K using the other 6 trials, or for lower superheats using this 4 trials. It was not possible to do the validation using higher superheats using all the trials because these 4 that were selected were in transitory conditions for those values of superheat. Finally, the Lref value used is exactly the same that was used for the HFE7100 experiments, i.e. no modifications were made in the formula to account for cryogenic fluids.

The comparison between the results obtained and the experimental data can be seen in figure 4.17, along with best-fit lines for both sets of data. The results are presented for six values of superheat, ranging from 65 to 8 K, in order to assess the accuracy of the Bromley-plaque correlation in a substantial part of the film boiling regime. The graphs show that, in general, the correlation overestimates the heat flux for superheats below or equal to 75 K, and underestimates it for superheats higher than 75 K, with the best agreement between experimental data and predicted results obtained for a superheat equal to 85 K. Having said that, the estimation error is inferior to 30% for all cases and for the entire range of mass flux. In the chapter A.3 of the Appendix, the curves for the other 3 cases studied are available.

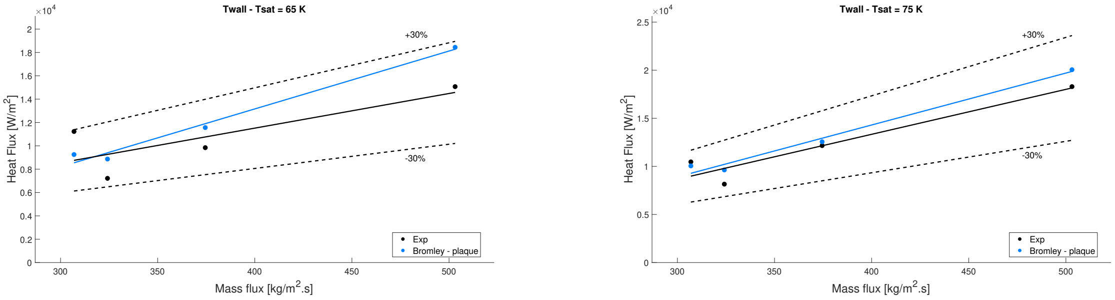

(a) Normal gravity (b) Microgravity

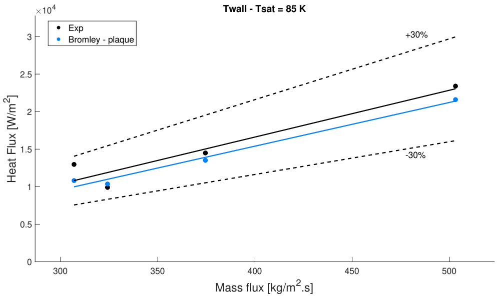

(c) Microgravity

Figure 4.17: Comparison of the theoretical model with the cryogenic experimental results for different superheats.

Considering this results, the question arose as to whether the model was capable of predicting the evolution of the wall's temperature as a function of time, which implicates an accurate prediction of the heat flux throughout the whole film boiling regime. Figure A.13 shows the evolution of the wall's temperature for the case with the higher mass flux and, after an initial transitory regime that last around 2 3 seconds, there are 5 seconds during which the slope is approximately constant. This is our region of interest since it represents the film boiling regime, and it can be seen that the Bromley-plaque model predicts the evolution of the temperature with accuracy. In fact, those 5 seconds, the wall temperature decreases more than 40 K, and at the rewetting point there is only a difference of 1.5 K between the predicted temperature and the experimental data. Nevertheless, the prediction is not perfect since the slope of the predicted curve is less pronounced than the experimental one for higher temperatures, then the two curves intersect and for nearer the rewetting point the slop of the predicted curve is steeper than the experimental one. This is in accordance with what has been observed from figure 4.17.

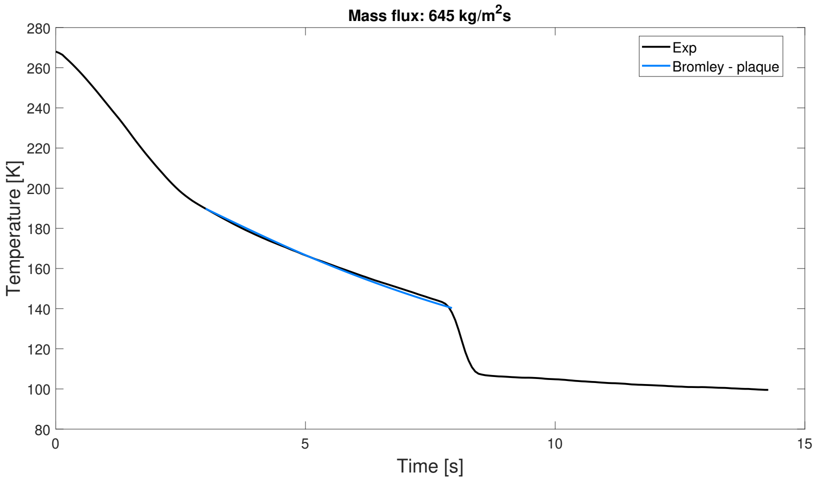

Figure 4.18: Comparison of the predicted evolution of temperature as a function of time with the experimental result, for the LN2 case.

4.3.2 Rewetting temperature

The figure 4.19 shows the comparison of the several models/correlations to calculate the rewetting temperature with the experimental data obtained, both in normal gravity and in microgravity.

Some of the previously correlations mentioned in the chapter 2.2.2 have not been plotted because they either overestimate or underestimate significantly the rewetting temperature values. Looking at the figure 4.19, one can observe that the Spielberg's correlation and the correlations that derive from it (Semeria, Baumeister, Darr) constitute the upper and lower boundaries . One evident problem of these 4 correlations that have the same origin is the incapability of reproducing the dependency of the Leidenfrost temperature with the flow mass flux.

On the other hand, the Berenson's law and two other that derive from it (Henry and Henry modified) predict mostly well the increasing trend of rewetting temperature with the flow mass flux. One important thing about this correlations is the fact that, despite the dependency of the Berenson's law on the gravity acceleration, g, this value is kept equal to 9,81 m/s^2 even for the trials under microgravity conditions, otherwise the results would overestimate the Leidenfrost temperature by a great margin. In terms of results, the Berenson and the Henry laws subestimate the results for the lower mass fluxes, but give good results for higher mass fluxes. Furthermore, the modification of the Henry law made by Brian Verthier gives good results in the entire range of mass fluxes, which comes as no surprise given that the correction made was precisely to fit our experimental data.

We can conclude from this that the models based on assumption of the hydrodynamic instability of the liquid-vapour interface as the main factor triggering the rewetting process are more accurate than the models using the metastable liquid instability hypothesis.

4.3.3 Critical Heat Flux

As it can be seen in figure 4.20, none of the correlations presented in 2.2.3 predicts accurately the CHF in either gravity levels. In fact, all the correlations overestimate the CHF except for the Kutateladze

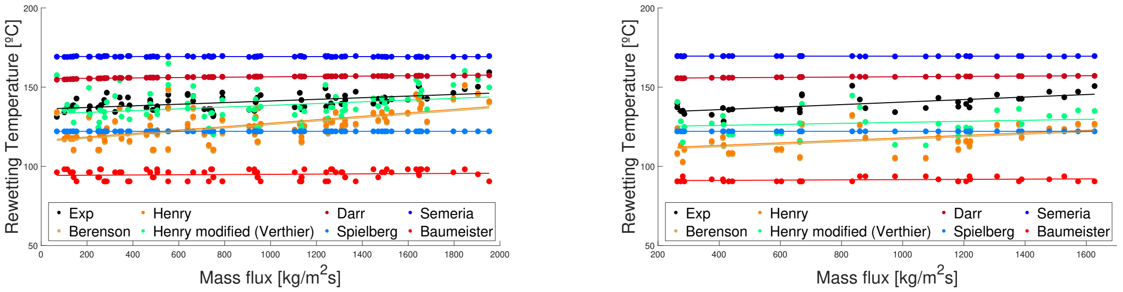

(a) Normal gravity (b) Microgravity

Figure 4.19: Comparison of the several models/correlations to calculate the rewetting temperature with the experimental data.

correlation in microgravity, which underestimates it.

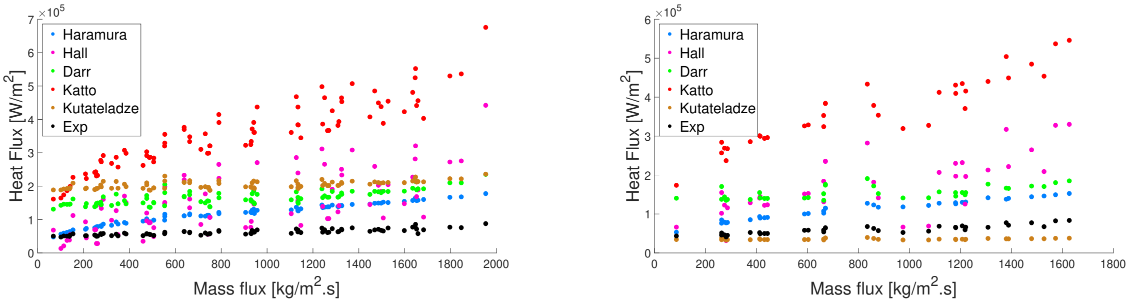

(a) Normal gravity (b) Microgravity

Figure 4.20: Comparison of the several models/correlations for the critical heat flux with the experimental data.

As previously discussed, the instationarity can play an important role in the CHF. In other words, the fact that the wall temperature is decreasing rapidly decreases the CHF. This was reported by Auracher and Marquardt [48], whose results were obtained with the refrigerant FC72 and are presented in figure 2.4 in the chapter 2.2.3. The plot shows that for a wall cooling velocity of around 7ºC/s, the CHF decreased more than 25%. In our case, the wall cooling velocity is in the range of 10-15 ºC/s depending on the flow mass flux and subcooling, as it can be seen in figure 4.21.

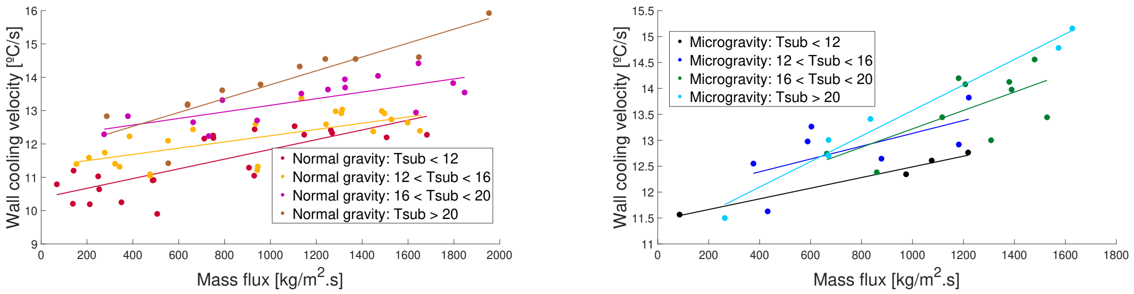

(a) Normal gravity (b) Microgravity

Figure 4.21: Impact of flow mass flux and subcooling in the cooling velocity of the wall.

As a result, Brian Verthier [16] proposed the correction presented in equation 4.1 in an effort to adapt the correlations developed for the pool boiling case to the transient regime. The instationarity is taken into account by the term $\partial T_w/\partial t$ at the critical heat flux point, which is calculated using equation 4.2. This correction was applied to the correlations tested and the results obtained were more accurate, as expected. The plot of these results is presented in A. It was found that the best correlation was the one from Haramura, which still overestimates the CHF but the error is always inferior to 30% in both gravity levels and for the entire range of mass flux, as it can be seen in figure 4.22.

$$\frac{q_{CHF,inst.}}{q_{CHF,steady}} = 0.0014\left(\frac{\partial T_w}{\partial t}\right)^2_{CHF} + 0.064\left(\frac{\partial T_w}{\partial t}\right)_{CHF} + 1 \tag{4.1}$$

$$\left(\frac{\partial T_w}{\partial t}\right)_{CHF} = -1.65\sqrt{\frac{\lambda\rho Cp|_l}{\lambda\rho Cp|_w}}^{-0.2167} Re_l^{0.266} Ja_{sub}^{0.213} \tag{4.2}$$

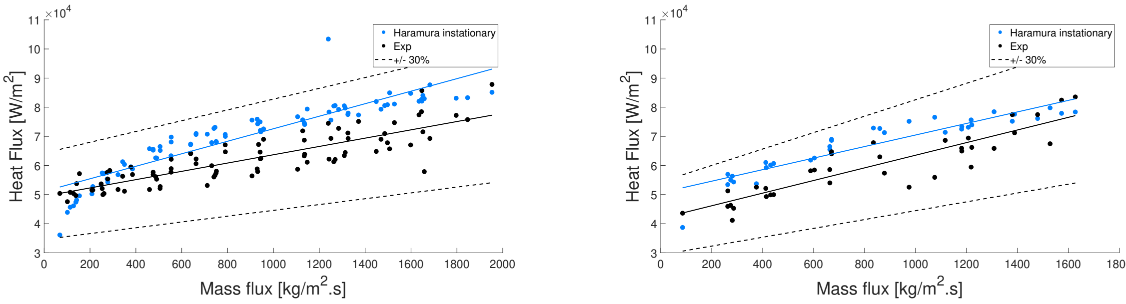

(a) Normal gravity

(b) Microgravity

Figure 4.22: Comparison between the experimental results and the results obtained with the Haramura correlation multiplied by the instationarity correction.

4.3.4 Nucleate boiling

The figure 4.23 shows the comparison of the several models/correlations to calculate the heat flux in the nucleate boiling regime with the experimental data obtained, both in normal gravity and in microgravity.

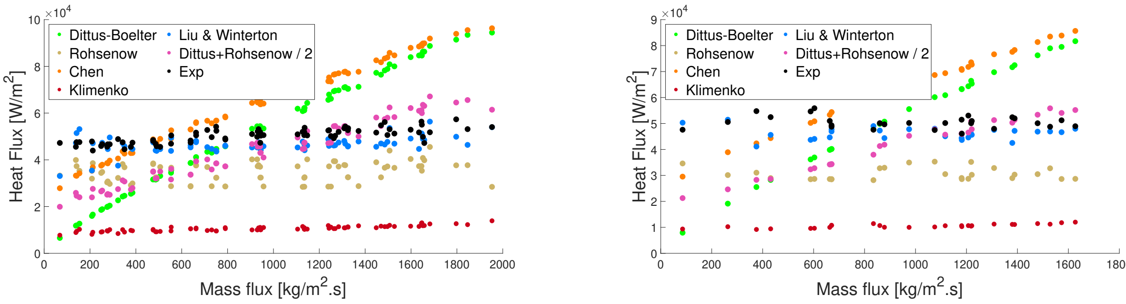

(a) Normal gravity

(b) Microgravity

Figure 4.23: Comparison of the several models/correlations for the nucleate boiling regime with the experimental data.

First of all, the accuracy of the various correlations seems the same in both gravity levels. Secondly, it was found that the classical solution of using the Dittus-Boelter correlation along with the Rohsenow correlation to account for the forced convection and nucleate boiling, respectively, significantly overestimates the heat flux. Similarly to what happens for the CHF, the instationarity plays an important role and it was reported a decrease of around 35% of the heat flux the nucleate boiling regime in the case where the wall cooling velocity was approximately 7 ºC/s. Considering that in our case the wall cooling velocity is in the range of 10-15 ºC/s (4.21), the decrease in the CHF is expected to be even higher. The Chen correlation also overestimated the heat flux for the majority of mass flux range, and the correlation for Klimenko underestimated significantly the heat flux.

Having said that, the correlation from Liu & Winterton predicts accurately the heat flux in the nucleate boiling regime for the whole range of mass flux and in both gravity levels. Moreover, one of the particularities of the nucleate boiling regime is the large variation of the heat flux with the wall superheat. Hence, to verify if the correlation from Liu & Winterton predicted accurately the heat flux for the entire nucleate boiling regime, the predicted boiling curve was compared with the experimental one, as it can be seen in figure 4.24. The correlation predicts the heat flux with an error inferior to 30% for an interval of wall superheat ranging from 30 to 65ºC. More plots like this one are presented in A for both gravity levels and different values of mass flux.

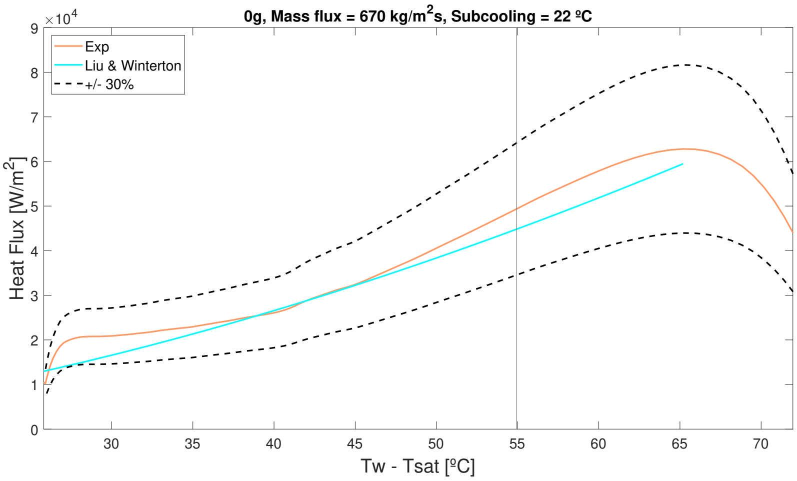

Figure 4.24: Comparison of the predicted boiling curve with the experimental result, for the nucleate boiling regime.

Chapter 5

Conclusions

The objective of this internship was to study the modelling of the different boiling regimes during the chill down of rocket engines by cryogenic fluid in microgravity. In particular, special focus was given to the theoretical modelling of the film boiling regime, since it is the regime that impacts the most the duration of the chilling process. Hence, a theoretical model coupled with the heat transfers in the tube wall was developed and validated using the data obtained in the scope of the PhD thesis of Brian Verthier [16], who designed and built at IMFT an experiment to study the quenching of a stainless steel tube by HFE7100. Furthermore, the proposed model was also validated for cryogenic fluids, using the LN2 data from Darr et al. [25]. For both type of fluids, the correlation is able to predict the heat flux within an error margin always inferior to 30%.

In terms of qualitative results, it is possible to conclude that the increase of flow mass flux and subcooling lead to an increase in the heat flux in all the regimes except for the nucleate boiling regime, where this is not verified under microgravity conditions due to the dominance of the nucleate boiling mechanism over the forced convection. In terms of gravity levels, a significant decrease of the heat flux in the film boiling regime was found, especially for lower mass fluxes. For higher mass fluxes, the difference in the heat flux gradually decreases. Moreover, the rewetting velocity is reduced to almost half under microgravity conditions. In the other regimes, the influence of gravity is not well-defined.

From the bibliographic review made, we can conclude that our findings are in agreement with the majority of the results reported. However, considering that some articles report results contrary to what we found, namely regarding the rewetting velocity, in the future it would be advisable to conduct more experiments to increase the data set and consolidate the results obtained in the chill down process under microgravity conditions.

Bibliography

[1] European Space Agency (ESA). Ariane 5 es. `https://www.esa.int/Enabling_Support/Space_Transportation/Launch_vehicles/Ariane_5_ES`.

[2] Arianespace (ArianeGroup). Ariane 6. https://www.arianespace.com/vehicle/ariane-6/.

[3] Toru Tanabe, Sinichi Nakasuka, and Takanori Iwata. System and operation analyses of OTV Network - A new space transportation concept. In *15th International Symposium on Space Technology and Science*, volume 2, pages 1475–1480, January 1986.

[4] European Space Agency (ESA). Microgravity and drop towers. `www.esa.int/Education/Microgravity_and_drop_towers`.

[5] B. N. Antar, F. G. Collins, and A. Hedayatpour. Transfer line chilldown in low gravity environment. *26th Joint Propulsion Conference*, 1990. doi.org/10.2514/6.1990-2372.

[6] Kanishkan Sathasivam. Cryogenic line quench experiment in microgravity. Master's thesis, University of Tennessee, 1991.

[7] Masaki Misawa. *An Experimental and Analytical Investigation of Flow Boiling Heat Transfer under Microgravity Conditions*. PhD thesis, University of Florida, 1993.

[8] K. Adham-Khodaparast, J. J. Xu, and M. Kawaji. Flow film boiling collapse and surface rewetting in normal and reduced gravity conditions. *International Journal of Heat and Mass Transfer*, 38(15), 1995. doi.org/10.1016/0017-9310(95)00026-6.

[9] C. J. Westbye, M. Kawaji, and B. N. Antar. Boiling heat transfer in the quenching of a hot tube under microgravity. *Journal of Thermophysics and Heat Transfer*, 9(2), 1995. doi.org/10.2514/3.660.

[10] Jason Jianxin Xu. *Flow boiling heat transfer in the quenching of a hot surface under reduced gravity conditions*. PhD thesis, University of Toronto, 1998.

[11] Osamu Kawanami, Hisao Azuma, and Haruhiko Ohta. Effect of gravity on cryogenic boiling heat transfer during tube quenching. *International Journal of Heat and Mass Transfer*, 50(17-18), 2007. doi.org/10.1016/j.ijheatmasstransfer.2007.01.025.

[12] Kun Yuan, Yan Ji, J . N. Chung, and Wei Shyy. Cryogenic boiling and two-phase flow during pipe chilldown in earth and reduced gravity. *Journal of Low Temperature Physics*, 150(101-122), 2008. DOI 10.1007/s10909-007-9521-8.

[13] G. P. Celata, M. Cumo, M. Gervasi, and G. Zummo. Quenching experiments inside 6.0 mm tube at reduced gravity. *International Journal of Heat and Mass Transfer*, 52(11-12), 2009. doi.org/10.1016/j.ijheatmasstransfer.2008.08.043.

[14] S. R. Darr, Hong Hu, N. G. Glikin, J.W. Hartwig, A. K. Majumdar, A. C. Leclair, and J. N. Chung. An experimental study on terrestrial cryogenic transfer line chilldown i. effect of mass flux, equilibrium quality, and inlet subcooling. *International Journal of Heat and Mass Transfer*, 103:1225–1242, 2016. doi.org/10.1016/j.ijheatmasstransfer.2016.05.019.

[15] Kiyoshi Kinefuchi, Wataru Sarae, Yutaka Umemura, Takeshi Fujita, and Koichi Okita. Investigation of cryogenic chilldown in a complex channel under low gravity using a sounding rocket. *Journal of Spacecraft and Rockets*, 56(1), 2019. DOI: 10.2514/1.A34222.

[16] Brian Verthier. *Une étude sur les transferts associés aux écoulements diphasiaues de fluides cryogéniques en microgravité : application à la mise en froid de moteurs-fusée*. PhD thesis, Institut National Polytechnique de Toulouse, 2010.

[17] Shiro Nukiyama. Maximum and minimum values of heat transmitted from metal to boiling water under atmospheric pressure. *Journal of the Japanese Society of Mechanical Engineers.*, 37:367, 1934.

[18] W. Nusselt. Die oberflachenkondensation des wasserdamphes. *Zeitschrift des Vereins Deutscher Ingenieure.*, 60:541–546,569–575, 1916.

[19] Van P. Carey. *Liquid-Vapor Phase-Change Phenomena: An Introduction to the Thermophysics of Vaporization and Condensation Processes in Heat Transfer Equipment*. CRC Press, 3rd edition, 2020.

[20] Leroy A. Bromley. Heat transfer in stable film boiling. *Chemical Engineering Progress.*, 46:211–227, 1950.

[21] V. V. Klimenko. Film boiling on a horizontal plate - new correlation. *International Journal of Heat Transfer*, 24(1):69–79, 1981. doi.org/10.1016/0017-9310(81)90094-6.

[22] J. M. Ramilison and J. H. Lienhard. Transition boiling heat transfer and the film transition regime. *Journal of Heat Transfer*, 109(3):746–752, 1987. doi.org/10.1115/1.3248153.

[23] Leroy A. Bromley, Norman R. Leroy, and James A. Robbers. Heat transfer in forced convection film boiling. *Industrial and Engineering Chemistry.*, 45(12):2639–2646, 1953.

[24] Samuel Darr, Jun Dong, Neil Glikin, Jason Hartwig, Alok Majumdar, Andre Leclair, and Jacob Chung. The effect of reduced gravity on cryogenic nitrogen boiling and pipe chilldown. *npj Microgravity*, 2(16033), 2016. https://doi.org/10.1038/npjmgrav.2016.33.

[25] S. R. Darr, J. W. Hartwig, J. Dong, H. Wang, A. K. Majumdar, A. C. LeClair, and J. N. Chung. Two-phase pipe quenching correlations for liquid nitrogen and liquid hydrogen. *Journal of Heat Transfer*, 141(4): 042901, April 2019. doi.org/10.1115/1.4041830.

[26] J. D. Bernardin and I. Mudawar. The leidenfrost point: Experimental study and assessment of existing models. *Journal of Heat Transfer*, 121(4), 1999. doi.org/10.1115/1.2826080.

[27] Geoffrey Ingram Taylor. The instability of liquid surfaces when accelerated in a direction perpendicular to their planes. i. volume A 201, pages 192–196. Royal Society of London, 1950.

[28] P. J. Berenson. Film-boiling heat transfer from a horizontal surface. *Journal of Heat Transfer*, 83(3):351–356, 1961. doi.org/10.1115/1.3682280.

[29] R. E. Henry. A correlation for the minimum film boiling temperature. volume 70 of *Chemical engineering progress symposium series*, pages 81–90. American Institute of Chemical Engineers, 1974.

[30] Shi-Chune Yao and R. E. Henry. An investigation of the minimum film boiling temperature on horizontal surfaces. *Journal of Heat Transfer*, 100(2):260–267, 1978. doi.org/10.1115/1.3450793.

[31] Akira Sakurai, Masahiro Shiotsu, and Koichi Hata. Steady and unsteady film boiling heat transfer at subatmospheric and elevated pressures. Advanced Course in Heat Transfer in Nuclear Reactor Safety, pages 301–312, 1982.

[32] J. G. Eberhart and H. C. Schnyders. Application of the mechanical stability condition to the prediction of the limit of superheat for normal alkanes, ether, and water. *The Journal of Physical Chemistry*, 77(23):2730–2736, November 1973. doi.org/10.1021/j100641a004.

[33] Van P. Carey. *Liquid-Vapor Phase-Change Phenomena: An Introduction to the Thermophysics of Vaporization and Condensation Processes in Heat Transfer Equipment*. Taylor & Francis, 1st edition, 1992.

[34] P. Spiegler, J. Hopenfeld, M. Silberberg, C. F. Bumpus, and A. Norman. Onset of stable film boiling and the foam limit. *International Journal of Heat and Mass Transfer*, 6(11):987–989, 1963. doi.org/10.1016/0017-9310(63)90053-X.

[35] R. Semeria. Thermique des fluides diphasiques bouillants. *Rev. gen. Therm.*, 12(135):211–218, 1973.

[36] K. J. Baumeister and F. F. Simon. Leidenfrost temperature—its correlation for liquid metals, cryogens, hydrocarbons, and water. *Journal of Heat Transfer*, 95(2):166–173, May 1973. doi.org/10.1115/1.3450019.

[37] M. DeSalve and B. Panella. Thermal-hydraulics of the precursory cooling during bottom reflooding. Multi-phase flow and heat transfer symposium-workshop, 1983.

[38] Christopher Konishi and Issam Mudawar. Review of flow boiling and critical heat flux in microgravity. *International Journal of Heat and Mass Transfer*, 80:469–493, 2015. doi.org/10.1016/j.ijheatmasstransfer.2014.09.017.

[39] Moritz Bruder, Gregor Bloch, and Thomas Sattelmayer. Critical heat flux in flow boiling—review of the current understanding and experimental approaches. *Heat Transfer Engineering*, 38(3):347–360, 2017. doi.org/10.1080/01457632.2016.1189274.

[40] S. S. Kutateladze. On the transition to film boiling under natural convection. *Kotloturbostroenie.*, 1948.

[41] S. S. Kutateladze. *Heat Transfer in Condensation and Boiling*. Leningrad Division of State Publishing House of Machine Literature, second edition, 1952.

[42] Y. Haramura and Y. Katto. A new hydrodynamic model of critical heat flux, applicable widely to both pool and forced convection boiling on submerged bodies in saturated liquids. *International Journal of Heat and Mass Transfer.*, 26(3):389–399, 1983. doi.org/10.1016/0017-9310(83)90043-1.

[43] Y. Katto and H. Ohno. An improved version of the generalized correlation of critical heat flux for the forced convective boiling in uniformly heated vertical tubes. *International Journal of Heat and Mass Transfer.*, 27(9):1641–1648, 1984. doi.org/10.1016/0017-9310(84)90276-X.

[44] M. Mohammed Shah. Improved general correlation for critical heat flux during upflow in uniformly heated vertical tubes. *International Journal of Heat and Fluid Flow.*, 8(4):326–335, 1987. doi.org/10.1016/0142-727X(87)90069-5.

[45] David D. Hall and Issam Mudawar. Critical heat flux (chf) for water flow in tubes—ii.: Subcooled chf correlations. *International Journal of Heat and Mass Transfer.*, 43(14):2605–2640, 2000. doi.org/10.1016/S0017-9310(99)00192-1.

[46] Y. Katto and C. Kurata. Critical heat flux of saturated convective boiling on uniformly heated plates in a parallel flow. *International Journal of Multiphase Flow.*, 6(6):575–582, 1980. doi.org/10.1016/0301-9322(80)90052-X.

[47] Cho-Ning Huang and Chirag R. Kharangate. A new mechanistic model for predicting flow boiling critical heat flux based on hydrodynamic instabilities. *International Journal of Heat and Mass Transfer*, 138:1295–1309, 2019. doi.org/10.1016/j.ijheatmasstransfer.2019.04.103.

[48] Hein Auracher and Wolfgang Marquardt. Experimental studies of boiling mechanisms in all boiling regimes under steady-state and transient conditions. *International Journal of Thermal Sciences.*, 41(7):586–598, 2002. https://doi.org/10.1016/S1290-0729(02)01352-2.

[49] John C. Chen. Correlation for boiling heat transfer to saturated fluids in convective flow. *Industrial Engineering Chemistry Process Design and Development.*, 5(3):322–329, 1966.

[50] F. W. Dittus and L. M. K. Boelter. Heat transfer in automobile radiators of the tubular type. *University of California Publications in Engineering*, 2:443–461, 1930.

[51] Vijay. (Dhir). *Handbook of phase change: boiling and condensation*, chapter 4. Nucleate boiling. Taylor Francis.

[52] H. K. Forster and N. Zuber. Dynamics of vapor bubbles and boiling heat transfer. *American Institute of Chemical Engineers Journal.*, 1(4):531–535, 1955. doi.org/10.1002/aic.690010425.

[53] J. G. (Collier). *Two-Phase Flow and Heat Transfer in the Power and Process Industries*, chapter 8. Hemisphere Publishing.

[54] V. Scheiff, F. Bergame, J. Sebilleau, P. Ruyer, and C. Colin. Experimental study of steady and transient subcooled flow boiling. *International Journal of Heat and Mass Transfer.*, 164, 2021. doi.org/10.1016/j.ijheatmasstransfer.2020.120548.

[55] V. V. Klimenko. Heat transfer in forced convection boiling in a channel. *Heat Transfer - Sovietic Research.*, 17(2):96–100, 1985.

[56] V. V. Klimenko. A generalized correlation for two-phase forced flow heat transfer. *International Journal of Heat and Mass Transfer.*, 31(3):541–552, 1988.

[57] V. V. Klimenko. A generalized correlation for two-phase forced flow heat transfer - second assessment. *International Journal of Heat and Mass Transfer.*, 33(10):2073–2088, 1990.

[58] Z. Liu and R. H. S. Winterton. A general correlation for saturated and subcooled flow boiling in tubes and annuli, based on a nucleate pool boiling equation. *International Journal of Heat and Mass Transfer.*, 34(11):2759–2766, 1991.

[59] M. G. Cooper. Heat flow rates in saturated nucleate pool boiling - a wide-ranging examination using reduced properties. *Advances in Heat Transfer.*, 16:157–239, 1984.

[60] Yiwu Kuang, Fei Han, Lijie Sun, Rui Zhuan, and Wen Wang. Modelling and numerical investigation of hydrogen nucleate flow boiling heat transfer. *International Journal of Hydrogen Energy.*, 46(37):19617–19632, 2021. doi.org/10.1016/j.ijhydene.2021.03.084.

[61] (NASA). Parabolic flight. https://www.nasa.gov/analogs/parabolic-flight.

[62] (Novespace). Zero-g flights: How it works. https://www.airzerog.com/zero-g-flights-how-it-works/.

[63] (3M™). 3m™ novec™ 7100 engineered fluid. Brochure. https://multimedia.3m.com/mws/media/199818O/3m-novec-7100-engineered-fluid.pdf.

[64] P.E. Tuma and L. Tousignant. Experimental study of the decomposition of hfe-7100 vapor in a billet of ti-6al-4v during bakeout at 275℃. 3M internal report, August 2000.

[65] Brian Verthier and Catherine Colin. Heat transfer coefficient and rewetting temperature during the quenching of a tube by hfe7100. 7th International Conference on Multiphase Flow, 2010.

[66] Denis Maillet, Stéphane André, Jean Christophe Batsale, Alain Degiovanni, and Christian Moyne. *Thermal Quadrupoles: Solving the Heat Equation through Integral Transforms*. Wiley, 2000.

[67] M. Gradeck, A. Kouachi, M. Lebouché, F. Volle, D. Maillet, and J. L. Borean. Boiling curves in relation to quenching of a high temperature moving surface with liquid jet impingement. *International Journal of Heat and Mass Transfer.*, 52(5-6):1094–1104, 2009. doi.org/10.1016/j.ijheatmasstransfer.2008.09.015.

[68] M. Ilyas, C. Hale, S. Walker, and G. Hewitt. Rewetting of heated surfaces by intermittently bursting liquid-metal contacts - an experimental study. 7th International Conference on Multiphase Flow, 2010.

[69] Kun Yuan, Yan Ji, and J. N. Chung. Cryogenic chilldown process under low flow rates. *International Journal of Heat and Mass Transfer*, 50(19-20), 2007. doi.org/10.1016/j.ijheatmasstransfer.2007.01.034.

[70] W. J. Chen, Y.Lee, and D. C. Groeneveld. Measurement of boiling curves during rewetting of a hot circular duct. *International Journal of Heat and Mass Transfer*, 22(6), 1979. doi.org/10.1016/0017-9310(79)90039-5.

[71] ”(peace software)”. ”online calculation of thermodynamic properties of nitrogen”. `www.peacesoftware.de/einigewerte/einigewerte_e.html`.

[72] ”MatWeb: Material Property Data”. ”304 stainless steel”. `matweb.com/search/DataSheet.aspx?MatGUID=abc4415b0f8b490387e3c922237098da&ckck=1`.

Appendix A

Appendix

A.1 Bromley model applied to a flat surface

Velocity profile:

$$\frac{u_v}{u_i} = a_0 + a_1 \frac{y}{\delta} + a_2 \frac{y^2}{\delta^2} \tag{A.1}$$

Boundary conditions:

$$u_v|_{y=0} = 0 \Rightarrow \boxed{a_0 = 0} \tag{A.2}$$

$$u_v|_{y=\delta} = u_i \Rightarrow a_1 + a_2 = 1 \tag{A.3}$$

$$\upsilon_v(\frac{\partial^2 u_v}{\partial y^2}) = -\left(\frac{\rho_l}{\rho_v} - 1\right) g \Rightarrow \boxed{a_2 = -\left(\frac{\rho_l}{\rho_v} - 1\right) \frac{g\delta^2}{2\upsilon u_i}} \Rightarrow \boxed{a_1 = 1 + \left(\frac{\rho_l}{\rho_v} - 1\right) \frac{g\delta^2}{2\upsilon_v u_i}} \tag{A.4}$$

Therefore, the velocity profile is given by the following expression:

$$\boxed{u_v = u_i \frac{y}{\delta} + \left(\frac{\rho_l}{\rho_v} - 1\right) \frac{g\delta^2}{2\upsilon_v} \left(\frac{y}{\delta} - \frac{y^2}{\delta^2}\right)} \tag{A.5}$$

Hypothesis: $u_i = u_L$

Average velocity:

$$\begin{aligned}
\overline{u_v} &= \frac{1}{\delta}\int_0^\delta u_v\,dy \\
&= \frac{1}{\delta}\int_0^\delta u_L\frac{y}{\delta}\,dy + \frac{1}{\delta}\int_0^\delta \left(\frac{\rho_l}{\rho_v}-1\right)\frac{g\delta^2}{2\upsilon_v}\left(\frac{y}{\delta}-\frac{y^2}{\delta^2}\right)dy \\
&= \frac{u_L}{\delta^2}\left[\frac{y^2}{2}\right]_0^\delta + \left(\frac{\rho_l}{\rho_v}-1\right)\frac{g\delta}{2\upsilon_v}\left[\frac{y^2}{2\delta}-\frac{y^3}{3\delta^2}\right]_0^\delta \\
&= \frac{u_L}{2} + \left(\frac{\rho_l}{\rho_v}-1\right)\frac{g\delta}{2\upsilon_v}\left(\frac{\delta}{2}-\frac{\delta}{3}\right) \\
\Rightarrow \overline{u_v} &= \frac{u_L}{2} + \left(\frac{\rho_l}{\rho_v}-1\right)\frac{g\delta^2}{12\upsilon_v}
\end{aligned} \tag{A.6}$$

Mass flux:

$$\begin{aligned}
\dot{m} &= \rho_v\overline{u_v}b\delta \\
\dot{m} &= \frac{\rho_v b u_L\delta}{2} + (\rho_l-\rho_v)\frac{bg\delta^3}{12\upsilon_v}
\end{aligned} \tag{A.7}$$

Temperature profile :

$$T = T_p + (T_{sat}-T_p)\frac{y}{\delta} \tag{A.8}$$

Enthalpy balance:

$$dq = h\Delta T dA = \frac{\lambda_v}{\delta}\Delta T b dx = d\dot{m}h_{lv}^* \Leftrightarrow \delta = \frac{\lambda_v b\Delta T}{h_{lv}^*\left(\frac{d\dot{m}}{dx}\right)} \tag{A.9}$$

Therefore, we obtain:

$$\begin{aligned}
\dot{m} &= \frac{\rho_v b u_L}{2}\frac{\lambda_v b\Delta T}{h_{lv}^*\left(\frac{d\dot{m}}{dx}\right)} + \frac{(\rho_l-\rho_v)\,bg}{12\upsilon_v}\left[\frac{\lambda_v b\Delta T}{h_{lv}^*\left(\frac{d\dot{m}}{dx}\right)}\right]^3 \Leftrightarrow \\
\Leftrightarrow \dot{m}\left(\frac{d\dot{m}}{dx}\right)^3 &= \frac{(\rho_l-\rho_v)\,bg}{12\upsilon_v}\left(\frac{\lambda_v b\Delta T}{h_{lv}^*}\right)^3 + \frac{\rho_v b u_L}{2}\frac{\lambda_v b\Delta T}{h_{lv}^*}\left(\frac{d\dot{m}}{dx}\right)^2
\end{aligned} \tag{A.10}$$

Hypothesis:

$$\frac{d\dot{m}}{dx} \approx \frac{\dot{M}_{ref}}{L_{ref}}$$

where:

$$\dot{M}_{ref} = \frac{h\Delta T b L_{ref}}{h_{lv}^*}$$

Substituting these expressions in equation A.10, we obtain:

$$\begin{aligned}
\dot{m}\left(\frac{d\dot{m}}{dx}\right)^3 &= \frac{(\rho_l-\rho_v)\,bg}{12\upsilon_v}\left(\frac{\lambda_v b\Delta T}{h^*_{lv}}\right)^3+\frac{\rho_v b u_L}{2}\frac{\lambda_v b\Delta T}{h^*_{lv}}\left(\frac{\dot{M}_{ref}}{L_{ref}}\right)^2 \Leftrightarrow \\
\Leftrightarrow \dot{m}^{1/3}\left(\frac{d\dot{m}}{dx}\right) &= \left[\frac{(\rho_l-\rho_v)\,bg}{12\upsilon_v}\left(\frac{\lambda_v b\Delta T}{h^*_{lv}}\right)^3+\frac{\rho_v b u_L}{2}\frac{\lambda_v b\Delta T}{h^*_{lv}}\left(\frac{\dot{M}_{ref}}{L_{ref}}\right)^2\right]^{1/3} \Leftrightarrow \\
\Leftrightarrow \dot{m}^{1/3}\cdot d\dot{m} &= \left[\frac{(\rho_l-\rho_v)\,bg}{12\upsilon_v}\left(\frac{\lambda_v b\Delta T}{h^*_{lv}}\right)^3+\frac{\rho_v b u_L}{2}\frac{\lambda_v b\Delta T}{h^*_{lv}}\left(\frac{\dot{M}_{ref}}{L_{ref}}\right)^2\right]^{1/3}\cdot dx \Leftrightarrow \\
\Rightarrow \int_0^{\dot{M}_{ref}}\dot{m}^{1/3}\,d\dot{m} &= \int_0^{L_{ref}}\left[\frac{(\rho_l-\rho_v)\,bg}{12\upsilon_v}\left(\frac{\lambda_v b\Delta T}{h^*_{lv}}\right)^3+\frac{\rho_v b u_L}{2}\frac{\lambda_v b\Delta T}{h^*_{lv}}\left(\frac{\dot{M}_{ref}}{L_{ref}}\right)^2\right]^{1/3} d\dot{x} \Leftrightarrow \\
\Leftrightarrow \frac{3}{4}\dot{M}_{ref}^{4/3} &= \left[\frac{(\rho_l-\rho_v)\,bg}{12\upsilon_v}\left(\frac{\lambda_v b\Delta T}{h^*_{lv}}\right)^3+\frac{\rho_v b u_L}{2}\frac{\lambda_v b\Delta T}{h^*_{lv}}\left(\frac{\dot{M}_{ref}}{L_{ref}}\right)^2\right]^{1/3}\cdot L_{ref} \Leftrightarrow \\
\Leftrightarrow \dot{M}_{ref} &= \left(\frac{4}{3}\right)^{3/4}\left[\frac{(\rho_l-\rho_v)\,bg}{12\upsilon_v}\left(\frac{\lambda_v b\Delta T}{h^*_{lv}}\right)^3+\frac{\rho_v b u_L}{2}\frac{\lambda_v b\Delta T}{h^*_{lv}}\left(\frac{\dot{M}_{ref}}{L_{ref}}\right)^2\right]^{1/4}\cdot L_{ref}^{3/4} \Leftrightarrow \\
\Leftrightarrow \frac{h\Delta T b L_{ref}}{h^*_{lv}} &= \left(\frac{4}{3}\right)^{3/4}\left[\frac{(\rho_l-\rho_v)\,bg}{12\upsilon_v}\left(\frac{\lambda_v b\Delta T}{h^*_{lv}}\right)^3+\frac{\rho_v b u_L}{2}\frac{\lambda_v b\Delta T}{h^*_{lv}}\frac{h^2\Delta T^2 b^2}{(h^*_{lv})^2}\right]^{1/4}\cdot L_{ref}^{3/4} \Leftrightarrow \\
\Leftrightarrow h &= \left(\frac{4}{3}\right)^{3/4}\left(\frac{1}{2}\right)^{1/4}\left[\frac{\lambda_v^3\rho_v(\rho_l-\rho_v)gh^*_{lv}}{6L_{ref}\Delta T\mu_v}+\frac{h^2u_L\lambda_v\rho_v h^*_{lv}}{L_{ref}\Delta T}\right]^{1/4} \Leftrightarrow \\
h^4 &= \frac{16}{81}\frac{\lambda_v^3\rho_v(\rho_l-\rho_v)gh^*_{lv}}{L_{ref}\Delta T\mu v}+\frac{32}{27}\frac{h^2u_L\lambda_v\rho_v h^*_{lv}}{L_{ref}\Delta T}
\end{aligned}$$

Using the quadratic formula, we can develop this equation further and find the following expression:

$$\boxed{h=\frac{4}{3\sqrt{3}}\sqrt{\frac{u_L\lambda_v\rho_v h^*_{lv}}{L_{ref}\Delta T}}\cdot\left[1+\sqrt{1+\frac{9}{16}\frac{\lambda_v(\rho_l-\rho_v)gL_{ref}\Delta T}{u_L^2\rho_v\mu_v h^*_{lv}}}\right]^{1/2}} \tag{A.11}$$

A.2 Prediction of the wall's temperature with time for the HFE7100 experiments

Microgravity conditions

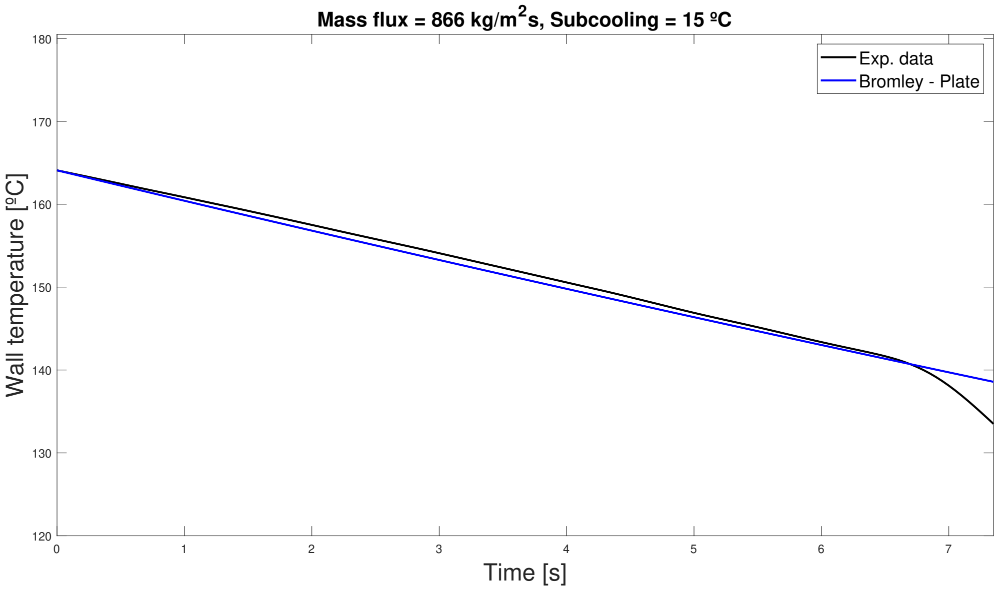

Figure A.1:

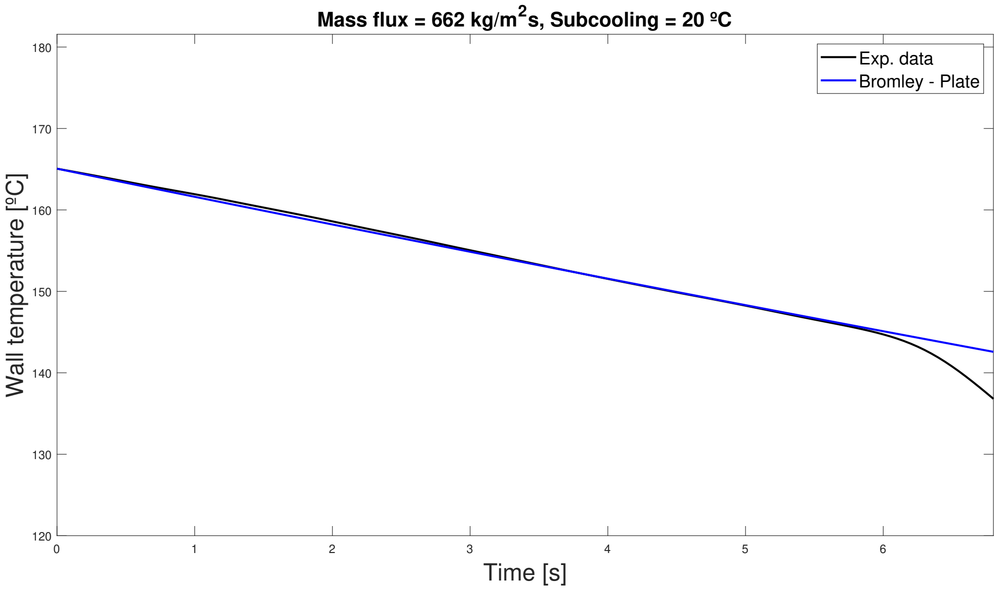

Figure A.2:

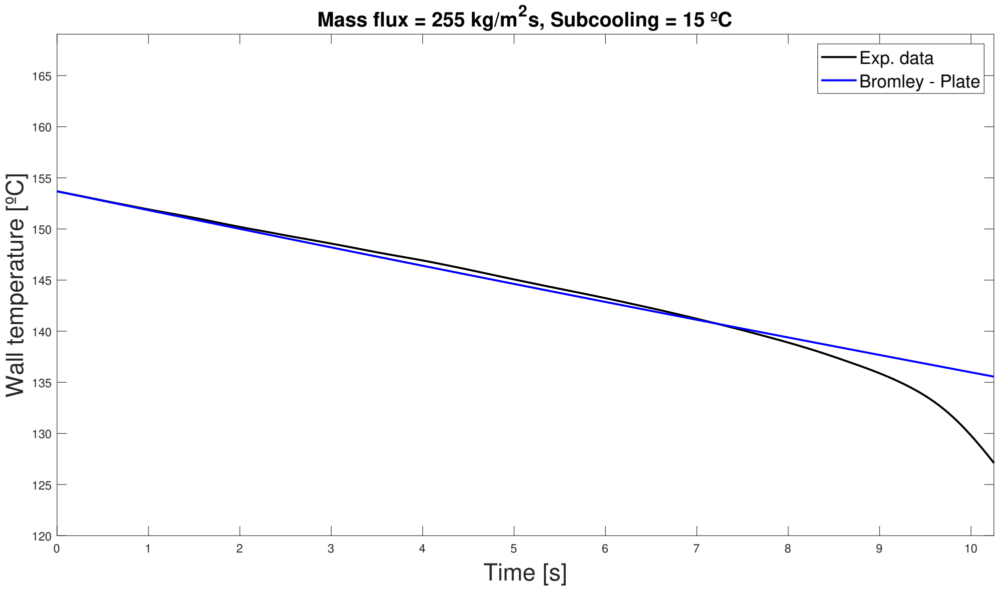

Figure A.3:

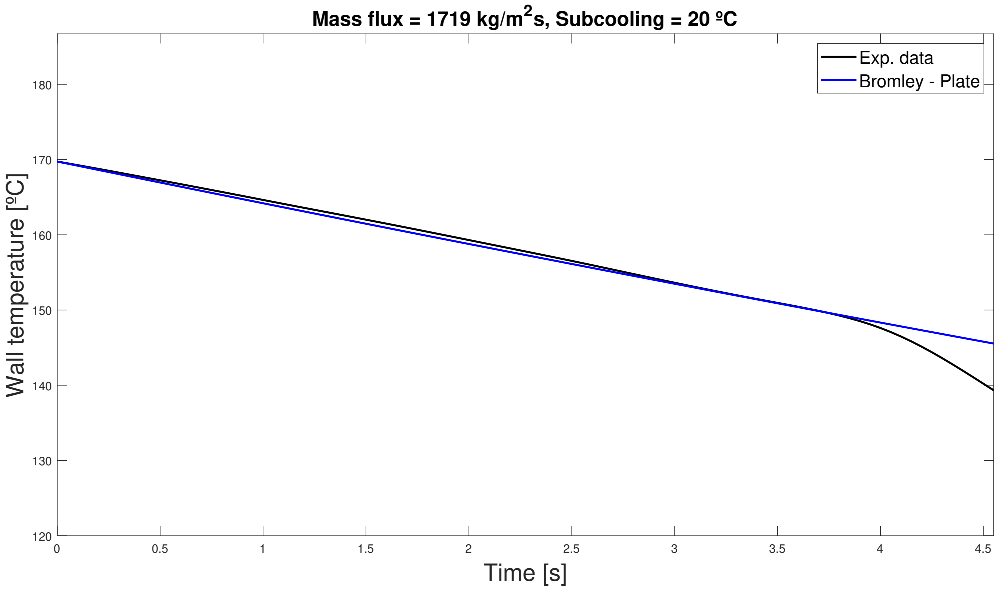

Figure A.4:

Normal gravity conditions

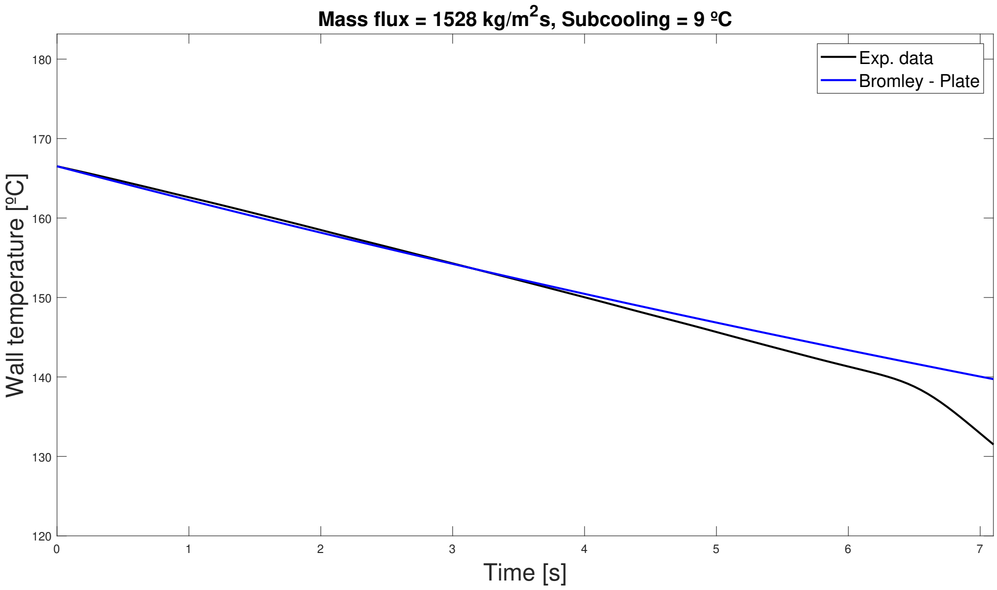

Figure A.5:

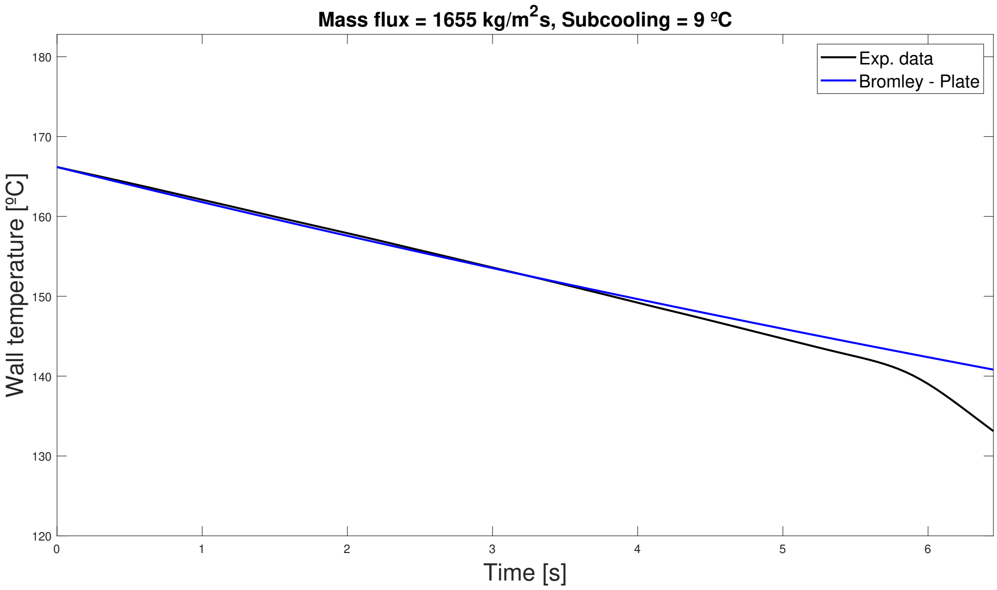

Figure A.6:

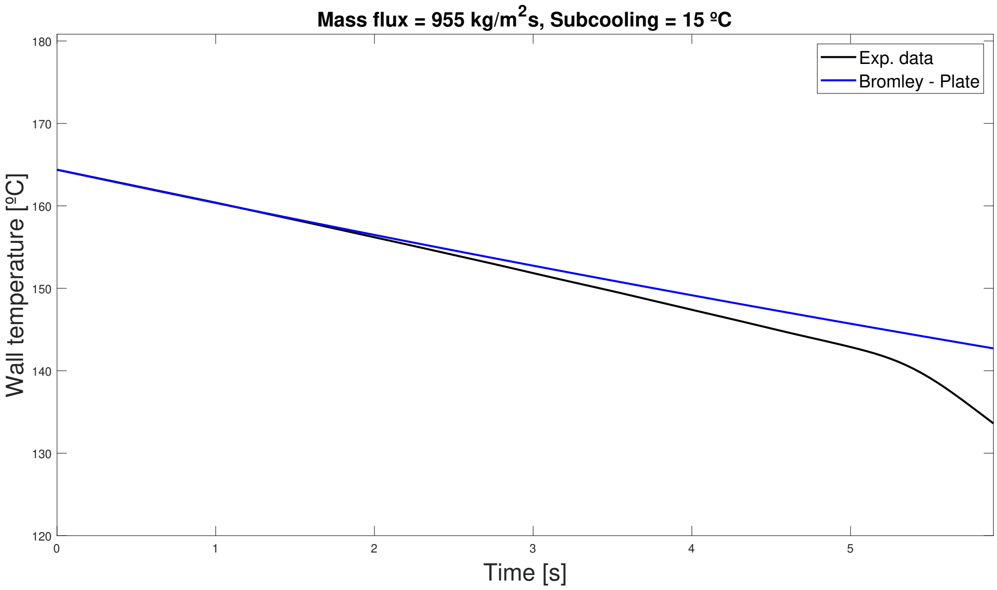

Figure A.7:

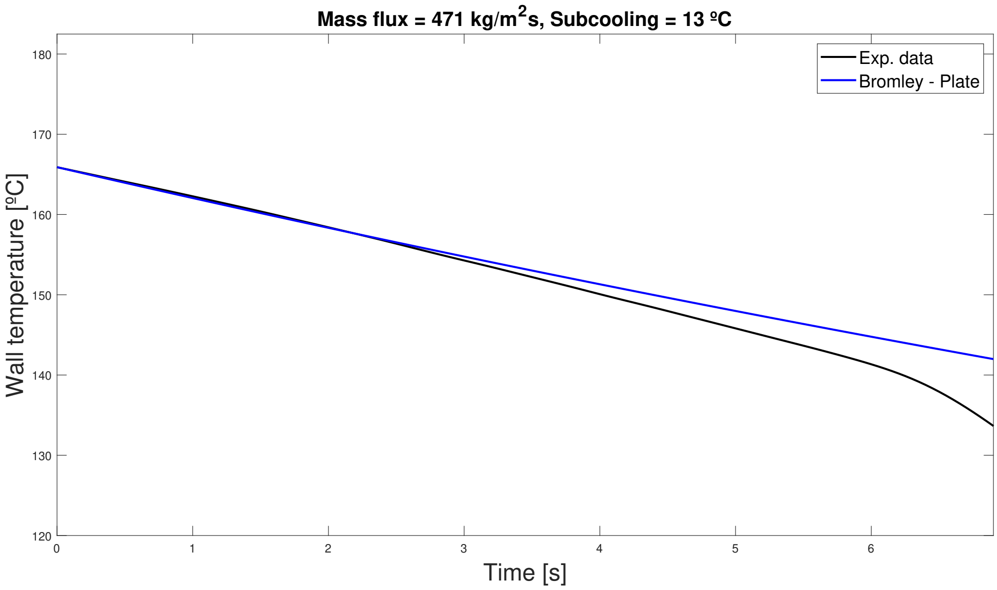

Figure A.8:

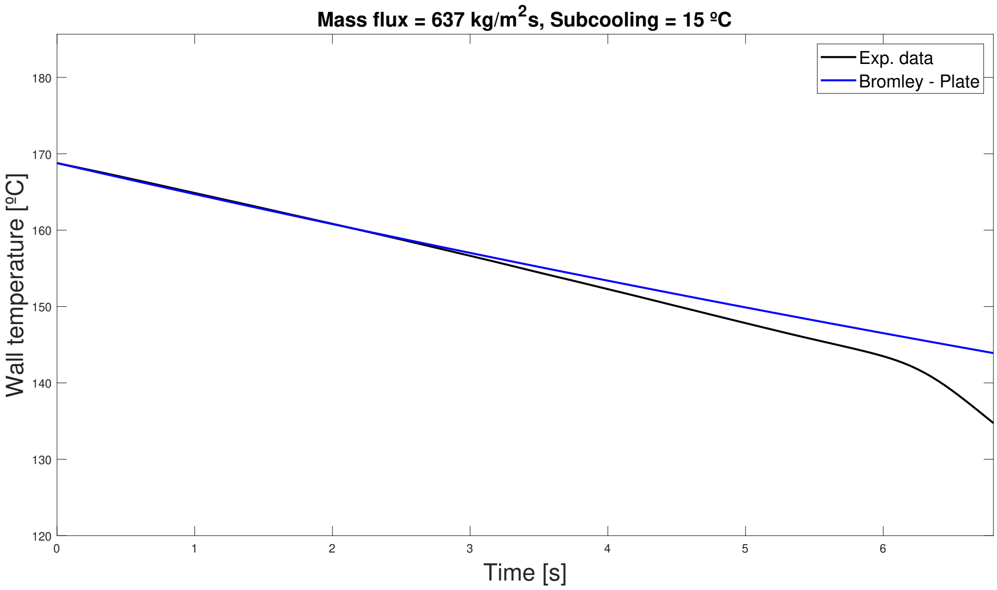

Figure A.9:

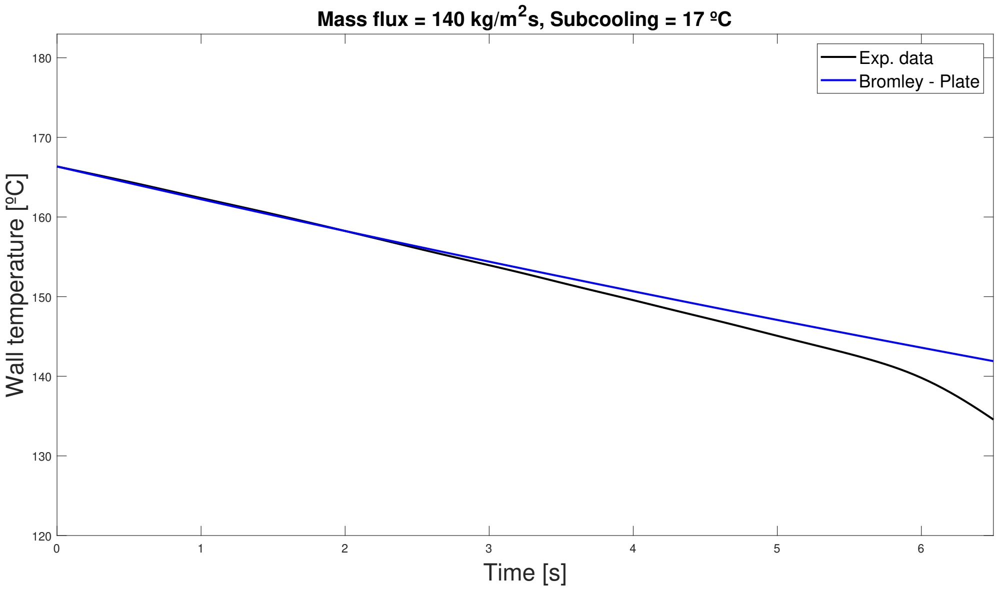

Figure A.10:

A.3 Prediction of the wall's temperature with time for the cryogenic experiments

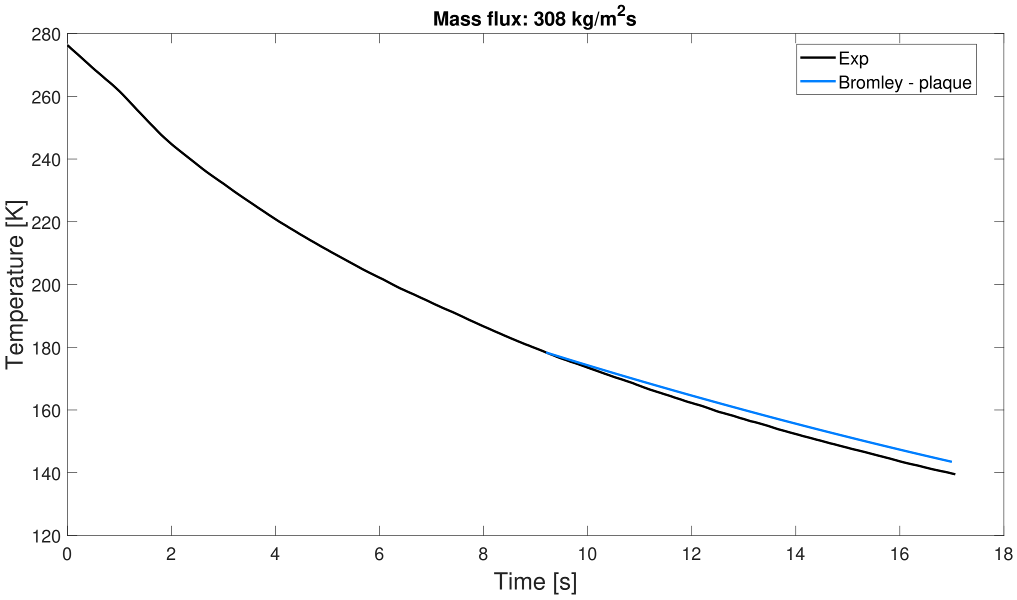

Figure A.11:

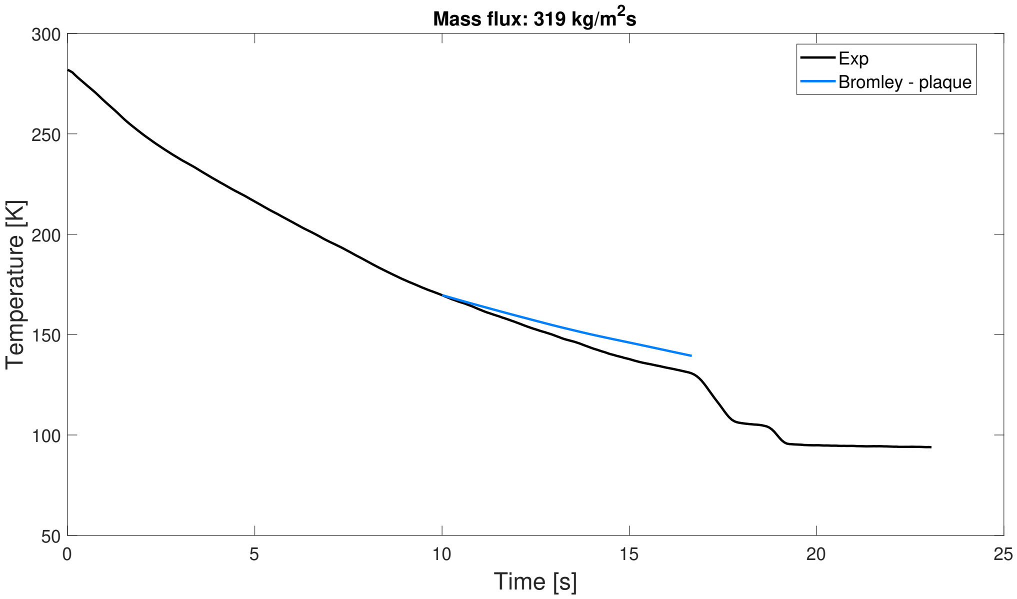

Figure A.12:

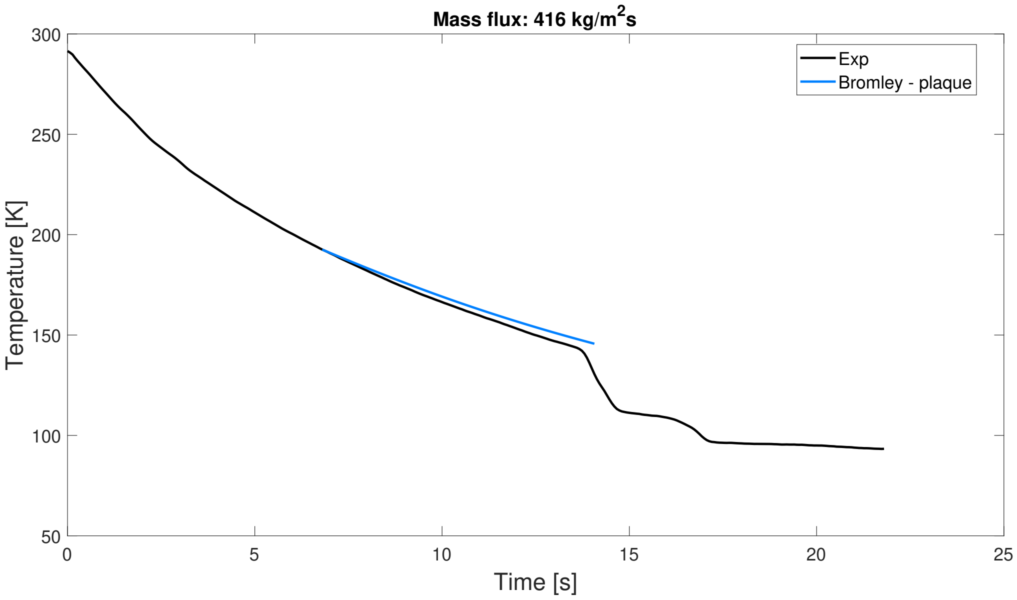
Mass flux: 416 kg/m²s
Exp
Bromley - plaque
Temperature [K]
300
250
200
150
100
50
Time [s]
0
5
10
15
20
25

Figure A.13:

A.4 Prediction of the nucleate boiling part of the boiling curve using Liu & Winterton correlation

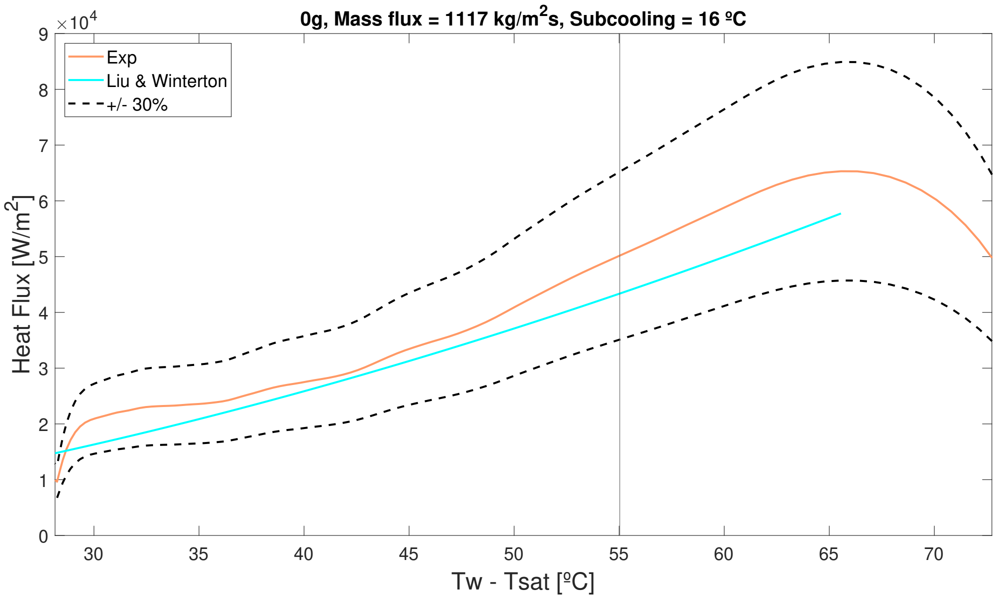

Figure A.14:

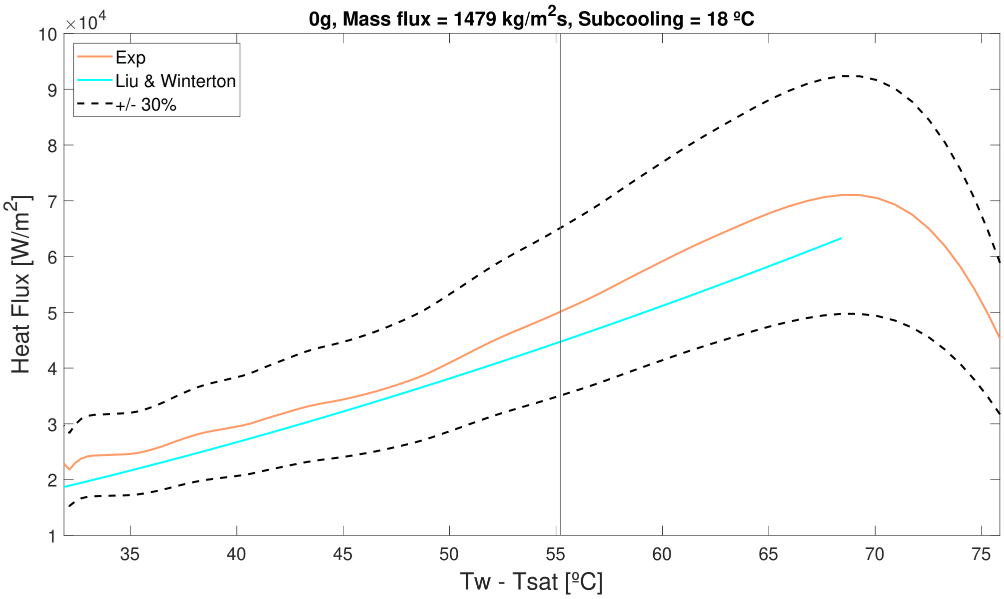

Figure A.15:

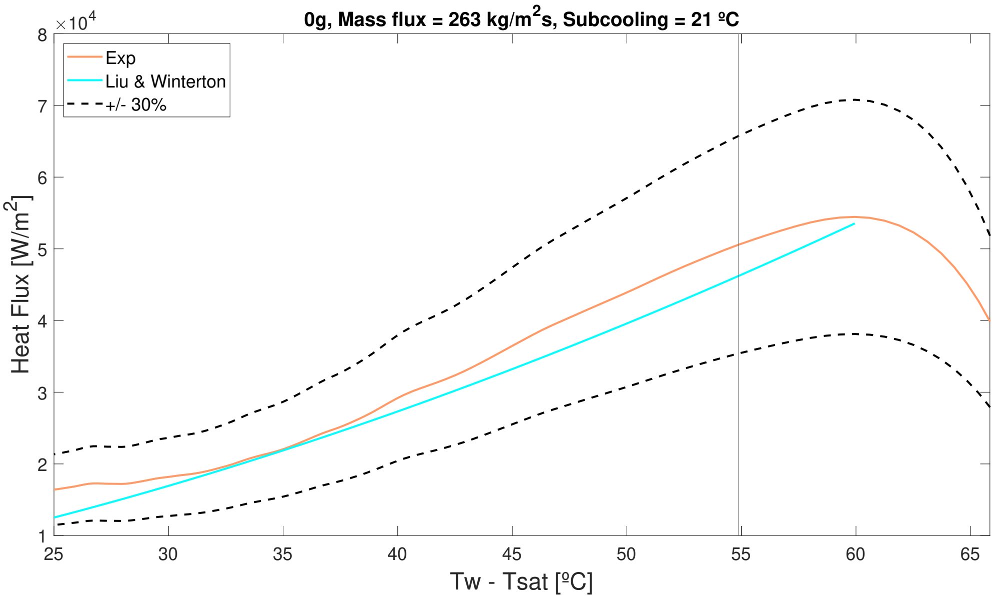

Figure A.16:

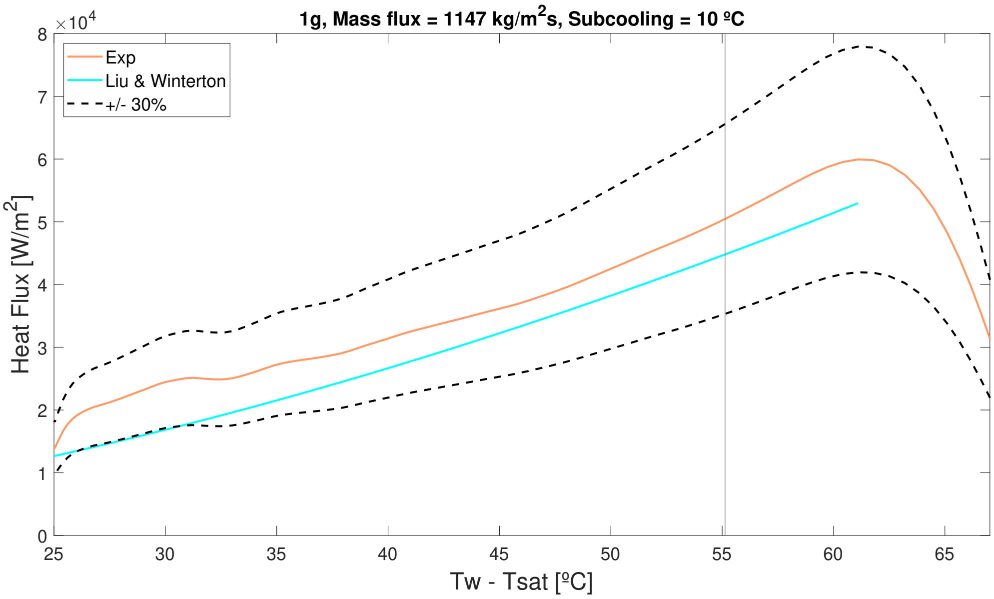

Figure A.17:

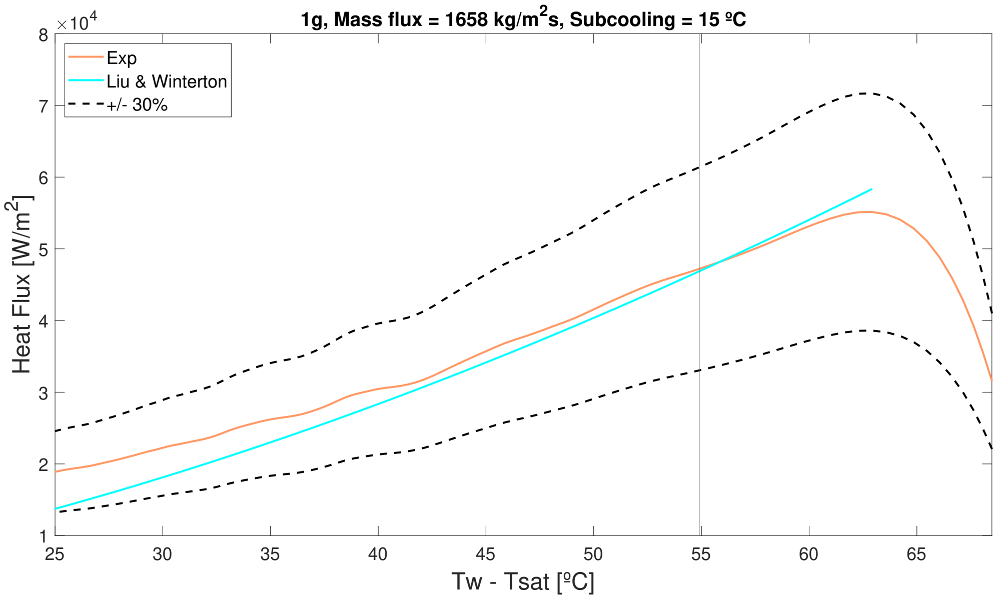

Figure A.18:

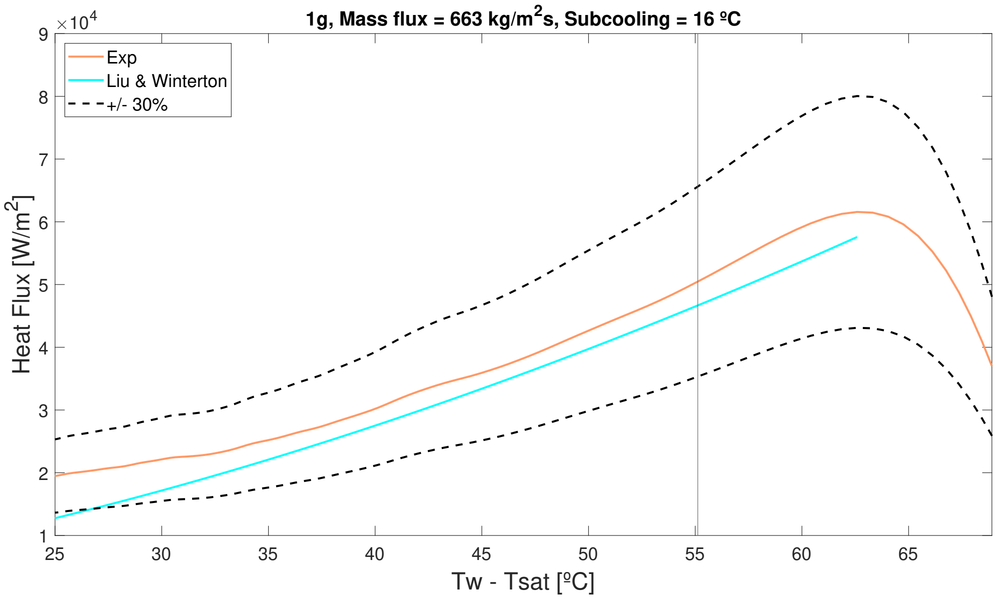

Figure A.19:

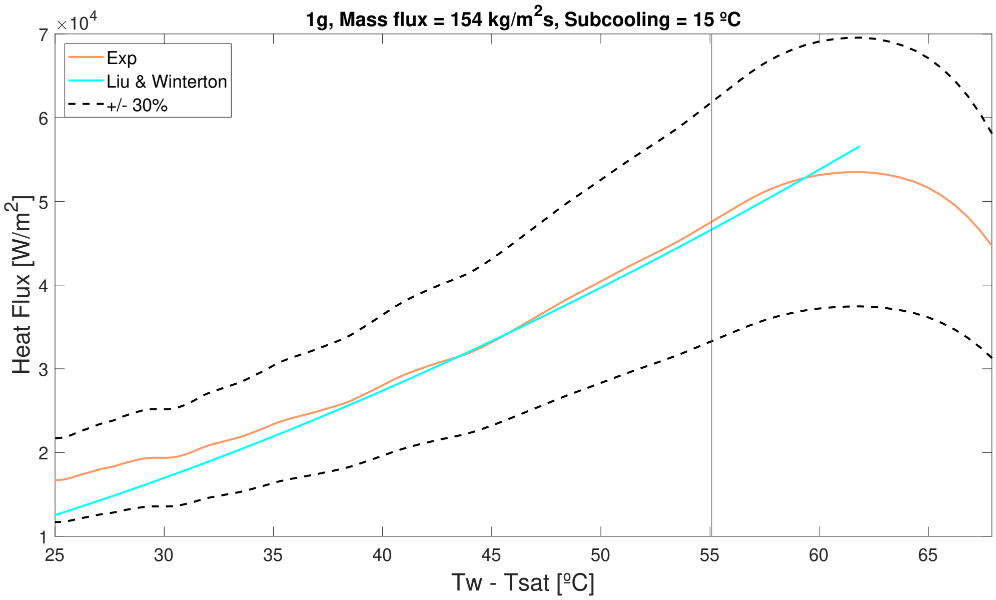
1g, Mass flux = 154 kg/m2s, Subcooling = 15 ºC
×10^4
7
6
5
4
3
2
1
Heat Flux [W/m2]
25
30
35
40
45
50
55
60
65
Tw - Tsat [ºC]
Exp
Liu & Winterton
+/- 30%

Figure A.20:

A.5 Data from Auracher and Marquardt[5]

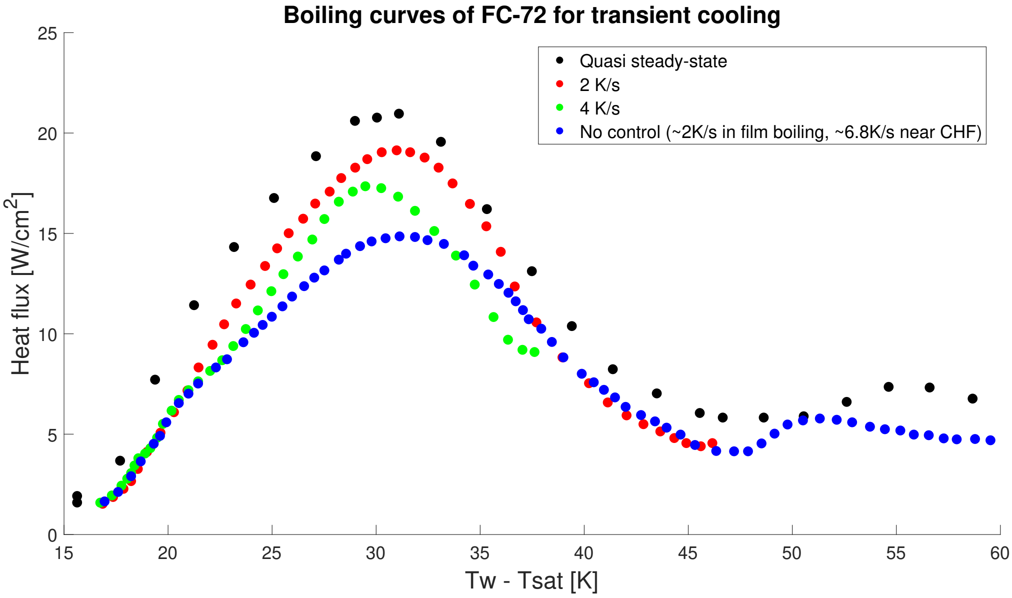

Figure A.21: